



12-1-2007

Remote Sensing of Heat Fluxes Validation and Inter-Sensor Comparison

Tedros M. Berhane

Follow this and additional works at: <https://commons.und.edu/theses>

Recommended Citation

Berhane, Tedros M., "Remote Sensing of Heat Fluxes Validation and Inter-Sensor Comparison" (2007).
Theses and Dissertations. 2965.
<https://commons.und.edu/theses/2965>

This Thesis is brought to you for free and open access by the Theses, Dissertations, and Senior Projects at UND Scholarly Commons. It has been accepted for inclusion in Theses and Dissertations by an authorized administrator of UND Scholarly Commons. For more information, please contact und.common@library.und.edu.

REMOTE SENSING OF HEAT FLUXES
VALIDATION AND INTER-SENSOR COMPARISON

by

Tedros M. Berhane
Bachelor of Science, University of Asmara, 2001

A Thesis

Submitted to the Graduate Faculty

of the

University of North Dakota

in partial fulfillment of the requirements

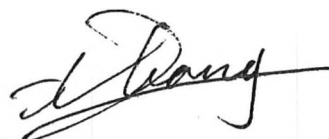
for the degree of

Master of Science

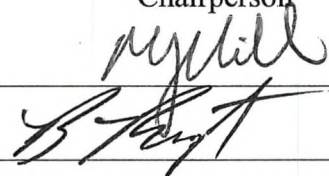
Grand Forks, North Dakota
December
2007

Copyright 2007 Tedros M. Berhane

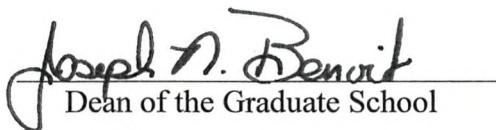
This thesis, submitted by Tedros M. Berhane in partial fulfillment of the requirements for the Degree of Master of Science from the University of North Dakota, has been read by the Faculty Advisory Committee under whom the work has been done and is hereby approved.



Chairperson



This thesis meets the standards for appearance, conforms to the style and format requirements of the Graduate School of the University of North Dakota, and is hereby approved.



Dean of the Graduate School



Date

PERMISSION

Title Remote Sensing of Heat Fluxes: Validation and Inter-sensor
Comparison

Department Earth System Science and Policy

Degree Master of Science

In presenting this thesis in partial fulfillment of the requirements for a graduate degree from the University of North Dakota, I agree that the library of this University shall make it freely available for inspection. I further agree that permission for extensive copying for scholarly purposes may be granted by the professor who supervised my thesis work or, in his absence, by the chairperson of the department or the dean of the Graduate School. It is understood that any copying or publication or other use of this thesis or part thereof for financial gain shall not be allowed without my written permission. It is also understood that due recognition shall be given to me and to the University of North Dakota in any scholarly use which may be made of any material in my thesis.

Signature

A handwritten signature in dark ink, appearing to be 'J. B. J.', written over a horizontal line.

Date

Nov 30, 2007

TABLE OF CONTENTS

LIST OF FIGURES.....	viii
LIST OF TABLES.....	xii
ACKNOWLEDGEMENTS.....	xiii
ABSTRACT.....	xv
CHAPTER	
I INTRODUCTION.....	1
Objectives.....	3
Descriptions of the Study Area.....	4
Brookings, SD.....	4
Fort Peck, MT.....	5
Instrumentation.....	6
II REMOTE SENSING OF EVAPOTRANSPIRATION AND THE SEBAL MODEL.....	8
Evapotranspiration.....	8
Remote Sensing of Evapotranspiration.....	12
Theoretical Basis.....	13
Net Radiation.....	15
Soil Heat Flux.....	16
Sensible Heat Flux.....	17
Latent Heat Flux.....	20

	The SEBAL Model.	21
	SEBAL Case Studies.	21
	Data and SEBAL Methods.	26
	Net Radiation.	26
	Soil Heat Flux.	32
	Sensible Heat Flux.	32
	Latent Heat Flux.	43
III	FLUX TOWERS AND STATISTICAL ANALYSIS.	44
	Measurement of Flux Tower.	44
	Footprint Analysis.	45
	Results of Footprint Analysis.	48
	Statistical Analysis.	48
IV	RESULTS AND DISCUSSION.	50
	Landsat.	51
	Net Radiation.	51
	Soil Heat Flux.	54
	Sensible Heat Flux.	55
	Latent Heat Flux.	56
	MODIS.	58
	Net Radiation.	58
	Soil Heat Flux.	60
	Sensible Heat Flux.	62
	Latent Heat Flux.	63

	Inter-sensor Comparison.	64
	Surface Energy Balance Closure.	72
	Sensitivity Analysis	73
V	CONCLUSIONS AND FUTURE WORK	77
	Conclusions	77
	Future Work.	79
	APPENDICES.	81
	REFERENCES.	110

LIST OF FIGURES

Figure	Page
1. Effect of spatial resolution on signals received from land surface elements by Landsat 3, 2, 1 bands (left) and MODIS 1, 4, 3 bands (right) around Fort Peck, MT, flux tower. The images were acquired on the date 070203 and cover 900 km ² (From: USGS 2006)	3
2. Location of the flux towers.	4
3. Spatial heterogeneity of land cover classes in an area of 1 km ² around Brookings, SD (left) and Fort Peck, MT (right) flux towers (From: USGS 2001 National Land Cover map)	5
4. Landscape near the Brookings (left) and Fort Peck (right) flux towers (From: AmeriFlux 2007).	6
5. Conceptual diagram of momentum transfer by turbulent diffusion (From: Dingman 2002).	14
6. Vertical distribution of wind speed. In the Figure, Z_0 , Z_d and Z_{veg} refer to the roughness height, zero plane of displacement and vegetation height, respectively (From: Dingman 2002)	19
7. Relationship between δT and T_0 for cold and hot pixels.	38
8. Unstable, neutral (adiabatic), and stable lapse rates near the surface (From: Dingman 2002).	39
9. Orientation and strength of flux contributing area to an arbitrarily located flux tower in relation to wind direction: The darker the color, the higher the contribution.	45
10. Comparison of R_n between the estimates by SEBAL using Landsat data and the measurements by two flux towers in Brookings and Fort Peck sites. . . .	52
11. Comparison of G_0 between the estimates by SEBAL using Landsat data and the measurements by two flux towers in Brookings and Fort Peck sites. . . .	54

12.	Comparison of H between the estimates by SEBAL using Landsat data and the measurements by two flux towers in Brookings and Fort Peck sites. . .	55
13.	Comparison of λE between the estimates by SEBAL using Landsat data and the measurements by two flux towers in Brookings and Fort Peck sites. . .	57
14.	Comparison of R_n between the estimates by SEBAL using MODIS data and the measurements by two flux towers in Brookings and Fort Peck	59
15.	Comparison of G_0 between the estimates by SEBAL using MODIS data and the measurements by two flux towers in Brookings and Fort Peck sites. . .	61
16.	Comparison of H between the estimates by SEBAL using MODIS data and the measurements by two flux towers in Brookings and Fort Peck sites . . .	62
17.	Comparison of λE between the estimates by SEBAL using MODIS data and the measurements by two flux towers in Brookings and Fort Peck sites . . .	64
18.	Comparison of R_n between the estimates by SEBAL using Landsat pixels simulated to a MODIS pixel and the measurements by two flux towers in Brookings and Fort Peck sites.. . . .	66
19.	Comparison of G_0 between the estimates by SEBAL using Landsat pixels simulated to a MODIS pixel and the measurements by two flux towers in Brookings and Fort Peck sites.	66
20.	Comparison of H between the estimates by SEBAL using Landsat pixels simulated to a MODIS pixel and the measurements by two flux towers in Brookings and Fort Peck sites.	67
21.	Comparison of λE between the estimates by SEBAL using Landsat pixels simulated to a MODIS pixel and the measurements by two flux towers in Brookings and Fort Peck sites.	68
22.	Comparison of R_n between the estimates by SEBAL using Landsat pixels simulated to a MODIS pixel and a MODIS pixel for Brookings and Fort Peck sites.	70
23.	Comparison of G_0 between the estimates by SEBAL using Landsat pixels simulated to a MODIS pixel and a MODIS pixel for Brookings and Fort Peck sites.	70
24.	Comparison of H between the estimates by SEBAL using Landsat pixels simulated to a MODIS pixel and a MODIS pixel for Brookings and Fort Peck sites.	71

25.	Comparison of λE between the estimates by SEBAL using Landsat pixels simulated to a MODIS pixel and a MODIS pixel for Brookings and Fort Peck sites.	71
26.	a) footprint and b) cumulative flux as a function of fetch for Landsat TM 080404 overpass date.	91
27.	a) footprint and b) cumulative flux as a function of fetch for Landsat TM 051905 overpass date.	92
28.	a) footprint and b) cumulative flux as a function of fetch for Landsat TM 080705 overpass date.	93
29.	a) footprint and b) cumulative flux as a function of fetch for Landsat TM 062306 overpass date.	94
30.	a) footprint and b) cumulative flux as a function of fetch for Landsat TM 050907 overpass date.	95
31.	a) footprint and b) cumulative flux as a function of fetch for MODIS 051905 overpass date.	96
32.	a) footprint and b) cumulative flux as a function of fetch for MODIS 080705 overpass date.	97
33.	a) footprint and b) cumulative flux as a function of fetch for MODIS 072306 overpass date.	98
34.	a) footprint and b) cumulative flux as a function of fetch for Landsat ETM+ 081702 overpass date.	99
35.	a) footprint and b) cumulative flux as a function of fetch for Landsat ETM+ 090202 overpass date.	100
36.	a) footprint and b) cumulative flux as a function of fetch for Landsat TM 081203 overpass date.	101
37.	a) footprint and b) cumulative flux as a function of fetch for Landsat TM 080406 overpass date.	102
38.	a) footprint and b) cumulative flux as a function of fetch for Landsat TM 081106 overpass date.	103
39.	a) footprint and b) cumulative flux as a function of fetch for MODIS 081702 overpass date.	104

40.	a) footprint and b) cumulative flux as a function of fetch for MODIS 090202 overpass date.	105
41.	a) footprint and b) cumulative flux as a function of fetch for MODIS 071803 overpass date.	106
42.	a) footprint and b) cumulative flux as a function of fetch for MODIS 081203 overpass date.	107
43.	a) footprint and b) cumulative flux as a function of fetch for MODIS 080406 overpass date.	108
44.	a) footprint and b) cumulative flux as a function of fetch for MODIS 081106 overpass date.	109

LIST OF TABLES

Table	Page
1. Measurements and instrumentation at Brookings, SD, and Fort Peck, MT, flux tower sites (AmeriFlux 2007)	7
2. Model performance statistics for Landsat: Both towers and all dates.	51
3. Model performance statistics of radiation components for Landsat: Both towers and all dates	52
4. Model performance statistics for MODIS: Both towers and all dates	58
5. Model performance statistics of radiation components for MODIS: Both towers and all dates	60
6. Model performance statistics for Landsat pixels simulated to a MODIS pixel: Both towers and all dates	68
7. Absence of energy closure observed at flux towers for all the dates and for both sensors	73
8. Results of sensitivity analysis of SEBAL sensible heat flux modeling to input parameters	75
9. Attributes of Landsat TM for Brookings, SD, flux tower site (USGS 2006)	85
10. Attributes of Landsat TM and ETM+ for Fort Peck, MT, flux tower site (USGS 2006)	85
11. Descriptions of Landsat 5 TM (USGS 2006)	86
12. Descriptions of Landsat 7 ETM+ (USGS 2006)	86
13. Descriptions of MOD011A1 products (USGS 2006)	87
14. Descriptions of MOD09GHK products (USGS 2006)	87
15. SEBAL parameters for the cold and hot reference pixels selected	88

ACKNOWLEDGEMENTS

Thank you Lord for all the things you blessed me with, if it had not been for you on my side things would have been different. Lord, I am always grateful for your love and mercy.

I would like to thank UMAC for giving me the chance to gain a lifetime of experience and knowledge, and more than anything for the kind financial support extended to me throughout my stay in the program. I am extremely grateful for my advisor, Dr. Xiaodong Zhang, who has always been supportive and encouraging me throughout this project. Without his unreserved support, this reality would have been just a dream. Thank you! Equally, I am extremely thankful for my committee members, Dr. Michael Hill and Dr. Bradley Rundquist, who showed no hesitation in sparing their valuable time to advise, support and encourage me to do work that would have been impossible without such help. I would like to thank the ND View Scholarship program and the office of Research Development at the University of North Dakota for providing support to present this work at the 2007 American Geophysical Union (AGU) Conference. I would like also to thank Dr. Alexander Smart and Dr. Tagir Gilmanov, from South Dakota State University for their extensive help in providing me all the required data and information about the flux tower located at Brookings, SD, site. Last but not least, I want to thank the Montana State Digital Library in proving me the different GIS layers including the 2005 high resolution aerial photographs.

Thanks to all my professors and my classmates who have been always supporting and nice to me. I am extremely grateful for all the people with whom I have spent these last two years, people with whom I have worked and people with whom I have spent even fractions of seconds. Your hospitality and unreserved help made me feel at home even when I went through excitement and challenges of life in a new culture, meeting new people, and living in a place as cold as North Dakota. Thank you all! I am particularly grateful for Dr. Wendy Loya for her hospitality during my initial arrival in the US. Tedros and Arsema and their families, thank you all for being good to me.

I want to thank my entire family, my mom and my father. Thanks dad and mom for being who you are. Dad, I missed you a lot. Your sudden departure I find still hard to believe. I am grateful for my friends, my brothers and sisters with their family.

I kindly would like to inform the readers of my work that I assume full responsibility on any mistake that would come to your attention.

ABSTRACT

Instantaneous heat fluxes were modeled using data obtained from Landsat 5 TM (Thematic Mapper), Landsat 7 ETM+ (Enhanced Thematic Mapper Plus) and Terra MODIS (Moderate Resolution Imaging Spectroradiometer) using the Surface Energy Balance Algorithm for Land (SEBAL) model for cloud-free days. The modeled results were compared with measurements of net radiation (both incoming and outgoing, shortwave and longwave), soil sensible and latent heat fluxes from two flux towers located in Brookings, SD, and Fort Peck, MT. Flux tower data consisted of 30 minute averages at every half an hour, and footprints of contributing movement of air within the period were estimated for each satellite overpass by taking into account the factors of observation height, atmospheric stability, and surface roughness, as well as wind speed and directions (Hsieh *et al.* 2000). It was found that footprints (considering 90% contributing areas) were normally larger than the size of one Landsat pixel (30 m) but smaller than that of one MODIS pixel (1 km). Therefore, for Landsat the data were averaged for pixels within the concurrent footprint, and for MODIS the data for the particular pixel covering the flux tower was used.

The R^2 values between the modeled and the observed net radiation (R_n) for Landsat and MODIS were found to be 0.70 and 0.66, respectively. Relatively, comparisons between modeled and observed values were better at Brookings than at Fort Peck for both sensors. This may be because the former site has a relatively flat topography and larger fetch than the latter, minimizing the possible effects of terrain

heterogeneity on incoming and outgoing radiation modeling. Both satellites performed poorly in modeling soil heat flux (G_0). Our results show that SEBAL provides a better modeling of sensible heat flux (H) with Landsat ($R^2 = 0.62$) than with MODIS ($R^2 = 0.11$), even though the MODIS performance for estimating latent heat flux (λE) improved ($R^2 = 0.37$). The improvement found in estimating latent heat flux is probably due to the fact that in SEBAL cold pixels are used to estimate air temperature and then also used in computation for both R_n and H . The uncertainties associated with this assumption cancelled out in deriving λE .

Overall, SEBAL performed better in modeling the heat fluxes when Landsat data were used. This may be due to the scaling issue, as the footprint areas were always significantly less than a single MODIS pixel. By simulating MODIS observations using Landsat, it was found that the R^2 value for the aggregated Landsat pixels decreased from 0.62 to 0.25 with an increase of root mean square difference (RMSD) from 50.5 to 68.3 Wm^{-2} . This suggested that the poor performance of MODIS in estimating heat fluxes was due to heterogeneity of the surface within a field of view. In addition, sensitivity analyses of the model to input parameters suggested that the model is more sensitive to surface-to-air temperature difference than to surface roughness conditions. Appendix A lists symbols mentioned in this thesis.

CHAPTER I

INTRODUCTION

The hydrological cycle is a major driver in redistributing solar energy across the earth's surface, and accurate estimates of evapotranspiration (ET) are critical in understanding and monitoring the dynamics of water and energy cycles. Direct measurement of ET under field conditions is labor-intensive and requires highly skilled operational staff and/or substantial financial resources (Pereira *et al.* 2006).

Advances in modeling and remote sensing technology during the last couple of decades have allowed the quantification of heat and vapor fluxes across the atmospheric boundary layer at various spatial and temporal scales (Oliosio *et al.* 1999; Overgaard *et al.* 2006; Waheed *et al.* 2006). The Surface Energy Balance Algorithm for Land (SEBAL) was developed by Bastiaanssen (1995) using Landsat 5 Thematic Mapper (TM) to estimate ET over vegetated surfaces. Since then, the model has been extensively tested with data from various satellite sensors. The advantage of SEBAL is that all the required parameters except wind speed can be modeled using multi-spectral observations provided by Advanced Spaceborne Thermal Emission and Reflection Radiometer (ASTER), Landsat 7 Enhanced Thematic Mapper Plus (ETM+) or TM, Geostationary Environmental Satellite (GOES), National Oceanic and Atmospheric Administration-the Advanced Very High Resolution Radiometer (NOAA-AVHRR) or Moderate Resolution Imaging Spectroradiometer (MODIS; Hafeez *et al.* 2002). However, in addition to cloud cover, characteristics and operations of the sensors pose limits on their applications in

SEBAL. For example, the higher spatial resolution of Landsat thermal infrared (IR) sensors (60 m for ETM+ and 120 m for TM) is compromised by poor temporal resolution of 16 days, which limits application in agricultural and water resource management often requiring daily ET updates (Kustas *et al.* 2003; Yang *et al.* 2005). On the other hand, MODIS sensors on board Terra and Aqua provide daily global coverage with 36 spectral bands (as compared to 8 of ETM+ and 7 of TM). This higher temporal resolution of MODIS increases the likelihood of obtaining cloud-free data. Also, MODIS data are free, while Landsat data cost about \$500 per scene. The one km spatial resolution, for the thermal bands of MODIS, however, makes accurate modeling of heat and vapor fluxes in a heterogeneous environment more challenging (Bastiaanssen *et al.* 1996; Cleugh *et al.* 2007). Fig. 1 illustrates the effect of the spatial resolution difference between Landsat and MODIS.

Both sensors have been used in SEBAL modeling, with MODIS offering potentially better estimates in surface reflectance, emissivity and temperature thanks to its higher spectral resolution. Nevertheless, very few studies have made direct comparisons between the two sensors (McCabe and Wood 2006). Moreover, there have been no reports on using the relevant MODIS data products to drive the SEBAL model directly. These products are daily land surface temperature and emissivity Level 3 global one km (MOD11A1), and daily surface reflectance Level 2G Global 500 m SIN Grid (MOD09GHK). In addition, no study has been conducted to compare modeled output of heat fluxes using Landsat and MODIS data over the same dates and geographical locations using the SEBAL model. Furthermore, it is worthwhile to evaluate the performance of the two sensors in different terrains. Appendices B and C list attributes of

Landsat TM and ETM+ datasets used in this study and radiometric, satellite and image characteristics descriptions of both Landsat and MODIS, respectively.

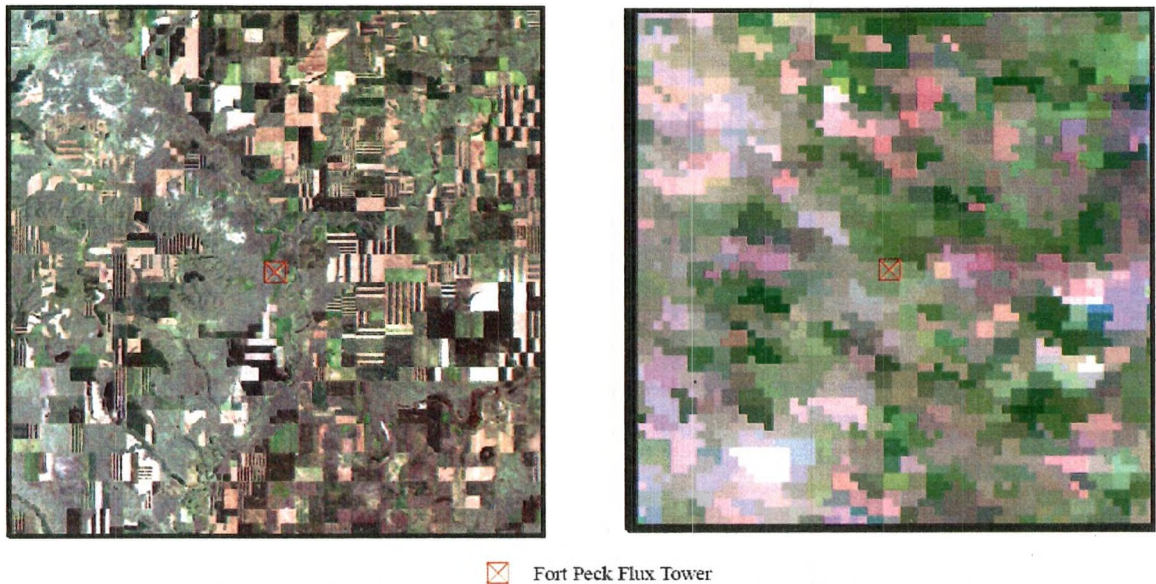


Figure 1. Effect of spatial resolution on signals received from land surface elements by Landsat 3, 2, 1 bands (left) and MODIS 1, 4, 3 bands (right) around Fort Peck, MT, flux tower. The images were acquired on the date 070203 and cover 900 km² (From: USGS 2006).

1.1 Objectives

The purpose of this study was to evaluate the performance of Landsat and MODIS data in modeling spatio-temporal distribution of instantaneous heat fluxes.

The following analyses were conducted:

1. Modeling instantaneous fluxes of net radiation, soil sensible and latent heat using SEBAL with remotely-sensed data from Landsat TM and ETM+, and Terra MODIS;
2. Comparing the modeled heat fluxes with each other and with measurements from the flux towers; and
3. Investigating scaling issues by comparing observations at different scales.

1.2 Descriptions of the Study Area

Two flux towers, one in Brookings, SD, and the other in Fort Peck, MT, were selected as the study sites (Fig. 2). The towers are part of the regional and continental flux tower network maintained by Fluxnet (AmeriFlux 2007). Fluxnet operates more than 400 towers across the globe providing long-term observation of carbon, heat and water fluxes across a diverse range of ecosystems and climates (Cleugh *et al.* 2007).

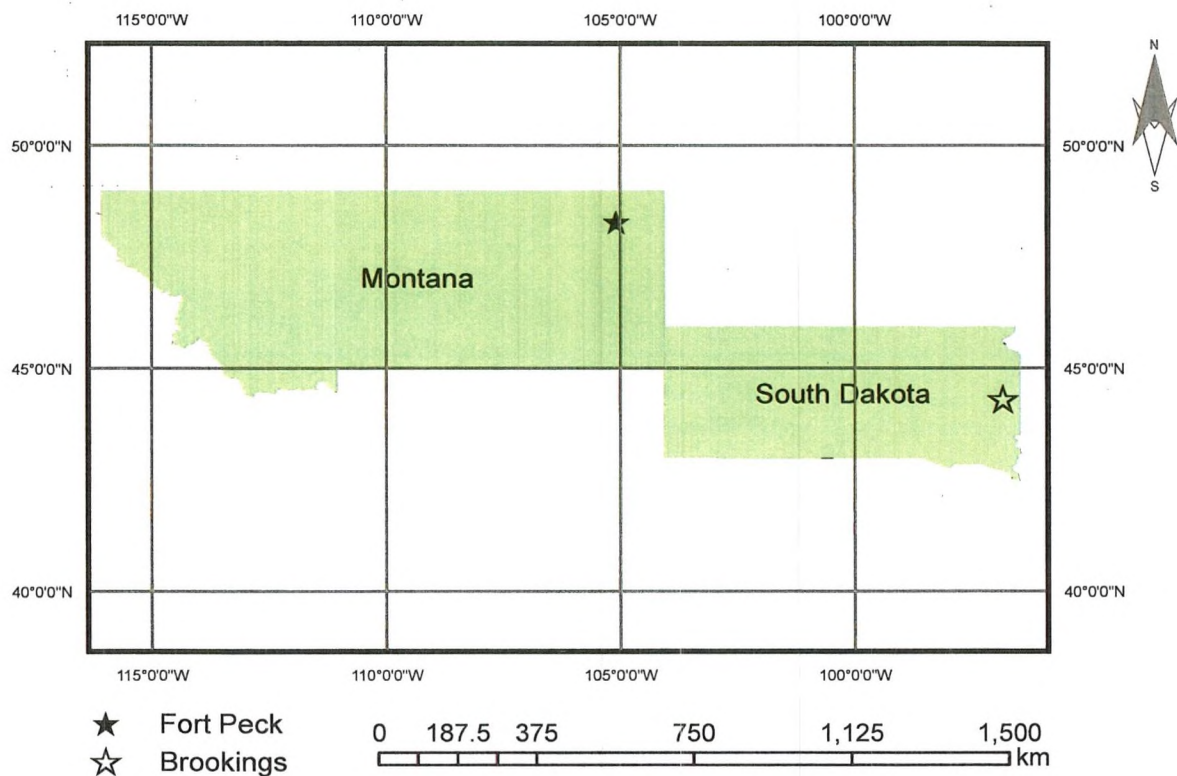


Figure 2. Location of the flux towers.

1.2.1 Brookings, SD

The Brookings flux tower is located north of the city of Brookings at $44^{\circ} 20' 43.044''$ N and $96^{\circ} 50' 10.212''$ W in a temperate climate (AmeriFlux 2007). Located on a family farm, the site is an actively grazed pasture with average canopy height of 30-40 cm (Figs. 3 and 4). The tower has been active since April 2004 (AmeriFlux 2007). The

height of the tower is 4 m on a flat terrain with an altitude of 510 m above sea level.

Between 2004 and 2005, the mean annual precipitation, the mean annual air temperature, the maximum and minimum air temperatures observed for the area were 600 mm, 6.92 °C, 35.2 °C and -33.3 °C, respectively (AmeriFlux 2007).

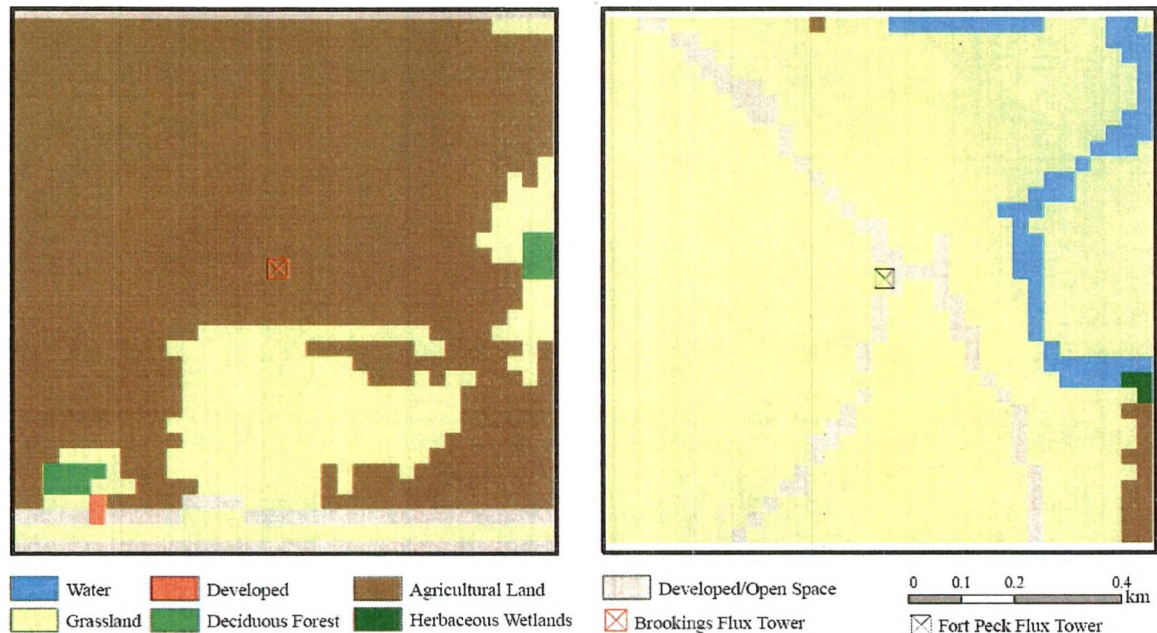


Figure 3. Spatial heterogeneity of land cover classes in an area of 1 km² around Brookings, SD (left) and Fort Peck, MT (right) flux towers (From: USGS 2001 National Land Cover map).

1.2.2 Fort Peck, MT

The Fort-Peck flux tower is located at 48° 18' 28.38" N and 105° 6' 1.92" W in the northeast part of Montana. The dominant vegetation in the area is grass, with an average height of 20-40 cm and fetch of 200 m. The tower has been in operation since November 1999 (AmeriFlux 2007). The height of the tower is 3.5 m over a relatively flat terrain with an altitude of 634 m above sea level (AmeriFlux 2007). Based on 2000-2005 data, mean annual precipitation, mean annual air temperature and maximum and minimum air temperature of the area reaches 500 mm, 5.13 °C, and 44.8 °C and -40.3 °C, respectively (AmeriFlux 2007).

1.2.3 Instrumentation

The towers in Brookings and Fort Peck are equipped with various instruments to measure eco-meteorological parameters (Table 1).

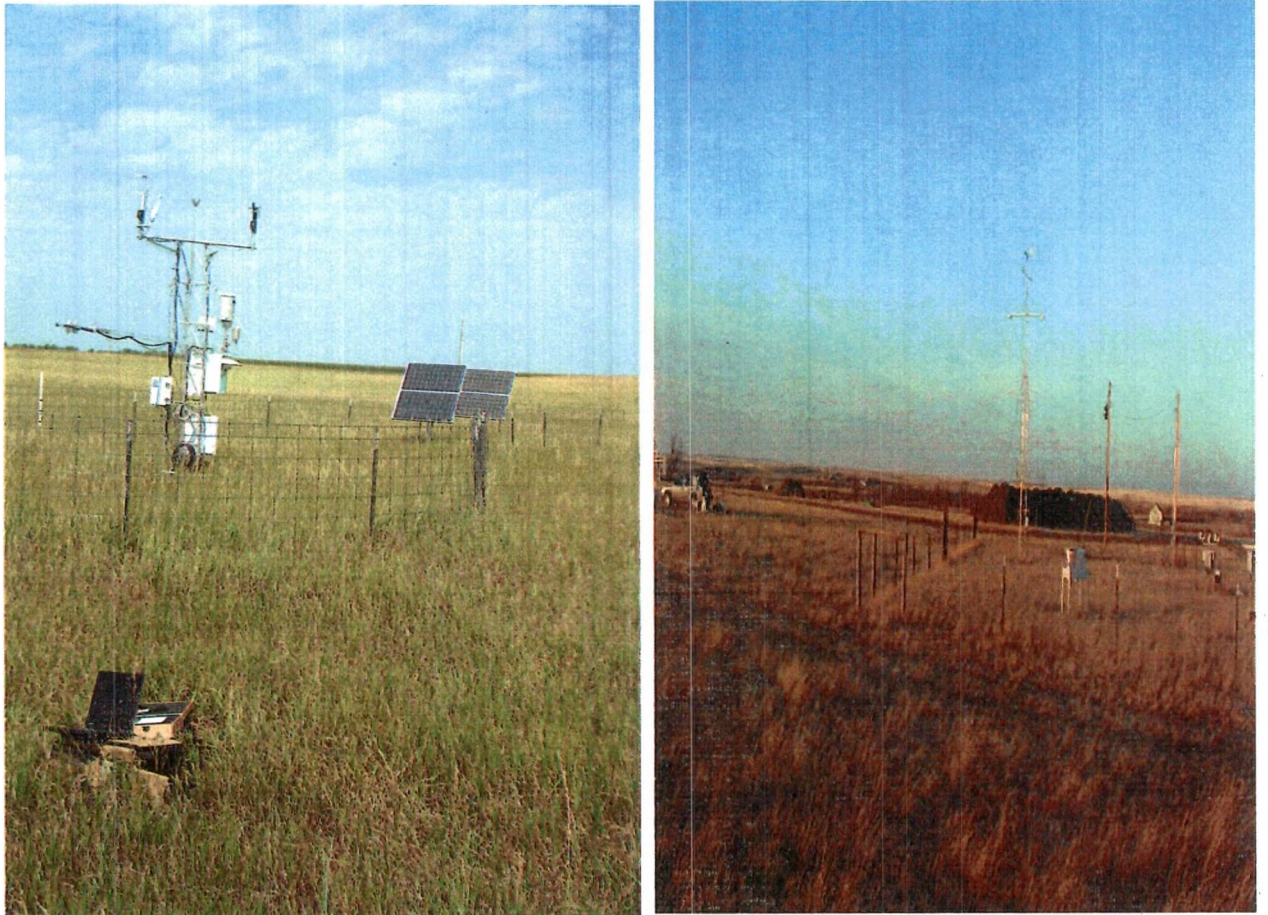


Figure 4. Landscape near the Brookings (left) and Fort Peck (right) flux towers (From: AmeriFlux 2007).

Table 1. Measurements and instrumentation at Brookings, SD, and Fort Peck, MT, flux tower sites (AmeriFlux 2007).

Parameter	Instrumentation		Model	
	Brookings, SD	Fort Peck, MT	Brookings, SD	Fort Peck, MT
Air temperature	Platinum resistance Thermometer	Temperature/relative humidity Transmitter and Platinum Resistance thermometer	Thermometrics PRT	Vaisala HMP50Y and Thermometrics PRT
Atmospheric pressure	Pressure transducer	Pressure transducer	Vaisala PTB101B	Vaisala PTB101B
Precipitation	Tipping bucket rain gauge	Tipping bucket rain gauge	Hydrological Services TB3	Hydrological Services TB3
Radiation, shortwave	Radiometer	Radiometer	Kipp & Zonen CNR 1	Kipp & Zonen CNR 1
Radiation, longwave	Radiometer	Radiometer	Kipp & Zonen CNR 1	Kipp & Zonen CNR 1
Radiation, net	Radiometer	Radiometer	Kipp & Zonen CNR 1	Kipp & Zonen CNR 1
Relative humidity	Temperature/Relative humidity transmitter	Temperature/Relative humidity transmitter	Vaisala HMP50Y	Vaisala HMP50Y
Soil heat flux	Soil heat flux plate	Soil heat flux plate and Thermopiles	Hukseflux HFP01SC -3	Hukseflux HFP01SC and ATDD/NOAA
Soil moisture	Soil moisture sensor	Soil moisture sensor	Delta T PR1/6	Delta T PR1/6
Soil temperature	ATDD Probe with YSI Thermistors	ATDD probe with YSI Thermistors	ATDD/NOAA	ATDD/NOAA
Surface temperature	Thermocouple	Thermocouple	Apogee IRTS-P	Apogee IRTS-P
Wind direction/speed	Anemometer	Wind sensor	R. M. Young Jr.	R. M. Young 05103
Wind speed (u' , v' , w') and sonic temperature	Ultrasonic anemometer	Sonic anemometer	R. M. Young 81000V	Gill R3

CHAPTER II

REMOTE SENSING OF EVAPOTRANSPIRATION AND THE SEBAL MODEL

2.1 Evapotranspiration

ET refers to a combined loss of water in the form of vapor from open water bodies, soil surfaces and plant systems and requires substantial amounts of energy in the form of latent heat (Hemakumara *et al.* 2003; Nagler *et al.* 2005). The flux depends on different factors in the surface-atmosphere continuum including vegetation type and growth, canopy cover and density, availability of moisture, solar radiation, and heat and vapor transport mechanisms (Mauser and Schädlich 1998; Batra *et al.* 2006). The ET process can be simplified using Eq. 1 (Dingman 2002) as:

$$ET = K_E * u(e_s - e_a) \quad \text{Eq. 1}$$

where K_E is coefficient of efficiency for vertical transport of vapor by turbulent currents of air, u is wind speed and $(e_s - e_a)$ is vapor pressure gradient between the evaporating surface and the atmosphere that drives the ET processes.

Solar radiation and the ambient temperature of the air provide the energy required to change the status of water molecules from liquid to gas while wind affects the rate of vapor removal from the evaporating surface by replacing the saturated air with drier air (Allen *et al.* 1998). The water vapor holding capacity of the air is affected by air temperature and with continuous addition of water vapor into the air, the air will ultimately become saturated and the ET process slows down. Generally, solar radiation,

air temperature, air humidity and wind speed are some of the climatological parameters that govern the ET process (Allen *et al.* 1998).

ET and the associated latent heat transfer is a major mechanism of redistributing water and energy on a global scale (Mausser and Schädlich 1998; Wu *et al.* 2006). It is also an important biophysical process supporting plant growth (Verstraeten *et al.* 2005). Water loss through ET from an ecosystem could vary significantly. For example, a study of Okavango Delta, Botswana, showed that ET accounted for a negligible amount of water loss in some areas of the region but as high as 100% water loss in others (Bauer *et al.* 2004). For efficient water resources management, hydrological processes should be understood and monitored at a river basin scale and with a high frequency (Hemakumara *et al.* 2003). Estimates of ET directly affect our ability to correctly predict or model the availability of water for irrigation and human consumption, river runoff and groundwater recharge (Nagler *et al.* 2005; Verstraeten *et al.* 2005). Study of ecosystem functions as both sources and sinks for greenhouse gases also needs ET data (Wu *et al.* 2006).

Consequently, ET data are critical in different decision-making processes, and many techniques have been developed and used for direct or indirect estimation (Yang *et al.* 2005). Techniques can be broadly classified as water balance methods (lysimeter and field and catchment water balance), flux profile models (Bowen ratio, scintillometers and eddy-correlation) and surface energy balance models (Verstraeten *et al.* 2005). These methods, based on the principles of conservation of mass, energy or a combination of both, have been deployed at different spatial and temporal scales from point and field to regional and continental levels (Verstraeten *et al.* 2005).

Field methods include an evaporation pan that estimates evaporation and a lysimeter that estimates both evaporation and transpiration. The instruments are designed to give point-level estimates of actual evaporation and ET, respectively (Kite and Droogers 2000). Water balance approaches estimate ET based on the conservation of mass. Specifically, the supply of water into a system such as precipitation or irrigation should be quantified first, followed by computation of outflow of water from the system in the forms of deep percolation into the groundwater and surface and sub-surface flow. While conceptually straightforward, the actual quantification of various terms in the water balance equation at field conditions can be difficult (Wu *et al.* 2006).

Other methods that indirectly estimate ET at field scale by quantifying the turbulent vertical moisture and heat fluxes in the atmospheric boundary layer include the Bowen ratio and scintillometer measurements. The planetary boundary layer here is defined as the lowest layer of the atmosphere in which the surface winds, which are induced by horizontal pressure gradients, are affected by the frictional resistance of the surface (Dingman 2002). The thickness of this boundary layer varies in time and space from few meters to few kilometers depending on local conditions such as topography, surface roughness, wind velocity, and the rate of cooling or heating of the surface (Dingman 2002). A scintillometer estimates the sensible heat flux in this boundary layer over a distance between several hundreds to several thousands of meters. Scintillometers, by emitting electromagnetic radiation of known wavelength, measure the turbulent intensity of air that causes fluctuation of light intensity based on the Monin–Obukhov similarity theory (Chehbouni *et al.* 2000; Hemakumara *et al.* 2003). The scintillometer-measured sensible heat flux should then be combined with the radiometric measurement

of net radiation to calculate the instantaneous latent heat flux (Hemakumara *et al.* 2003). The soil heat flux and energy used by plants for photosynthetic and metabolic activities are usually considered as negligible terms of the surface energy balance equation and are neglected from such computation (Cain *et al.* 2001; French *et al.* 2005; Verstraeten *et al.* 2005). These assumptions introduce uncertainties in the accuracy of the estimates.

The development of the scintillometer has eased the spatial scale discrepancies between point level measurement of ET and surface energy balance methods while providing aurally averaged ET estimates within one-to-five kilometers range (Kite and Droogers 2000; Hafeez *et al.* 2002). Hence, it is now possible to validate remote sensing-based models over a range of ground measured heat flux parameters. In addition, various authors have mentioned that scintillometer measurements of aurally averaged sensible heat flux are in a good agreement with eddy-correlation systems (Hemakumara *et al.* 2003). However, scintillometers often should be positioned over an elevation where there is no obstacle between the transmitter and the receiver of the signal, as this could limit their application in undulated topography (Chehbouni *et al.* 2000; Hemakumara *et al.* 2003). Moreover, a net radiometer along with a scintillometer is required for radiation measurements to compute latent heat flux. One of the main difficulties associated with this has been that footprints of scintillometer-measured sensible heat flux often are substantially bigger than footprints of net radiometer measurements; this difference can cause lack of closure in the surface energy balance and hence affect the accuracy of latent heat flux calculations (Hemakumara *et al.* 2003; refer to Chapter III of this thesis for details on how eddy-correlation measurements are used to measure vapor and heat fluxes in the turbulent atmospheric boundary layer).

While each of these methods has advantages, all operate on a fixed geographic location with observations representative over a few meters to several thousand meters. To study variations and dynamic of hydrological processes at watershed, regional or continental scales, other options are needed. It is always crucial to understand momentum, heat and vapor fluxes in the surface-atmospheric continuum over spatial scales appropriate for a particular application need, and in this respect remote sensing provides a promising future (Albertson *et al.* 1997).

2.2 Remote Sensing of Evapotranspiration

Remote sensing of ET is based on the energy conservation by accounting for radiative, conductive and convective flux of energy across the planetary boundary layer (Bastiaanssen *et al.* 1996). The fluxes of moisture and heat between the earth's surface and the atmosphere generally determines the extent and the state of this boundary layer (Nagar *et al.* 2002).

One of the most important developments in remote sensing of hydrological cycle during the last couple of decades is modeling the spatial distribution of these fluxes across the boundary layer using surface energy balance theory (Hafeez *et al.* 2002; Mohamed *et al.* 2004; Bashir *et al.* 2006). Models that have been developed include SEBAL, Surface Energy Balance System (SEBS), the resistance energy balance (RSEB), Two Source Energy Balance (TSEB), the triangle method, and the dual source model that uses multi-angular remote sensing data (Cleugh *et al.* 2007).

Despite the importance of remote sensing of hydrology in parameterization of vapor and heat fluxes, there have also been challenges to achieving this. For instance, water vapor flux and its associated stores must be estimated indirectly using algorithms

that relate measured radiance to different model input parameters (Cleugh *et al.* 2007). The main problem associated with this has been conflicting requirements for algorithms that are biophysically realistic yet simple to implement (Cleugh *et al.* 2007). For instance, aerodynamic surface (heat source) temperature is controlled by turbulent exchange processes and often required by the models (Bastiaanssen *et al.* 1996). Yet, it is often replaced by radiometric surface temperature from remote sensing measurements causing uncertainties in the modeling of sensible heat flux (Bastiaanssen *et al.* 1996; Cleugh *et al.* 2007). Validation studies of surface temperature retrieval show that surface temperature estimated by satellites is generally 1 to 3 °C higher than ground measurements (Kaleita and Kumar 2000; Wang *et al.* 2006). Moreover, some variables such as wind speed, air temperature or vapor pressure cannot be readily measured from remote sensing and therefore must be measured, estimated, or modeled using other methods (Jacob *et al.* 2002; Venturini *et al.* 2004).

2.2.1 Theoretical Basis

Turbulence in the boundary layer caused by a gradient of wind speed and by unstable vertical stratification of temperature produces chaotic eddies by which the transfer of momentum and hence transfer of heat and water vapor occurs (Dingman 2002). Eddies are rapidly ascending and descending currents of air in the turbulent part of the boundary layer above the canopy (Dingman 2002; Nagler *et al.* 2005). Remote sensing provides the possibility of modeling fluctuations in the vertical transfer of eddies, momentum, heat and vapor by measuring land surface characteristics across time and space (Dingman 2002; McCabe *et al.* 2005). Fig. 5 illustrates turbulent momentum transfer by chaotic eddies.

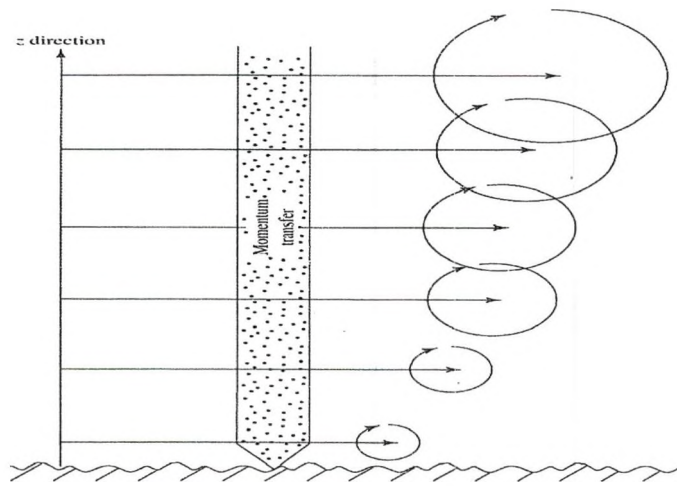


Figure 5. Conceptual diagram of momentum transfer by turbulent diffusion (From: Dingman 2002).

In the absence of advective energy transfer over land surfaces, the energy transfer by chaotic eddies across the atmospheric boundary layer can be simplified in one dimension (Schmugge *et al.* 1998; Melesse 2004) as:

$$R_n - G_0 - H - \lambda E = 0 \text{ (Wm}^{-2}\text{)} \quad \text{Eq. 2}$$

where R_n , G_0 , H and λE are net radiation, soil sensible and latent heat fluxes, respectively.

Considering the ground elements as a layer of a given thickness and responding uniformly to solar radiation, the above equation fits the ideal description of satellite remote sensing and its ground sampling unit, the pixel (Chemin, unpublished manuscript). However, the equation ignores the lateral exchange of heat between neighboring pixels. This assumption, which applies where the topography is relatively flat, is not true for areas with rapid change of landscape between neighboring pixels (Allen *et al.* 2000). Also, Eq. 2 neglects the amount of solar radiation stored and used by plants in their metabolic activities (French *et al.* 2005; Verstraeten *et al.* 2005).

2.2.1.1 Net Radiation

Net radiation, defined as the difference between the incoming and outgoing shortwave and longwave radiations at the ground surface, is the main driving force for fluxes of heat and vapor (Granger 2000; Kite and Droogers 2000; Tang *et al.* 2006). It is empirically modeled due to the scarcity of weather stations that are equipped with necessary equipment (Skeiker 2006) and is normally estimated as:

$$R_n = R_{s\downarrow}(1 - \alpha) + R_{L\downarrow} - R_{L\uparrow} \text{ (Wm}^{-2}\text{)} \quad \text{Eq.3}$$

where $R_{s\downarrow}$ is clear-sky incoming direct and diffused shortwave radiation that reaches the earth surface, $R_{L\downarrow}$ is clear-sky incoming longwave radiation, $R_{L\uparrow}$ is outgoing longwave radiation and α is planetary surface albedo.

The total amount of instantaneous solar radiation at the top of the atmosphere perpendicular to the incident rays (solar constant) approximately equals $1,367 \text{ Wm}^{-2}$. Day of the year, time of the day and latitude of a given location affect the amount of this radiation reaching the surface. Moreover, atmospheric gaseous and solid particles scatter and/or absorb some of the incoming radiation. Depending on surface albedo of ground objects, part of the radiation received at the ground surface is reflected back to the atmosphere while the rest is absorbed by different elements at the ground surface. By definition, radiation components coming toward the ground surface are assumed to be positive and conversely those going away from the surface are considered negative (Wang *et al.* 2007). The negative terms of the radiation components are the reflected shortwave and longwave and the absorbed short and longwave radiations by ground objects that are later radiated back to the atmosphere as longwave radiation depending on thermal IR emissivity of ground materials.

The accuracy of surface energy balance models in the subsequent parameterization of heat fluxes depends on the level of precision of modeling the incoming and outgoing radiation components and thereby R_n (Bastiaanssen *et al.* 1996). Hence, to minimize atmospheric interferences in accurate derivation of R_n , all energy-balance models require remotely-sensed data acquired during clear-sky conditions (Bastiaanssen *et al.* 1998; Granger 2000; Kampf and Tyler 2006).

The potential use of remote sensing data from the various earth-orbiting satellites in surface energy balance modes is dependent upon the possibilities of retrieving radiometric surface temperature from the sensors (Kustas *et al.* 2004). In general, derivatives of satellite radiance measurements in the visible, IR and thermal IR spectra such as surface albedo, vegetation indices such as Normalized Difference Vegetation Index (NDVI), surface thermal IR emissivity, and radiometric surface temperature are required to compute the terms of Eq. 3 and to subsequently parameterize heat fluxes.

2.2.1.2 Soil Heat Flux

Soil heat flux is the rate of heat storage to the ground due to conduction (Gilman 1980; Melesse 2004) and given as:

$$G_0 = \lambda_s \frac{\delta T}{\delta Z} \text{ (Wm}^{-2}\text{)} \quad \text{Eq. 4}$$

where λ_s (W(mK)⁻¹) is thermal conductivity of the soil, and $\frac{\delta T}{\delta Z}$ (Km⁻¹) is the temperature difference between the soil surface and a reference depth below the ground.

Soil heat flux is triggered by the thermal gradient in the upper part of the soil profile created by vegetation cover, amount of light interception, soil texture, soil moisture content and other factors that affect soil thermal conductivity (Verstraeten *et al.*

2005). Heat storage by ground objects is the main source of energy at night and a considerable sink during the day but only represents a small portion of the energy budget when averaged over a longer period of time (Burba *et al.* 1999). Generally, wet soils conduct less heat into deeper parts of the soil profile than dry soils due to energy absorption by soil moisture (Verstraeten *et al.* 2005). Measuring the heat flux through water bodies is more complex, and daytime heat storage by water bodies depends primarily on the amount of net radiation reaching the water surface, with water depth determining the heat storage potentials (Burba *et al.* 1999; Allen *et al.* 2000). In order to consider Eq. 4 for G_0 estimation, spatially distributed surface and subsurface soil temperature data at a reference depth are required (Gilman 1980); the above equation cannot be used in the absence of such information. Soil heat flux plates installed a few centimeters below the ground surface are commonly used to measure the soil heat flux of an ecosystem (Gilman 1980).

2.2.1.3 Sensible Heat Flux

Sensible heat flux is driven by surface-to-air temperature difference, δT (Dingman 2002). The amount of sensible heat flux, H , varies during different growth stages of a plant. From early in the growing season through its peak, H accounts for approximately 10% of R_n and this amount progressively increases as plants began to senesce consuming 20-30% of R_n (Burba *et al.* 1999). When compared to soil heat flux, the magnitude of sensible and latent heat flux fluctuates throughout the day depending on surface-to-air temperature and vapor pressure differences, respectively; however, soil heat flux is relatively constant during a 24-hour period (Consoli *et al.* 2006)

Sensible and latent heat fluxes interact with momentum flux and the former two terms could not be solved before the latter is solved (Bastiaanssen *et al.* 1998; Dingman 2002). In this case, sensible heat flux is related to turbulent momentum as:

$$\tau = \rho_{air} u_*^2 \text{ and } H = -\rho_{air} C p_{air} \delta T u_* \quad \text{Eq. 5}$$

and is represented following Ohm's law (Bastiaanssen *et al.* 1996) as:

$$H = \frac{\rho_{air} C p_{air} \delta T}{r_{ah}} \text{ (Wm}^{-2}\text{)} \quad \text{Eq. 6}$$

where τ (Nm⁻²) is momentum flux, ρ_{air} (kgm⁻³) is the air density as a function of air temperature and atmospheric pressure, u_* (ms⁻¹) is friction velocity, $C p_{air}$ (= 1004 Jkg⁻¹K⁻¹) is specific heat capacity of the air, δT (K) is surface-to-air temperature difference at reference height Z (m) above the canopy, and r_{ah} (sm⁻¹) is bulk aerodynamic resistance to heat transfer across a single surface-atmosphere layer determined according to the Monin-Obukhov stability function and given as:

$$r_{ah} = \frac{1}{k u_*} \left\{ \ln\left(\frac{Z}{Z_{oh}}\right) - \psi_h(Z, L) \right\} \quad \text{Eq. 7}$$

where k (=0.4) is the von Karman constant, Z_{oh} (m) is surface roughness length for heat transport, ψ_h is stability correction for heat transport, L (m) is the Monin-Obukhov length and given as:

$$L = -\frac{\rho_{air} C p_{air} T_0 u_*^3}{kgH} \text{ (m)} \quad \text{Eq. 8}$$

where T_0 (K) is radiometric surface temperature, g (= 9.8 ms⁻²) is the acceleration due to gravity. Expanding δT and u_* of Eqs. 5 and 6,

$$\delta T^{-1} = \frac{1}{\{T_{zoh} - T_{air(z)}\}k} \left\{ \ln\left(\frac{Z}{Z_{oh}}\right) - \psi_h(Z, L) \right\} \text{ (K}^{-1}\text{)} \quad \text{Eq. 9}$$

and

$$u_*^{-1} = \frac{1}{u(z)k} \left\{ \ln\left(\frac{Z}{Z_{om}}\right) - \psi_m(Z, L) \right\} \text{ (ms}^{-1}\text{)} \quad \text{Eq. 10}$$

where T_{zoh} (K) is aerodynamic surface temperature, $T_{air(z)}$ (K) is potential screen level air temperature at reference height, Z (m), above the canopy, u (ms⁻¹) is horizontal wind speed measurement at reference height, Z_{om} (m) is surface roughness length for momentum transport, and ψ_m is stability correction for momentum transport. Fig. 6 shows vertical distribution of wind speed over a vegetative surface following a logarithmic relation.

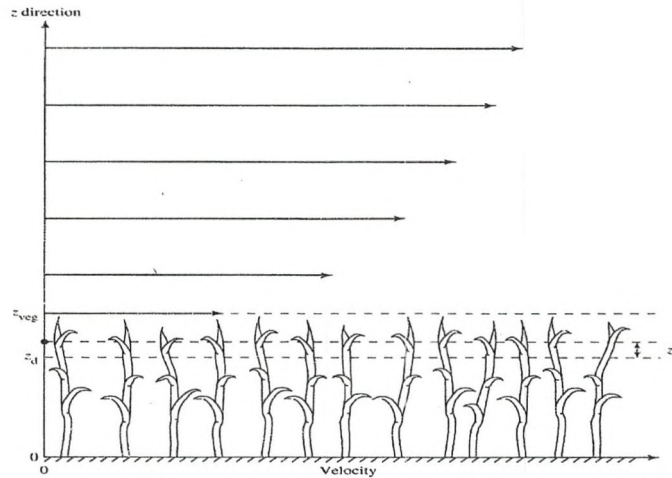


Figure 6. Vertical distribution of wind speed. In the Figure, Z_0 , Z_d and Z_{veg} refer to the roughness height, zero plane of displacement and vegetation height, respectively (From: Dingman 2002).

Models employed to estimate H are generally classified as single-source, where the whole surface is treated as a single source of H transfer to the overlying atmosphere, and dual-source models, where bare soil and plant foliage composing the surface are treated as two different sources of H (Zhan 1996; Timmermans *et al.* 2007). In a single-

source model only one combined bulk aerodynamic resistance to heat transfer, r_{ah} , is assumed, while a dual-source model assumes two separate resistance terms to H for both soil and vegetation (Timmermans *et al.* 2007). Single-source models are relatively easy to implement and are suitable for areas of homogenous vegetation cover; however, two-source models perform better when a landscape is represented by a mix of bare soil and various vegetation densities (Timmermans *et al.* 2007).

2.2.1.4 Latent Heat Flux

Latent heat of vaporization, λE , is the amount of energy consumed for a given amount of water to undergo a phase change from liquid to vapor and is a function of the temperature of water (Dingman 2002). Because of hydrogen bonding between water molecules, water has a very high latent heat of vaporization, $2.45 \times 10^6 \text{ J kg}^{-1}$ at 20°C (Dingman 2002; Hemakumara *et al.* 2003).

By quantifying R_n , G_0 and H , instantaneous λE during satellites overpass time is usually estimated as a residual component of the surface energy balance equation (Bastiaanssen *et al.* 1998). Hence, accurate modeling of ET from remote sensing measurements using surface energy balance approaches highly depend on how well R_n , G_0 and H are modeled (Bastiaanssen *et al.* 1996).

In order to estimate daily, monthly or seasonal ET, the ET fraction (Λ), defined as the ratio of total available energy consumed by ET, is usually calculated (Allen *et al.* 2000). The ET fraction is assumed to be constant during all daily satellite overpass time under conservative relative partitioning of energy fluxes (Timmermans and Meijerink 1999; Verstraeten *et al.* 2005; Kampf and Tyler 2006). In other words, the ET fraction does not vary between the mid-day and all day averages, while this might not hold true

under dynamic soil moisture and cloudy conditions (Mohamed *et al.* 2004). ET is ultimately computed as:

$$ET = \Lambda R_n \quad \text{Eq. 11}$$

2.3 The SEBAL Model

The SEBAL model was originally developed in 1995 by Bastiaanssen in Spain and Egypt using Landsat 5 TM data (Bastiaanssen 1995; Bastiaanssen 2000). It is a single-source model, and one of its main advantages is that it avoids the need for extensive ground measurement of input variables. It is designed with minimum requirements of field data with the possibility of improving the modeling result whenever more ground data are available (Timmermans and Meijerink 1999; Bastiaanssen 2000). Similar to all energy balance methods, SEBAL utilizes Eq. 2 along with regional wind speed and remotely-sensed data to parameterize R_n into H and λE (Bastiaanssen *et al.* 1998; Bastiaanssen 2000; Timmermans *et al.* 2007). In the subsequent section brief summaries of case studies that have used the SEBAL model are presented.

2.3.1 SEBAL Case Studies

The model SEBAL has been extensively used with remotely-sensed data acquired from the various existing operational satellites. While most of the studies focused on remotely-sensed data obtained from one sensor, some studies have also used SEBAL to make inter-sensor and inter-model comparisons. The model has so far been used with data obtained from Landsat, ASTER, AVHRR and suborbital airborne sensors (Bastiaanssen *et al.* 1998; Hafeez 2002; Timmermans *et al.* 2007).

In agricultural applications, SEBAL was used by Bastiaanssen (2000) with two TM images acquired in June and August to estimate H and λE in the irrigated Gediz

River Basin in western Turkey. Higher modeled ET fraction results for June as compared to August were verified using scintillometer measurements (Bastiaanssen 2000). Moreover, Melesse and Nangia (2005) used three Landsat images acquired between 1997 and 2002 to estimate heat fluxes for agricultural applications in northwestern Minnesota. The model SEBAL was used to estimate R_n and G_0 while the two source energy balance model was used to estimate H and λE . Respectively, the root mean square differences (RMSD) for the heat flux terms were found to be 21.9, 10.5, 11.9 and 6.8 Wm^{-2} (Melesse and Nangia 2005). Data obtained from the Fort Peck flux tower were used to calibrate and validate the results. Root mean square error is very sensitive to outliers because it does not take into account the scale of measurements, and the mean absolute percentage difference (MAPD) more heavily penalizes the overestimated values than the underestimated values (Melesse and Nangia 2005). Hence, a combination of both statistical parameters was used in their study in which MAPD for R_n , G_0 , H and λE modeling were found to be 19.7, 24.4, 15.1 and 12.1 %, respectively.

Scintillometers have also been used validating modeled results across a larger landscape and when using coarser spatial resolution data. Hemakumara *et al.* (2003) for instance used a large aperture scintillometer and radiometer data to compare SEBAL-modeled ET in an area of mixed vegetation at Horana Field, Sri Lanka. Average deviations of 17% and one percent ET for 10-days and one month periods, respectively, were found between *in-situ* and SEBAL-AVHRR modeled results. In the study, SEBAL overestimated the observed R_n and H by 43% and 46%, respectively (Hemakumara *et al* 2003).

Bashir *et al.* (2006) used a moisture depletion approach to compare the spatial distribution of SEBAL and four Landsat images estimated daily, monthly and seasonal ET for irrigated sorghum scheme in Gezira, Sudan. In the study, seasonal ET modeled using SEBAL was deviated by 5% from ET measured by a moisture depletion approach.

SEBAL has also been extended to model water productivity and spatial variability of crop yield using three Landsat and 12 AVHRR images for a wheat dominated area in the Yaqui Valley of Mexico (Zwart and Bastiaanssen 2007). SEBAL overestimated the eddy-correlation observed ET data for 110 days by 8.8% (Zwart and Bastiaanssen 2007). While the difference was argued to be within the range of *in-situ* measurement error, consistency of the model in yield estimates, with measured values more than modeled values by 3.5%, proved SEBAL's usefulness for further similar water productivity studies (Zwart and Bastiaanssen 2007). In the study, flux tower measurements were used to validate the combined multi-sensors (high spatial and high temporal resolutions) remote sensing data. As part of input parameters to a distributed soil-water-atmosphere-plant (SWAP) model, SEBAL was also used with two Landsat images to derive ET for agricultural water management applications in India (Ines *et al.* 2006).

The use of SEBAL has also been imperative in watershed management and ecosystem restoration efforts. To determine ET from a groundwater aquifer in Botswana, Timmermans and Meijerink (1999) used SEBAL and a series of TM and AVHRR images. SEBAL overestimated the observed ET when compared with continuous field and tower surface temperature and soil moisture data (Bowen Ratio method; Timmermans and Meijerink 1999). Similarly, a water balance method was used by Mohamed *et al.* (2004) to validate estimates of SEBAL and AVHRR inputs for a

moisture recycling project in a large swampy area in the Upper Nile basin, Sudan.

Kimura *et al.* (2007) has also used three TM images for the months of June, July, and August to estimate ET for a river basin of the Loess Plateau in China. The study found a RMSD of 0.17 mm/day for the ET fraction.

SEBAL was used with Landsat data in South Africa for water use policy purposes (Kongo and Jewitt 2006). The study investigated the impact of adapting water use innovations in a predominantly agricultural area on catchment ecology and hydrology (Kongo and Jewitt 2006). Moreover, SEBAL was also used to evaluate wetland restoration efforts by monitoring seasonal and yearly changes of ET for multiple years in Glacial Ridge National Wildlife Refuge, a wetland restoration site in Minnesota (Oberg and Melesse 2006).

Higher resolution (12 m) airborne data collected in the visible, near IR and thermal IR wavelengths by Thermal IR Multi-spectral Scanner (TIMS) and TM Simulator (TMS) instruments were used in sub-humid grassland and semi-arid rangeland of the Southern Great Plains (Timmermans *et al.* 2007). Respectively the RMSD values for SEBAL-modeled R_n , G_0 , H and λE were found to be 44, 29, 49 and 70 Wm^{-2} when compared to four flux towers' observed data (Timmermans *et al.* 2007). In the study, discrepancies in H modeling increased in order of 100 Wm^{-2} over full modeling domain even with the use of such higher-resolution remotely-sensed data, (Timmermans *et al.* 2007).

Some studies have also focused on inter-surface energy balance model comparisons for better parameterization of heat fluxes because of mixed performance of SEBAL. For instance, French *et al.* (2005) used ASTER data to compare SEBAL with

TSEB over an experimental site in central Iowa (Soil Atmosphere Coupling Experiment, SMACEX). Compared to half-hourly averaged data from eight flux towers, SEBAL performed poorer than TSEB in H modeling with mean deviations of 89 Wm^{-2} and 7 Wm^{-2} , respectively. Both models, however, agreed within 20 Wm^{-2} over a low H region (French *et al.* 2005). Despite higher discrepancies observed in H estimates (up to 150 Wm^{-2} for SEBAL as compared to TSEB (up to 35 Wm^{-2}), estimates of λE were better for SEBAL than for TSEB with mean deviations of one and 89 Wm^{-2} , respectively (French *et al.* 2005). At a flux tower point comparison, SEBAL showed higher agreement with flux tower observed λE data with deviations of 10 Wm^{-2} as compared to 50 Wm^{-2} for TSEB. Moreover, using measured incoming radiation and calibrated spatial albedo data as an input to the model, R_n modeling by SEBAL showed an average deviation of -31 Wm^{-2} (French *et al.* 2005). On top of the absence of energy balance closure observed and uncertainties in footprint approximation, SEBAL's failure to fully distinguish cold and hot areas of the study site was argued to be the main reason for inaccurate modeling of H by the model (French *et al.* 2005).

Finally, with increases in the application of SEBAL for various studies under various ecosystems and topographic settings, recent studies have also concentrated on refining the model's parameters by focusing on some of the assumptions in an attempt to improve the parameterization of the heat flux terms. Accordingly, Koloskov *et al.* (2007) used SEBAL to investigate the pivotal role the Monin-Obukhov length (L) plays in calculating ET from remotely-sensed data for a short-season cotton crop in southern Kazakhstan. The study demonstrated an alternative way to derive ET fraction by

separating the L term without a time-consuming iterative procedure of sensible heat flux estimation (Koloskov *et al.* 2007).

In summary, the above-mentioned studies indicate the wide spectrum of SEBAL applications from pure research to applications in agriculture and water resources management and drafting water management policies. Modeling of heat fluxes and ET by SEBAL showed mixed results when validated across a landscape and at a point. In addition to differences in spatial and spectral resolutions, heterogeneity of land surface elements *i.e.* magnitude and aerial extent of existing surface conditions contrasting within a modeling grid are some of the main reasons for the mixed results (Kustas *et al.* 2004).

2.3.2 Data and SEBAL Methods

Multi-spectral surface reflectance and thermal IR emittance data derived from seven bands of Landsat and for MODIS; MOD09GHK and MOD11A1 products were used to derive the components of Eq. 2. The regional wind speed measurement during the satellites overpass time was obtained from flux towers located in the study area.

Appendix C describes the two MODIS products. SEBAL parameters of the selected cold and hot reference pixels are also presented in Appendix D.

2.3.2.1 Net Radiation

2.3.2.1.1 Net Shortwave Radiation

The amount of shortwave radiation reaching the earth's surface was empirically calculated (Gutman 1988) as:

$$R_{s\downarrow} = G_{SC} * \cos \theta * d_r * \tau' \text{ (Wm}^{-2}\text{)} \quad \text{Eq. 12}$$

where G_{SC} is the solar constant, $1,367 \text{ Wm}^{-2}$, d_r is the inverse of the square of the relative distance of the earth-sun calculated as:

$$d_r = 1 + 0.033 \cos\left(DOY \frac{2\pi}{365}\right) \quad \text{Eq. 13}$$

where DOY is Julian date when the images were acquired, τ' is one-way atmospheric transmittance and was empirically derived from DEM for cloud-free days (Wu *et al.* 2006) as:

$$\tau' = 0.75 + 2 * 10^{-5} DEM \quad \text{Eq. 14}$$

where DEM is a 30 m-resolution U.S. Geological Survey (USGS) digital elevation model acquired by Shuttle Radar Topographic Mission (SRTM), and θ is solar incident angle.

Assuming the surface to be Lambertian, which is considered to be a perfect diffuse reflector, reflecting equally in all viewing directions, a correction was made to avoid differential illumination caused by orientation (slope and aspect) of the surface (Allen *et al.* 2000) as:

$$\cos \theta = \sin(\delta) \sin(\phi) \cos(s) - \sin(\delta) \cos(\phi) \sin(s) \cos(\gamma) + \cos(\delta) \cos(\phi) \cos(s) \cos(\omega) + \cos(\delta) \sin(\phi) \sin(s) \cos(\gamma) \cos(\omega) + \cos(\delta) \sin(\phi) \sin(s) \sin(\omega) \quad \text{Eq. 15}$$

where δ is declination of the earth, negative during winter and positive during summer in northern hemisphere, ϕ is latitude of the site, s is slope in radian, γ is surface azimuth angle, and ω is hour angle, zero during solar noon, negative and positive in the morning and afternoon hours, respectively. The same DEM was used in Eqs. 14 and 15; for MODIS it was re-sampled (using nearest neighbor method) to a pixel size of 500 m, while for Landsat the original pixel size (30 m) was maintained. Both slope and aspect were computed in degrees where 90°, 180°, 270° and 360° represented east, south, west, and north facing slopes, respectively, and 361° represented flat topography with no slope.

Surface reflectance was used to derive the outgoing shortwave radiation.

Respectively, narrow band surface reflectance was converted to broadband surface reflectance for both Landsat and MODIS (Liang *et al.* 2002) as:

$$\alpha_{Landsat} = 0.356\alpha_1 + 0.130\alpha_3 + 0.373\alpha_4 + 0.085\alpha_5 + 0.072\alpha_7 - 0.0018 \quad \text{Eq. 16}$$

and

$$\alpha_{MODIS} = 0.160\alpha_1 + 0.291\alpha_2 + 0.243\alpha_3 + 0.116\alpha_4 + 0.112\alpha_5 + 0.081\alpha_7 - 0.0015 \quad \text{Eq. 17}$$

where $\alpha_{1,2,3,\dots}$ is surface reflectance measured by the sensors in the respective bands.

All of the Landsat images were corrected for atmospheric and haze effects using the atmospheric correction module (ATCOR) in ERDAS Imagine 8.7[®] (Leica Geosystems, Atlanta) before the computation of surface albedo. In the case of MODIS, MOD09GHK was used to compute the outgoing shortwave radiation. The product provides estimates of surface reflectance for the first seven channels as it would be measured at ground level in the absence of atmospheric scattering and absorption, and it has been validated and is ready for use in various scientific studies (USGS 2006). Before the computation of surface albedo, the product was re-projected from a sinusoidal to a Universal Transverse Mercator-World Geodetic System (UTM WGS1984) projection, Zone 13 for Brookings and Zone 14 for Fort Peck. MODIS re-projection tool (MRT[®]) and ERDAS were used, respectively, to re-project and re-sample the products to a common pixel size of 500 m.

Net shortwave radiation was then computed as:

$$R_s = R_{s\downarrow} (1 - \alpha) \text{ (Wm}^{-2}\text{)} \quad \text{Eq. 18}$$

2.3.2.1.2 Net Longwave Radiation

The amount of net longwave radiation was also computed by subtracting the outgoing from the incoming longwave radiation term as:

$$R_{L(net)} = R_{L\downarrow} - R_{L\uparrow} \text{ (Wm}^{-2}\text{)} \quad \text{Eq. 19}$$

Longwave clear-sky atmospheric emissivity, surface temperature and thermal IR emissivity were used to compute the net longwave radiation. Accordingly, incoming longwave radiation was first computed as:

$$R_{L\downarrow} = \varepsilon_a \sigma T_a^4 \text{ (Wm}^{-2}\text{)} \quad \text{Eq. 20}$$

where ε_a is clear-sky emissivity of the atmosphere and given by Allen *et al.* (2000) as:

$$\varepsilon_a = -0.85(\ln \tau')^{0.09} \quad \text{Eq. 21}$$

σ is the Stefan-Boltzman constant, $5.67 \times 10^{-8} \text{ Wm}^{-2}\text{K}^{-4}$, and T_a (K) is reference air temperature and it was estimated from pixels with the coldest surface temperature and higher NDVI. For Landsat, NDVI was computed as:

$$NDVI_{Landsat} = \frac{IR - RED}{IR + RED} \quad \text{Eq. 22}$$

where, respectively, IR and RED are surface reflectance in the near IR (band 4) and red (band 3) portion of the surface spectrum observed by both Landsat 5 TM and Landsat 7 ETM+. Reflectance from channels one and two of MOD09GHK were used to derive NDVI for MODIS (Nagler *et al.* 2005) as:

$$NDVI_{MODIS} = \frac{Channel2 - Channel1}{Channel2 + Channel1} \quad \text{Eq. 23}$$

To ensure consistency in the estimates of NDVI, a linear conversion of NDVI between Landsat and MODIS was done (Steven *et al.* 2003) as:

$$NDVI_{TM} = 1.002NDVI_{MODIS} - 0.012 \quad \text{Eq. 24}$$

and

$$NDVI_{ETM+} = 1.023NDVI_{MODIS} - 0.013 \quad \text{Eq. 25}$$

The outgoing longwave radiation was then computed as:

$$R_{L\uparrow} = \varepsilon_s \sigma T_0^4 \quad (\text{Wm}^{-2}) \quad \text{Eq. 26}$$

where ε_s is surface thermal IR emissivity, a dimensionless ratio of the radiant emittance from a grey body to the emittance of a blackbody (Dingman 2002). An empirical relationship between ε_s and NDVI was used to derive ε_s for Landsat (Lagouarde *et al.* 2002) as:

$$\varepsilon_s = 1.009 + 0.0047 \ln(NDVI) \quad \text{Eq. 27}$$

For surface temperature, wavelength adjusted radiation was then used to derive radiometric surface temperature from thermal radiance measurement of Landsat (NASA 2006) as:

$$T_0 = \frac{k_2}{\ln\left(\frac{k_1}{L} + 1\right)\varepsilon_s^{0.25}} \quad (\text{K}) \quad \text{Eq. 28}$$

and

$$L = \text{gain} * DN + \text{offset} \quad \text{Eq. 29}$$

where k_1 and k_2 are calibration constants and, $k_1 = 607.76 \text{ Wcm}^{-2}\text{sr}^{-1}\mu\text{m}^{-1}$ and $k_2 = 1260.56 \text{ K}$ for Landsat 5 TM, and $k_1 = 666.09 \text{ mWcm}^{-2}\text{sr}^{-1}\mu\text{m}^{-1}$ and $k_2 = 1282.71 \text{ K}$ for Landsat 7 ETM+, $L \text{ (Wm}^{-2}\text{sr}^{-1}\mu\text{m}^{-1})$ is spectral radiance, and DN (digital number) is quantized calibrated pixel value for Landsat band 6. Gain and offset are calibration values

of Landsat for band 6. In SEBAL applications, no thermal band correction was required for Landsat (Allen *et al.* 2000).

Air temperature decreases by approximately 6.5 °C for each km increase in elevation, and because equilibrium exists between surface and air temperatures, a similar decrease in surface temperature could be observed (Allen *et al.* 2000). Therefore, to account for the orographic effect on the retrieved radiometric surface temperature, a DEM-adjusted radiometric surface temperature over a reference horizontal plain was derived (Mohamed *et al.* 2004) as:

$$T_{0(DEM)} = T_0 + 0.0065\delta Z \text{ (K)} \quad \text{Eq. 30}$$

where $T_{0(DEM)}$ and δZ are DEM-adjusted radiometric surface temperature over a reference horizontal plain and elevation difference between a given pixel and elevation of a reference plain, respectively. Elevation for the reference plain was chosen from a representative low-lying surface around the study area of interest.

For MODIS, MOD11A1 product was used to calculate net longwave radiation. No correction was required for MODIS land surface temperature, as the product was corrected for such effects (USGS 2006). The product provides approximately one km pixel surface temperature value derived with a day/night land surface temperature algorithm using a pair of MODIS day and night time observations and yields one K accuracy (USGS 2006). The product also contains band emissivities for channel 31 and 32. An average band emissivity from channel 31 and channel 32 was used, as these channels are considered to be more stable for emissivity retrieval (Bisht *et al.* 2005). MODIS emissivity products are derived using different MODIS data as inputs to simulation algorithms and database information by the MODIS team (USGS 2006).

2.3.2.2 Soil Heat Flux

In this study, an empirical relationship between NDVI and R_n was used to estimate soil heat flux (Bastiaanssen 2000) as:

$$\frac{G_0}{R_n} = \frac{T_0}{\alpha} (0.0038\alpha + 0.0074\alpha^2)(1 - NDVI^4) \text{ (Wm}^{-2} \text{)} \quad \text{Eq. 31}$$

where G_0 (Wm⁻²), R_n (Wm⁻²), T_0 (K) and α are soil heat flux, net radiation, radiometric surface temperature and surface albedo, respectively.

2.3.2.3 Sensible Heat Flux

Sensible heat flux is the most important term of the surface energy balance equation. Consequently, precision in the parameterization of heat fluxes using remote sensing methods depends on the separation of H and λE if R_n and G_0 are computed with reasonable accuracy (Bastiaanssen *et al.* 1996; Hemakumara *et al.* 2003).

The coupling of momentum and sensible heat fluxes allows the computation of sensible heat flux by solving the momentum flux under neutral atmospheric conditions (Bastiaanssen *et al.* 1998; Dingman 2002). Assuming the buoyancy effect on the momentum flux is negligible, which is not true, local u_* in Eq. 10 and hence r_{ah} can be solved (Bastiaanssen *et al.* 1998; Koloskov *et al.* 2007). Regional wind speed and local surface roughness information are required to compute local u_* . While it is possible to retrieve wind vectors over the global ocean surface from remotely-observed reflectance in the microwave frequencies, the wind speeds over land surfaces used in this study were Brookings and Fort Peck flux tower measurements at 4 m and 3.5 m, respectively. Local surface roughness length for momentum transport was computed (Allen *et al.* 2000) as:

$$Z_{om} = 0.123 * h \text{ (m)} \quad \text{Eq. 32}$$

where h is average vegetation height around the flux tower, 0.3 m.

The calculated local u_* at the flux towers was then used to estimate wind speed at 200 m above the ground surface where the lateral movement of air is believed to be unaffected by the components of the surface roughness elements. The wind speed derived for 200 m is assumed to be constant spatially and used at each pixel to calculate the first spatially distributed u_* under the assumed neutral atmospheric conditions.

In order to calculate the distributed roughness length for heat transport in Eq. 7, and hence the distributed sensible heat flux, the distributed surface roughness length for momentum transport should be solved first. In this regard, a great deal of research was conducted to determine Z_{om} from vegetation indices and land cover information of an area. However, deriving Z_{om} at a significantly larger spatial scale for use in surface energy balance models to parameterize H is a challenge (Jia *et al.* 2003). Jasinski *et al.* (2005) stated that from the perspective of global modeling, it is not feasible to estimate the roughness parameters for each unique plant species or vegetation stand due to insufficient reference profile data. Hence, roughness data derived from land cover maps commensurate the level of detail required by energy balance models such as SEBAL (Jasinski *et al.* 2005). In addition, they have mentioned that satellite-derived estimates of vegetation height would most likely lead to improved accuracy in the roughness length fields. Generally, best guess approaches have been used in many land surface models to estimate aerodynamic roughness parameters for natural vegetation and in most cases, estimates of distributed surface roughness maps from land cover maps were found to be within acceptable ranges according to values presented in literature (Driese and Reiners 1997).

Alternatively, spatially distributed surface roughness maps can also be derived empirically by relating NDVI and reference vegetation heights (Bastiaanssen *et al.* 1998) as:

$$Z_{om} = \exp(C_1 + C_2 NDVI) \text{ (m)} \quad \text{Eq. 33}$$

where C_1 and C_2 are local constants and are dependent on vegetation type of the study area. The minimum and maximum values of Z_{om} correspond to minimum and maximum NDVI values of a particular land cover class. In this case, the minimum and maximum Z_{om} values should not exceed possible field conditions and are used in SEBAL modeling to limit the range of Z_{om} to a realistic value for a particular land cover class (Bastiaanssen *et al.* 1998; Allen *et al.* 2000). However, field information about vegetation height and the extent of cover for each vegetation type is mandatory in order to use the above equation. Retrieving this information is impossible for historical years unless previously collected ground data are available.

In this study, a 2001 USGS National Land Cover map prepared at 30 m resolution from a composite Landsat image and a 2005 one meter resolution aerial photograph of the area were used to derive surface roughness information. Each Landsat image was classified into 10 arbitrary homogenous land cover classes using an unsupervised classification scheme in ERDAS software. The 2001 map and the 2005 aerial photographs revealed no significant changes in terms of percentage of area covered by major land cover/use classes such as residential areas, grassland, cropland, grazing land and/or area covered by perennial plants like trees and shrubs. Accordingly, each of the 10 land cover classes derived from the unsupervised classification scheme was assigned a particular land cover class from the 2001 map, and the aerial photographs were used as

base maps to validate the classification process. Vegetation type commonly grown in the area was assumed from the 2001 map metadata for each of the 10 land cover classes recognized. Approximate vegetation heights from literature were assigned for each of the 10 land cover classes recognized in order to get reference Z_{om} . A similar approach was pursued for all of the images. The 2001 map used in this study has a 30 m resolution with 76% classification accuracy and was verified against ground data during classification process (USGS 2001 National Land Cover map metadata). The areas around the flux towers are dominated by short grasses and herbaceous plants with some agricultural land (Figs. 3 and 4). Considering the overall modeling domain, most of the flat topography is under agricultural practices or natural grassland. In areas where the slope is higher and along the river channels, trees and shrubs are prominent. As previously mentioned, parameterization of H is highly controlled by surface conditions of the cold and hot pixels chosen (Timmermans *et al.* 2007) and hence more emphasis was paid to surface roughness of the selected cold and hot pixels and pixels around the flux towers. Bearing in mind that the study was conducted for historical years with no available land cover map information of the site other than the 2001 land cover map and the 2005 aerial photographs, this was the best case scenario for deriving the distributed Z_{om} at the modeling scale considered.

However, once the distributed surface roughness length for momentum transport was solved, some of the challenges were:

- 1) Radiometric surface temperature used by energy balance models is frequently higher than T_{zoh} causing uncertainties in H modeling (Bastiaanssen *et al.* 1998); and

2) It is difficult to accurately relate Z_{om} and Z_{oh} using a generic approach

(Bastiaanssen *et al.* 1996).

In order to address the above-mentioned problems, the resistance term or the kB^{-1} factor is used by surface energy balance models to adjust Z_{oh} (Timmermans *et al.* 2007) as:

$$\frac{1}{kB} = \ln \frac{Z_{om}}{Z_{oh}} \quad \text{Eq. 34}$$

The values for the kB^{-1} factor range from one to 10, and omission of the term in the calculation of H results in large over-estimation of H (Lhomme *et al.* 1997).

SEBAL's assumption of a constant kB^{-1} factor of 2.3 was used in this study (Timmermans *et al.* 2007). In this case, SEBAL assumes that the deviations of the actual Z_{oh} from the specified kB^{-1} value are absorbed into the regression equation and hence avoids precise specification of Z_{oh} (and hence r_{ah}) in the calculation of H (Timmermans *et al.* 2007). The constant value assumed for the kB^{-1} factor over an entire area of interest, however, has involved uncertainties in the calculation of H , as specification of the spatially-varied kB^{-1} factor in heterogeneous land surfaces and δT in composite terrain are challenging (Bastiaanssen *et al.* 1996). For instance, the kB^{-1} values in many experiments were found to be higher over sparse vegetations and a two-layer approach performs better than SEBAL with the exception of difficulties associated with retrieving two surface temperatures for vegetation and bare soil, which could not be obtained from current operational satellites (Lhomme *et al.* 1997).

Once all the parameters required for the calculation of the spatially distributed u_* and hence r_{ah} under the assumed neutral atmospheric conditions were derived, δT was linearly computed from surface temperature by inversely relating H and δT (Bastiaanssen *et al.* 1998). The difficulty of defining the blending height at which fluxes are not affected by surface characteristics because of variation of r_{ah} and Z_{om} in space according to local conditions (in terms of soil and vegetation cover) is similarly addressed in SEBAL by linearly relating δT with surface temperature (Bastiaanssen *et al.* 1996; Timmermans *et al.* 2007). This would avoid the need for spatially-distributed screen level air temperature. Presence of full hydrological contrast, *i.e.* cold (wet) and hot (dry) pixels within an area of interest, is the main criteria for deriving δT from surface temperature (Bastiaanssen *et al.* 1998). Surface conditions of the two hydrologically-extreme pixels determine the partition of H and λE over the entire area (Timmermans *et al.* 2007). It is important to mention here that the words “cold” and “hot” in reference to pixels are relative terms, since both H and λE happen in all pixels at the same time but with different magnitude and this will always under-represent one of the two terms (Verstraeten *et al.* 2005). Following selection of the reference pixels based on NDVI and surface temperature, they were verified by visual inspection of the true color (RGB) composite image. Highly vegetated and wet areas as well as unpaved roads (unfarmed plots) were chosen as the cold and hot reference pixels, respectively. At the cold reference pixel, H was assumed to be negligible, and all the available energy ($R_n - G_o$) was consumed as λE , while at the hot reference pixel, λE was assumed to be negligible, and all the available energy ($R_n - G_o$) was converted to H (Bastiaanssen *et al.* 1998). Under the assumed cold and no-advective H conditions the value of δT is zero at the

cold pixel (Bastiaanssen *et al.* 1998). In the case of the hot pixels, local ρ_{air} , estimated $r_{ah(hot)}$ and H_{hot} (calculated from $(R_{n(hot)} - G_{o(hot)})$) were required to determine $\delta T_{(hot)}$. This allowed the calculation of the spatially distributed δT and hence the first guess of H for the entire area of interest (Allen *et al* 2000) as:

$$\delta T = aT_0 + b \text{ (K)} \quad \text{Eq. 35}$$

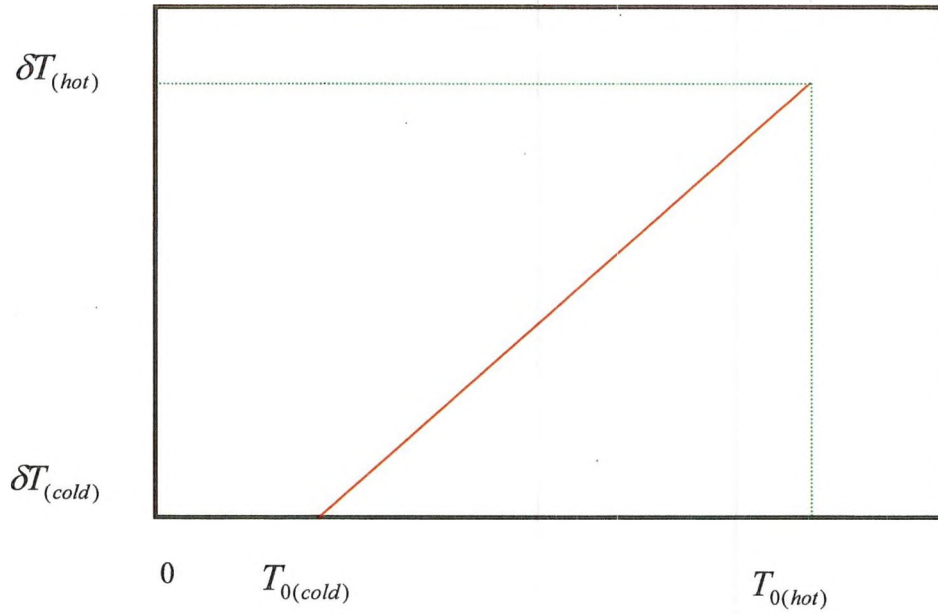


Figure 7. Relationship between δT and T_0 for cold and hot pixels.

where a and b are slope and intercept, respectively, and given as:

$$a = \frac{\delta T_{hot} - \delta T_{cold}}{T_{0(hot)} - T_{0(cold)}} \text{ or } a = \frac{\delta T_{hot}}{T_{0(hot)} - T_{0(cold)}} \text{ (K)} \quad \text{Eq. 36}$$

$$b = -aT_{0(cold)} \text{ (K)} \quad \text{Eq. 37}$$

$$T_a = T_0 - \delta T \text{ (K)} \quad \text{Eq. 38}$$

where $T_{0(cold)}$ and $T_{0(hot)}$, and δT_{cold} and δT_{hot} are radiometric surface temperature and surface-to-air temperature difference at the cold and hot reference pixels, respectively.

2.3.2.3.1 Iteration

Since the first guess of H was calculated in SEBAL for neutral atmospheric conditions, different approaches have been suggested to correct the first guess of H for non-neutral atmospheric conditions. Fig. 8 illustrates atmospheric conditions as a function of surface-to-air temperature gradients.

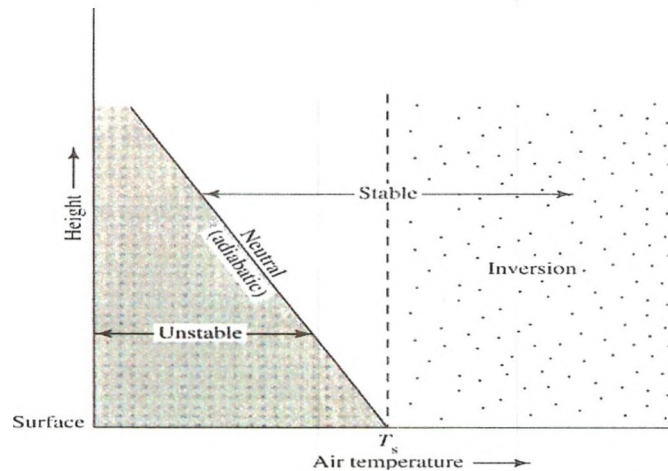


Figure 8. Unstable, neutral (adiabatic), and stable lapse rates near the surface (From: Dingman 2002).

When the actual surface-to-air temperature gradient is higher than the adiabatic gradient, the atmosphere is unstable, and vertical turbulent transfer of heat is enhanced by buoyancy effect (Dingman 2002). On the other hand, when the gradient is lower than the adiabatic gradient, the atmosphere is stable, and heat transfer is suppressed by buoyancy effects. Inversions are stable gradients whereby the air temperature increases with height (Dingman 2002).

Iterative procedure using; H , u_* and L ; H , u_* and r_{ah} ; H , u_* and temperature scale; all aimed at establishing a convergence on H based on calibration steps to establish a linear relationship between surface and air temperatures obtained from cold and hot pixels have been suggested in various studies (Koloskov *et al.* 2007). In this

study, stability correction terms for heat transport, ψ_h , and for buoyancy effect on the momentum flux, ψ_m , as presented in Koloskov *et al.* (2007) were used.

Accordingly, the Monin-Obukhov length, L , was calculated using Eq. 8 to determine the condition of the atmosphere. The first-guess spatially distributed ρ_{air} , H , and u_* were used for the calculation of L .

For $L < 0$ and $L > 0$ the atmosphere is assumed to be unstable and stable, respectively. Correspondingly, the following stability corrections for momentum transport were first applied for unstable and stable conditions (Koloskov *et al.* 2007) as:

$$\psi_{m(200m)} = 2 \ln \left(\frac{1 + x_{(200m)}}{2} \right) + \ln \left(\frac{1 + x_{(200m)}^2}{2} \right) - 2 \tan^{-1}(x_{(200m)}) + 0.5\pi \text{ for } L < 0 \quad \text{Eq. 39}$$

and

$$\psi_{m(200m)} = -\frac{10}{L} \text{ for } L > 0 \quad \text{Eq. 40}$$

where $\psi_{m(200m)}$ is stability correction function for momentum transport.

Based on stability of the atmosphere and hence the calculated correction factor for momentum transport, an improved second guess of u_* was then derived as:

$$u_* = \frac{u_{200m} k}{\ln \left(\frac{200}{Z_{om}} \right) - \psi_{m(200m)}} \text{ (ms}^{-1}\text{)} \quad \text{Eq. 41}$$

In addition, correction terms were also calculated for heat transport for unstable atmospheric conditions as:

$$\psi_{h(2m)} = 2 \ln \left(\frac{1 + x_{(2m)}^2}{2} \right) \quad \text{Eq. 42}$$

and for stable atmospheric conditions as:

$$\psi_{h(2m)} = -\frac{10}{L} \quad \text{Eq. 43}$$

where $\psi_{h(2m)}$ is the stability correction function for heat transport. Respectively, the terms $x_{(200m)}$ and $x_{(2m)}$ in Eqs. 39 and 42 are:

$$x_{(200m)} = \left(1 - 16 \left(\frac{200}{L}\right)\right)^{0.25} \quad \text{Eq. 44}$$

and

$$x_{(2m)} = \left(1 - 16 \left(\frac{2}{L}\right)\right)^{0.25} \quad \text{Eq. 45}$$

Finally, the improved second guess of u_* from Eq. 41 and correction factor calculated for heat transport were used to compute an improved and spatially distributed second guess of r_{ah} as:

$$r_a = \frac{\ln\left(\frac{Z_2}{Z_1}\right) - \psi_{h(2m)}}{ku_*} \quad (\text{sm}^{-1}) \quad \text{Eq. 46}$$

In the first guess of H , local ρ_{air} can be calculated using air temperature and atmospheric pressure data when available from nearby weather stations. For instance, data reported by the flux towers were considered in this study. However, at this stage, spatially distributed air temperature derived from surface temperature was used to derive spatially distributed first guess of ρ_{air} (Dingman 2002) as:

$$\rho_{air} = \frac{349.467}{T_a} \quad (\text{kgm}^{-3}) \quad \text{Eq. 47}$$

Coefficients of Eq. 35 and hence δT_{hot} were then computed using the corrected and the spatially-distributed first guess of ρ_{air} , second guess of r_{ah} and H_{hot} . This allowed the derivation of an improved estimate of δT as:

$$\delta T_{(hot)} = \frac{H_{(hot)} r_{ah(hot)}}{\rho_{air(hot)} 1004} \text{ (K)} \quad \text{Eq. 48}$$

Finally, the first guess of ρ_{air} , the second guess of r_{ah} and the second guess of δT were used to calculate the second guess of H . By calculating the Monin-Obukhov length, the loop from Eq. 39 was iterated while updating the values of $\delta T_{(hot)}$ using an updated constants a and b from the newly calculated $\rho_{air(hot)}$ and $r_{ah(hot)}$ during each iteration stages. This continued until convergence of H based on aerodynamic stability was attained. Normally no more than five iterations are required to derive an accurate value of L for > 98% of given pixels (Koloskov *et al.* 2007).

In summary, limitations still exist in the derivation of H for various reasons. Several H models have been developed that give acceptable results. However, only a few studies have compared the performance and applicability of these models to different landscapes (Zhan *et al.*, 1996). Moreover, deriving δT from radiometric surface temperature could yield up to > 5 °C error in area with contrasting roughness and vegetation stress conditions for which an error of one degree could lead to an approximate heat flux modeling error of 50 Wm⁻² (Timmermans *et al.* 2007). It is therefore paramount to determine the possible uncertainties involved in using the various input data and assumptions in using surface energy balance models. A sensitivity analysis of SEBAL to input parameters conducted by Timmermans *et al.* (2007) showed that the

model is most sensitive to δT followed by NDVI with uncertainty in selecting the cold and hot pixels that could result in H estimation error of 20-25%. Derivation of δT depends on r_{ah} of the hottest pixel selected and hence the linear relationship is highly governed by surface conditions of the hot pixel. Consequently, errors introduced at the hot pixels propagate into the regression equation of δT that can significantly affect flux estimation in areas that have different moisture and roughness characteristics than the hot pixels (Timmermans *et al.* 2007).

2.3.2.4 Latent Heat Flux

Under the assumption that the energy storage by the canopy is negligible, ET (also denoted as λE) was then calculated as a residual term of Eq. 2 (Wang *et al.* 2006).

CHAPTER III

FLUX TOWERS AND STATISTICAL ANALYSIS

3.1 Measurement of Flux Tower

Heat and vapor flux measurements by eddy-covariance methods have been used to validate modeling results using remotely-sensed data as input to surface energy balance models. Flux towers located in Brookings, SD, and Fort Peck, MT, were used in this study to validate the SEBAL-modeled fluxes of net radiation, soil sensible and latent heat. Flux tower measurements using eddy-covariance are weighted averages of upwind side surface flux, and flux footprint refers to those pixels that are contributing to the measured flux in the upwind direction (Kim *et al.* 2006). The eddy-covariance method measures fluxes of heat and vapor in the boundary layer over a representative homogenous landscape scale. This method was designed to calculate a covariance between instantaneous fluctuations in vertical wind speed, and air temperature and water vapor density that are measured at high frequency above the canopy (Wever *et al.* 2002; Nagler *et al.* 2005; Finnigan 2006). However, studies of measurements by a global network of more than 400 micrometeorological eddy-covariance flux towers showed a general lack of energy closure (Wever *et al.* 2002; Verstraeten *et al.* 2005). The actual errors vary among different land cover types. The closure issue is partly attributable to the differences in footprints for averaging net radiation and soil heat flux (located close to the instrument tower) as compared to sensible and latent heat fluxes (relatively larger and located in the upwind direction; Wever *et al.* 2002; Nagler *et al.* 2005). Moreover,

although eddy-covariance is regarded as the most precise method of measuring area-averaged sensible heat flux at scales of 100 m to one kilometer, the equipment is expensive and must be calibrated and verified for each site and hence requires skilled operational staff (Hemakumara *et al.* 2003; Nagler *et al.* 2005).

3.2 Footprint Analysis

Footprint functions are estimates of relative location and strength of passive mass and/or heat flux sources. Different factors govern the size, location, and orientation of the footprints (Hsieh *et al.* 2000; Fig. 9).

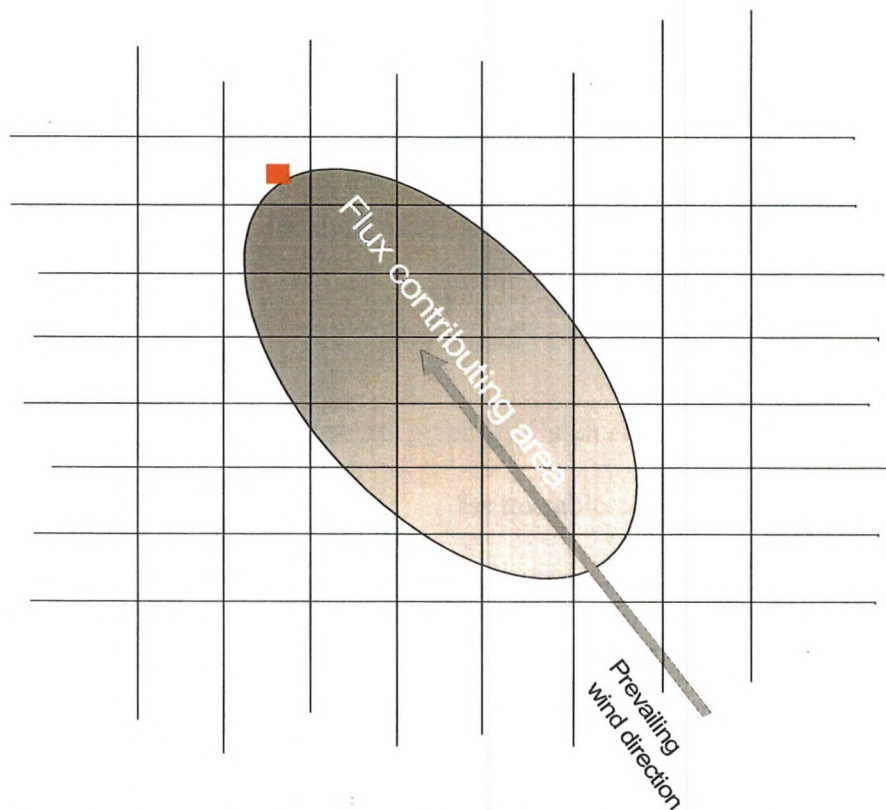


Figure 9. Orientation and strength of flux contributing area to an arbitrarily located flux tower in relation to wind direction: The darker the color, the higher the contribution.

Analytical solutions to the advection-diffusion equation, the Lagrangian stochastic simulation and large-eddy simulations are some of the flux footprints functions that are used to determine the integrated upwind side flux source (Kim *et al.* 2006). The

last two approaches are used for footprint determination in complex and heterogeneous land cover types and landscapes (Kim *et al.* 2006).

In validating results of heat fluxes modeling, an approximate analytical model for footprint estimation proposed by Hsieh *et al.* (2000) was used to determine an approximate footprint area in the upwind direction of the flux towers. In addition to being simple, the model avoids the shortfall of most footprint models by taking into account the relationship between footprint, atmospheric stability, flux tower (observation) height and surface roughness information (Hsieh *et al.* 2000; Timmermans *et al.* 2007). The model was developed based on output result from the Lagrangian stochastic dispersion model and was found to be comparable to detailed Eulerian and Lagrangian models with good agreement against measured water vapor flux (Hsieh *et al.* 2000).

Accordingly, the peak location of the footprint, x (m), was estimated as:

$$x = \frac{DZ_u^P |L|^{1-P}}{2k^2} \quad \text{Eq. 49}$$

where D and P are similarity constants given by Hsieh *et al.* (2000) as:

$D = 0.28; P = 0.59$	for unstable conditions
$D = 0.97; P = 1$	for near neutral and neutral conditions
$D = 2.44; P = 1.33$	for stable atmospheric conditions

$$\text{Near neutral conditions is met when } \left| \frac{Z_u}{L} \right| < 0.04 \quad \text{Eq. 50}$$

where L (m) and k are the Monin-Obukhov length and the von Karman constant, respectively.

Z_u (m) is a combined length scale of Z_m and Z_0 , and was calculated (Hsieh *et al.* 2000) as:

$$Z_u = Z_m \left(\ln \left(\frac{Z_m}{Z_0} \right) - 1 + \frac{Z_0}{Z_m} \right) \quad \text{Eq. 51}$$

where Z_m (m) is flux tower (observation) height and Z_0 (m) is zero plane of displacement calculated as:

$$Z_0 = \frac{2}{3} h \quad \text{Eq. 52}$$

where h (m) is average vegetation height.

Presented by the model, the footprint as a function of fetch-to-height ratio was also calculated as:

$$f(x, Z_m) = \frac{1}{k^2 x^2} DZ_u^P |L|^{1-P} \exp \left(\frac{-1}{k^2 x} DZ_u^P |L|^{1-P} \right) \quad \text{Eq. 53}$$

where, f (m^{-1}) is the footprint, and all the other terms are the same as previously mentioned. Similarly, a fetch-to-height ratio change with the above-mentioned variables was analytically determined by the model from the commonly 90% constant flux layer as:

$$\frac{x}{Z_m} = \frac{D}{0.105 k^2} Z_m^{-1} |L|^{1-P} Z_u^P \quad \text{Eq. 54}$$

Finally, the cumulative flux as a function of the above-mentioned variables was calculated as:

$$\frac{F(x, Z_m)}{S_0} = \exp \left(\frac{-1}{k^2 x} DZ_u^P |L|^{1-P} \right) \quad \text{Eq. 55}$$

where F and S_0 ($\text{gm}^{-2}\text{s}^{-1}$) are flux and source strength, respectively.

3.3 Results of Footprint Analysis

In this study, the atmospheric conditions were unstable for most of the satellite overpass time, as only three out the 19 overpass time analyzed were in stable atmospheric conditions during the measurement. This has resulted in different footprint areas for different dates and hours of measurements. Following the calculation of the peak location of the footprint as a function of atmospheric stability and a combined length scale, plus or minus one pixel (Rivas and Caselles 2004) was considered to account for errors associated with geometric correction. Consequently, different window sizes were defined for all the dates of Landsat. For instance, if the 90% flux contributing area was 50 m, a window of two Landsat pixels plus one in the upwind and one in the downwind direction and two pixels across were considered. Wind direction information from the towers was used to define the orientation of the defined windows for Landsat. An average value of the approximated footprint area contributing to the fluxes measured by the towers was then determined.

For MODIS, the pixel size was significantly larger than the 90% constant flux layer. Hence, one MODIS pixel (1 km^2) with the tower located at the center of the pixel was considered. In this way all modeled terms of the surface energy balance equation were compared against *in-situ* measurements from both flux towers. Appendix E includes details of footprint analysis.

3.4 Statistical Analysis

The following simple statistical analyses were considered to see the agreement between the modeled results versus the observed values.

1. Mean of modeled and observed values as:

$$\bar{S} = \frac{\sum_{i=1}^n S_i}{n} \text{ and } \bar{T} = \frac{\sum_{i=1}^n T_i}{n} \text{ (Wm}^{-2}\text{)} \quad \text{Eq. 56}$$

where \bar{S} is the mean of SEBAL modeled values for both towers and for all the dates, S_i is SEBAL modeled value for a particular date, n is total number of observations, \bar{T} is the mean of tower observed values for both sites and for all the dates and T_i is tower observed value for a particular date.

2. Standard deviation of modeled and observed values as:

$$\sigma_S = \left[\sum_{i=1}^n \frac{(S_i - \bar{S})^2}{n-1} \right]^{1/2} \text{ and } \sigma_T = \left[\sum_{i=1}^n \frac{(T_i - \bar{T})^2}{n-1} \right]^{1/2} \text{ (Wm}^{-2}\text{)} \quad \text{Eq. 57}$$

where σ_S and σ_T are standard deviations of SEBAL modeled and flux towers observed values for both flux towers and all the dates.

3. Mean absolute difference (*MAD*) as:

$$\frac{1}{n} \sum_{i=1}^n |S_i - T_i| \text{ (Wm}^{-2}\text{)} \quad \text{Eq. 58}$$

4. Mean absolute percentage difference (*MAPD*) as:

$$\left[\frac{\frac{1}{n} \sum_{i=1}^n |S_i - T_i|}{\bar{T}} \right] * 100 \text{ (\%)} \quad \text{Eq. 59}$$

5. Root mean square difference (*RMSD*) as:

$$\left[\frac{1}{n} \sum_{i=1}^n (S_i - T_i)^2 \right]^{1/2} \text{ (Wm}^{-2}\text{)} \quad \text{Eq. 60}$$

CHAPTER IV

RESULTS AND DISCUSSION

The focus of the study was to compare the use of Landsat and MODIS data in SEBAL for heat flux modeling. The use of remotely-sensed data from the sensors in surface energy balance models has both advantages and limitations. Temporal and spatial resolution differences are the two main factors that affect the potential utilization of the sensors considered in ET modeling. The surface energy balance equation was employed to estimate net radiation, soil sensible and latent heat fluxes. In the following sections, results of heat flux terms are separately explained in the same order in which they were modeled for both Landsat and MODIS. In addition, results of an inter-sensor comparison and sensitivity analyses to surface roughness length and surface-to-air temperature difference, and the observed absence of energy balance closure are presented at the end.

Because of variations in local winds and other meteorological conditions at the sites, footprints calculated for the time periods concurrent with the satellite overpasses were within 300 m and 100 m for the Brookings and Fort Peck sites, respectively (Appendix E illustrates details of footprint analysis). The footprints at Brookings were larger than at Fort Peck largely because Brookings has flatter topography and more homogenous land cover. While the footprints of *in-situ* flux measurements were well within a field of view of one MODIS pixel, a number of Landsat pixels covering the footprints were calculated, and values were averaged for each comparison. Moreover, mean values of aggregated Landsat pixels to the same size of one MODIS pixel were

compared against MODIS estimates. This was mainly done to see the effect of spatial heterogeneity of land surface elements on the modeled fluxes.

4.1 Landsat

The mean absolute difference and RMSD were found to be the lowest for G_0 and H modeling of Landsat than for R_n and λE . Comparatively, MAD and RMSD were the highest for λE estimates. Table 2 lists the statistics of comparisons in various energy flux components between observation and modeling for 10 Landsat data.

Table 2. Model performance statistics for Landsat: Both towers and all dates.

Flux	n	\bar{S} Wm ⁻²	\bar{T} Wm ⁻²	σ_s Wm ⁻²	σ_T Wm ⁻²	MAD Wm ⁻²	MAPD %	RMSD Wm ⁻²
R_n	10	608.4	560.7	55.6	108.1	71.13	12.7	80.7
G_0	10	79.9	74.1	26.4	33.3	35.9	48.5	41.6
H	10	174.3	186.7	58.8	82.7	41.8	22.4	50.5
λE	10	355.4	303.0	126.0	220.4	127.3	42.0	146.0

However, when the RMSD was normalized by the mean value of flux tower measured data, the ($\frac{RMSD}{\bar{T}}$) ratio was found to be 0.14, 0.56, 0.27 and 0.48 for R_n , G_0 , H and λE , respectively. The ratio is a relative measure of model performance and indicates poor agreement with flux tower observed data when the value is higher. Model performance was better for estimates of R_n followed by H and λE estimates.

4.1.1 Net Radiation

The R^2 value between the modeled and observed R_n was found to be 0.70 (Fig. 10). For each flux tower site, five Landsat images were analyzed. It was found that Landsat estimates of R_n were better at Brookings than at the Fort Peck flux tower site.

Generally, SEBAL overestimated the observed R_n where the biggest difference (127.5 Wm^{-2}) was observed on Aug. 17, 2002.

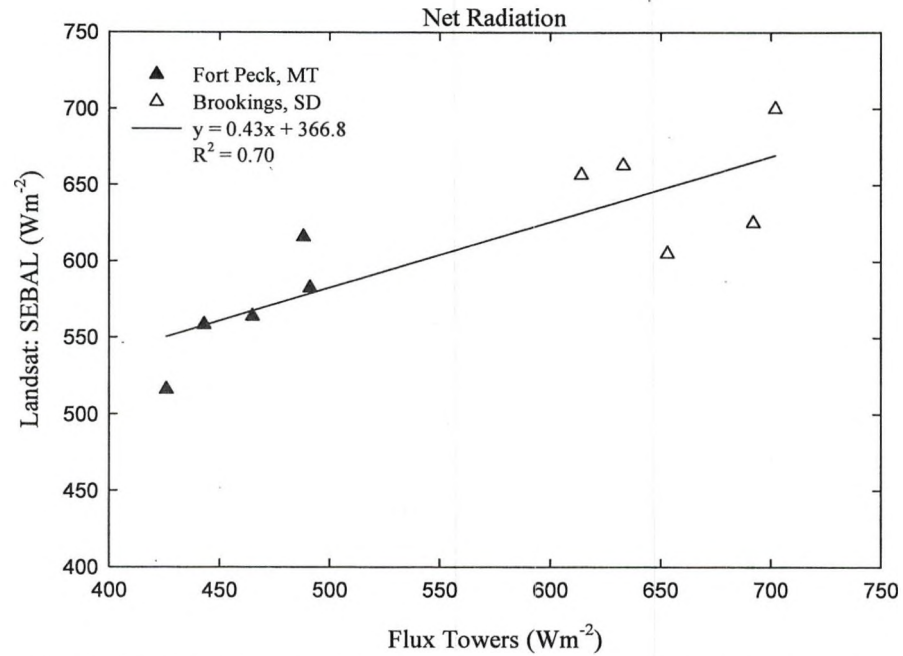


Figure 10. Comparison of R_n between the estimates by SEBAL using Landsat data and the measurements by two flux towers in Brookings and Fort Peck sites.

To see the possible source of error in R_n modeling, the incoming and outgoing terms of R_n were compared independently against flux tower data. Table 3 lists the breakdown of comparisons for R_n . It was found that, the R^2 value between modeled and flux tower observed values were higher for $R_{S\downarrow}$, $R_{L\downarrow}$ and $R_{L\uparrow}$.

Table 3. Model performance statistics of radiation components for Landsat: Both towers and all dates.

Flux	n	\bar{S} Wm^{-2}	\bar{T} Wm^{-2}	σ_S Wm^{-2}	σ_T Wm^{-2}	MAD Wm^{-2}	RMSD Wm^{-2}	R^2	Slope	Intercept Wm^{-2}
$R_{S\downarrow}$	10	920.2	861.4	58.6	93.9	58.8	70.2	0.93	0.60	401.47
$R_{S\uparrow}$	10	163.3	137.7	29.9	21.1	25.6	31.6	0.58	1.08	14.81
$R_{L\downarrow}$	10	309.4	327.8	16.5	46.8	32	34.7	0.94	0.34	197.41
$R_{L\uparrow}$	10	457.9	491.2	36.4	56.5	33.3	39.8	0.94	0.63	150.84

The outgoing shortwave radiation had the lowest R^2 value, 0.58. In addition, when the $(\frac{RMSD}{\bar{T}})$ ratio was computed for all of the net radiation terms, modeling of $R_{s\uparrow}$ showed the least agreement as compared to tower observed values with a ratio of 0.23.

Some of the uncertainties involved in the $R_{s\uparrow}$ modeling could be related to empirical approximation methods pursued for computing broadband surface albedo. Different empirical equations developed based on experiments and simulations exist to convert reflectance measured by individual bands of the various operational sensors to planetary broadband surface albedo. Calibrated under particular experimental settings, the approach may introduce errors when used in a different environmental and topographic setting. The linear conversion equations also assume linear mixing of land surface elements or a homogeneous surface, which is not always the case (Liang *et al.* 2002). Hence, poor modeling of $R_{s\uparrow}$ is attributed to uncertainties involved in using such merely generic empirical approaches. For example, surface albedo derived using a method utilized by Allen *et al.* (2000) overestimated surface albedo calculated using Liang *et al.* (2002). This indicates the need for more validation work on the various empirical equations developed and used to convert narrow-to-broad band surface albedo through local calibration of the equations using extensive field data. It is important to recall here that narrow-to-broadband surface albedo conversion equations recommended by Liang *et al.* (2002) were used to estimate $R_{s\uparrow}$ for both Landsat and MODIS.

In addition, another possible source of errors for poor modeling of $R_{s\uparrow}$ was the atmospheric correction method pursued in this study. The atmospheric correction model, ATCOR, only requires sensor calibration defaults and selection of predefined

atmospheric properties that may not be of typical for the atmospheric conditions during the satellites overpass time.

4.1.2 Soil Heat Flux

No correlation was found between SEBAL modeled and flux towers observed G_0 as shown in Fig. 11. In addition, the $(\frac{RMSD}{\bar{T}})$ ratio showed the model performed the worst in estimating G_0 .

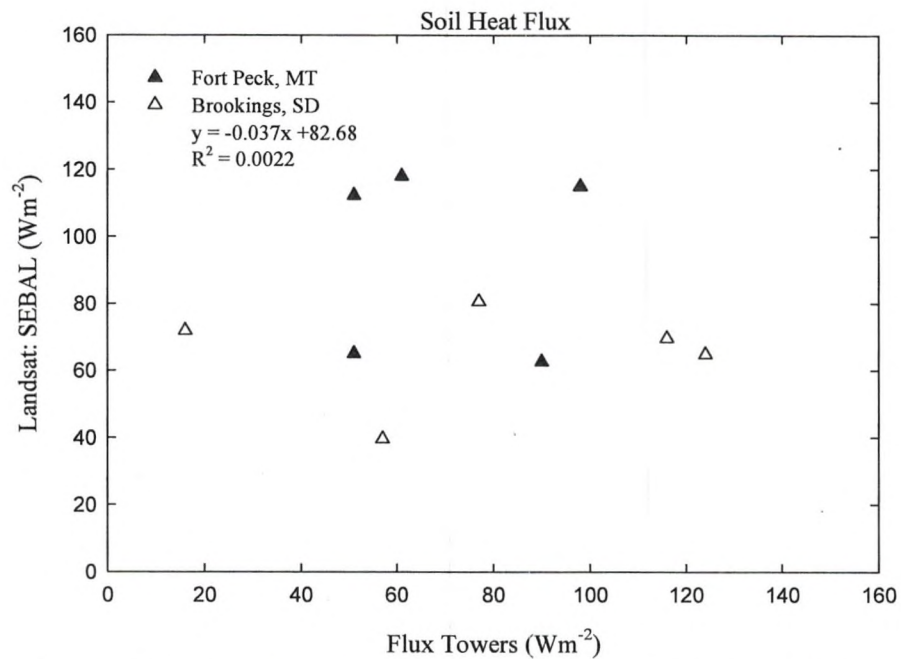


Figure 11. Comparison of G_0 between the estimates by SEBAL using Landsat data and the measurements by two flux towers in Brookings and Fort Peck sites.

When individual dates were considered, the discrepancies between modeled and observed G_0 values were within $50 Wm^{-2}$ for six out of the 10 Landsat dates analyzed, while for the rest of the dates, the discrepancies were less than $62 Wm^{-2}$, the lowest of which, $3.6 Wm^{-2}$, was found for Aug. 07, 2005, at the Brookings site.

Despite the fact that G_0 modeling showed the lowest MAD and RMSD of all the terms of Eq. 2, both statistical parameters are insensitive to scale and cannot give the

right picture of model performance. The magnitude of G_0 is usually incomparable with the magnitude of the other heat flux terms. Moreover, scaling is an issue for comparison with Landsat observations, because the measurement of G_0 , unlike its counterparts above the surface, is barely affected by the air movement and basically fixes at a point.

4.1.3 Sensible Heat Flux

The R^2 value between modeled and observed H was found to be 0.62 (Fig. 12). Next to net radiation modeling, good agreement was found between SEBAL modeled and tower observed H .

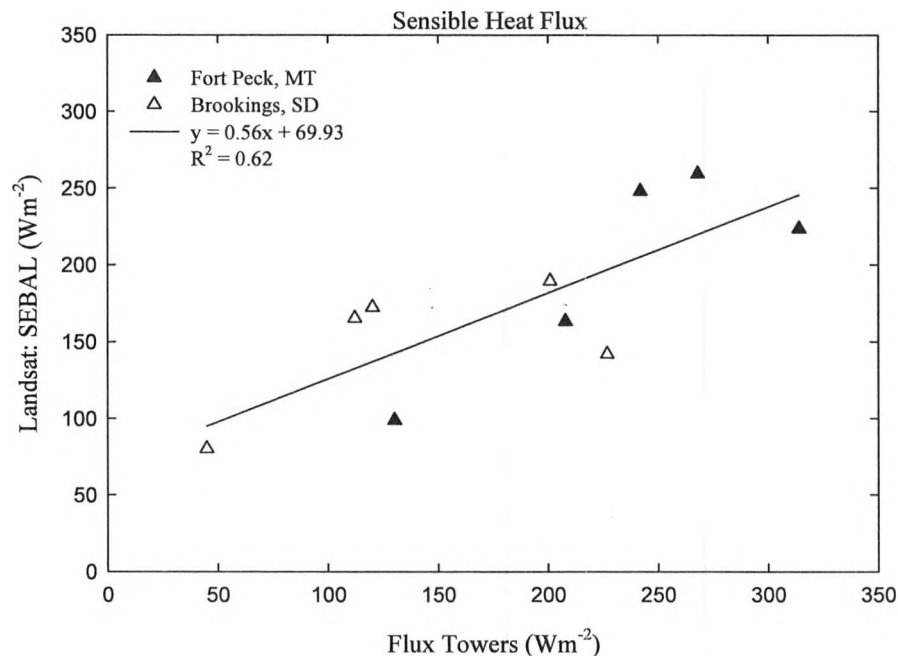


Figure 12. Comparison of H between the estimates by SEBAL using Landsat data and the measurements by two flux towers in Brookings and Fort Peck sites.

With the exception of two dates, Aug. 7, 2005, and Aug. 11, 2006, discrepancies between Landsat modeled and flux towers observed H were approximately equal to $50 Wm^{-2}$. Results showed that the aforementioned dates yielded the highest discrepancies with SEBAL underestimating the observed values by 85 and $90.5 Wm^{-2}$ at Brookings and Fort

Peck sites, respectively. The lowest discrepancy from the overall modeling domain of H was found for Aug. 4, 2006 at the Fort Peck site, where SEBAL overestimated the observed H by 6 Wm^{-2} .

The unique feature of SEBAL is its ability to derive δT with relatively high accuracy, because the iterative procedure is able to cancel out uncertainty and inaccuracy in the estimates of both the surface and the atmospheric temperatures. Hence, no correction was needed for the Landsat thermal band. However, even with better estimates of MODIS land surface temperature product, the performance of SEBAL also depends on the selection of reference cold and hot pixels. In this study, selection of the coldest pixels from water bodies was avoided due to difficulties in quantifying heat storage by water (Allen *et al.* 2000; Timmermans *et al.* 2007). Wet and vegetated areas close to water bodies were selected for Landsat. Timmermans *et al.* (2007) mentioned that there is no general consensus on how to select the hottest pixels; it is a subjective procedure, as multiple pixels with different surface conditions may satisfy hot pixel selection criterion. Similarly, selecting reference pixels from those with different Z_{om} but similar surface temperatures was a challenge in the overall modeling work. This would contribute error to the overall uncertainty in the calculation of δT and hence H .

4.1.4 Latent Heat Flux

The R^2 value between the modeled and observed λE for Landsat was found to be 0.62 (Fig. 13). The highest level of absolute discrepancy in the overall modeling domain when compared with flux tower observed data was obtained in the calculation λE , as it was always calculated as a residual term of the surface energy balance equation. Generally, it was found to be overestimated as compared to the observed values.

However, when the error was normalized by the mean value of flux observed data, relative model performance was better for λE estimates than for G_0 .

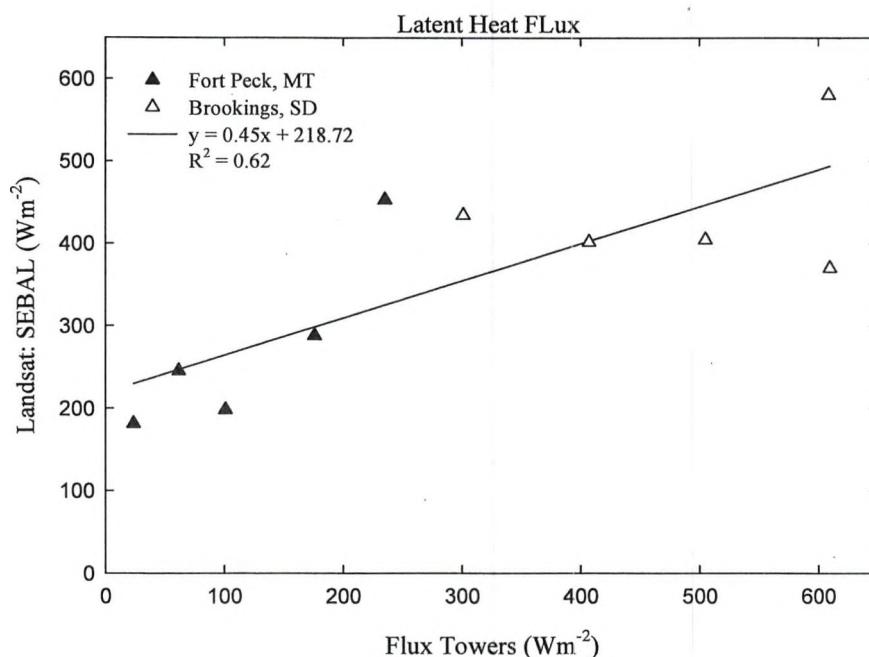


Figure 13. Comparison of λE between the estimates by SEBAL using Landsat data and the measurements by two flux towers in Brookings and Fort Peck sites.

The lowest and the highest discrepancies in λE modeling were found at the Brookings site for Aug. 4, 2004, and May 9, 2007, as SEBAL overestimated the observed values for those dates by 5.7 and 239.4 Wm^{-2} , respectively. It is important to mention here that the cold pixels used to estimate air temperature in the computation of R_n were also used for iterative derivation of H . The uncertainties associated with this assumption cancelled out in the derivation of δT . Consequently, the comparisons for λE showed improvement even with some modeling error of R_n and G_0 .

Despite the fact that some errors introduced in the modeling of R_n and G_0 were cancelled out in the subsequent calculation of H , λE still showed a higher difference when compared with observed values. This is not surprising as λE is calculated as a

residual term in the surface energy balance equation and tends to inherit the accumulated errors introduced in the calculation of other terms. Therefore, although the intended product of SEBAL and other surface energy balance models is the spatial distribution of ET, many studies have just focused on the modeling of H as opposed to λE (Timmermans *et al.* 2007).

4.2 MODIS

Similar to Landsat, independent comparisons were made for each heat flux terms modeled against flux tower data. Thus, the $(\frac{RMSD}{\bar{T}})$ ratio was found to be 0.13, 0.38, 0.45, and 0.85 for estimates of R_n , H , λE and G_0 , respectively. Modeling was better for R_n than for the other terms. Table 4 lists the statistics of comparisons in various energy flux components between observation and modeling for MODIS data.

Table 4. Model performance statistics for MODIS: Both towers and all dates.

Flux	n	\bar{S} Wm ⁻²	\bar{T} Wm ⁻²	σ_s Wm ⁻²	σ_T Wm ⁻²	MAD Wm ⁻²	MAPD %	RMSD Wm ⁻²
R_n	9	581.7	532.8	56.4	84.9	57.2	10.7	68.9
G_0	8	88.2	90.6	18.6	35.3	29.5	32.6	34.8
H	8	200.8	216.8	104.4	65.8	85.3	39.4	98.1
λE	8	286.3	188.1	152.1	148.5	144.4	76.8	159.0

4.2.1 Net Radiation

The R^2 value between the modeled and observed R_n was found to be 0.66 (Fig. 14). MODIS has better estimates of thermal IR emissivity and surface temperature products. A total number of nine MODIS images, six for Fort Peck and three for Brookings were analyzed. In the overall modeling domain using MODIS data, considerable agreement between modeled and observed values was found for R_n .

Comparing individual dates with flux tower data, MODIS estimates of R_n were better for Brookings than for the Fort Peck flux tower site. Similar to Landsat, SEBAL using MODIS data overestimated R_n . In MODIS modeling of R_n , the discrepancies were found to be within 50 Wm^{-2} for five out of the nine dates considered.

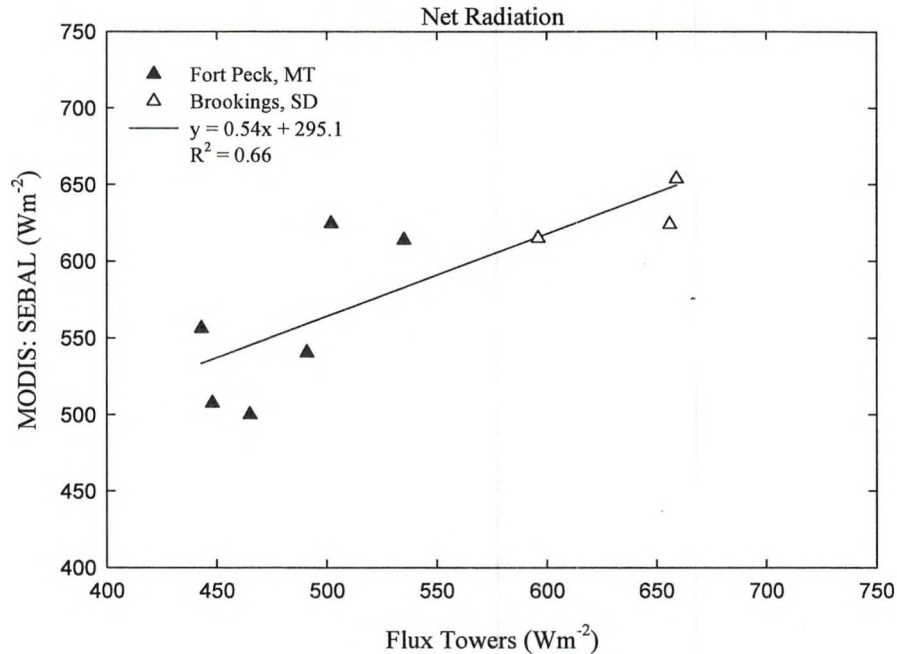


Figure 14. Comparison of R_n between the estimates by SEBAL using MODIS data and the measurements by two flux towers in Brookings and Fort Peck.

Further comparisons of net radiation components with flux tower data revealed that R^2 between modeled and observed values were higher for $R_{s\downarrow}$ and $R_{L\uparrow}$ (Table 5). Modeling of the incoming shortwave radiation does not require any remote sensing data that might affect the accuracy of its estimation. The only remote sensing data used was the 30 m resolution USGS SRTM DEM.

Table 5. Model performance statistics of radiation components for MODIS: Both towers and all dates.

Flux	<i>n</i>	\bar{S} Wm ⁻²	\bar{T} Wm ⁻²	σ_s Wm ⁻²	σ_T Wm ⁻²	MAD Wm ⁻²	RMSD Wm ⁻²	<i>R</i> ²	Slope	Intercept Wm ⁻²
<i>R</i> _{S↓}	9	894.1	840.6	54.7	65.4	52.9	56.4	0.93	0.81	216.32
<i>R</i> _{S↑}	9	166.2	133.1	34.3	15.4	34.9	41.4	0.50	1.59	44.96
<i>R</i> _{L↓}	9	336.5	331.67	24.0	48.78	24.5	33	0.58	0.38	211.86
<i>R</i> _{L↑}	9	483.0	507.1	41.1	63.3	33.1	39.8	0.77	0.57	193.5

Similar to Landsat, the outgoing shortwave radiation had the lowest *R*² value, 0.50. This was further confirmed with *R*_{S↑} having a ($\frac{RMSD}{\bar{T}}$) ratio of 0.31, the highest among the four components.

4.2.2 Soil Heat Flux

No correlation was found between SEBAL modeled and flux towers observed *G*₀ for MODIS (Fig. 15). As no significant correlation was found between modeled and observed *G*₀ values, the ($\frac{RMSD}{\bar{T}}$) ratio was not a good indicator in this case. The discrepancies between the modeled and observed *G*₀ using MODIS data were found to be within 50 Wm⁻² except for Aug. 11, 2006, in which a maximum discrepancy of 59 Wm⁻² was found at the Fort Peck site. Similarly, the lowest discrepancies in *G*₀ modeling were obtained for Aug. 12, 2003, and Aug. 7, 2005, at Fort Peck and Brookings sites with total values of 5.4 and 8.4 Wm⁻², respectively.

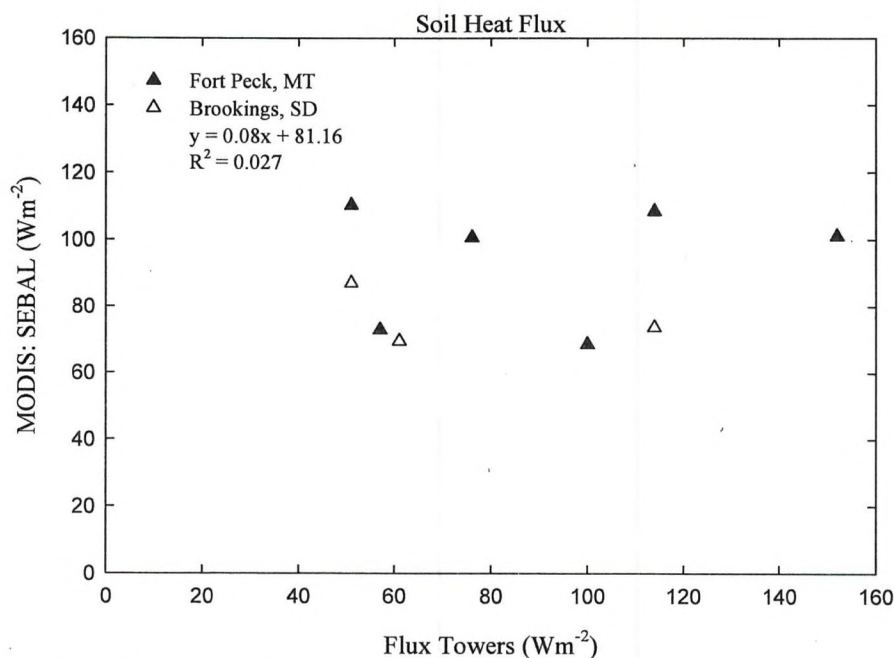


Figure 15. Comparison of G_0 between the estimates by SEBAL using MODIS data and the measurements by two flux towers in Brookings and Fort Peck sites.

Physically, soil heat flux is governed by the gradient of soil temperature profile and soil water content, neither of which can be measured by remote observations. SEBAL approximates G_0 using surface parameters such as surface temperature, broadband surface albedo and NDVI (Eq. 31). It is expected that this empirical relationship, which was developed for Gediz Basin, Turkey (Bastiaanssen 2000) under different conditions and assumptions may introduce errors in G_0 estimates when it is applied without calibration. In a similar study, applying the same equation and NOAA-AVHRR images for 13 EuroFlux towers, Verstraeten *et al.* (2005) found the best, and all sites average correlation coefficients of 0.44 and 0.01 between modeled and observed G_0 values, respectively.

4.2.3 Sensible Heat Flux

The R^2 value between modeled and observed H for MODIS was only 0.11 (Fig. 16). Generally speaking, modeling of H by MODIS performed worse than Landsat for both sites, with bigger discrepancies found for Fort Peck than for Brookings site. Next to G_0 modeling, relative model performance was found to be the lowest for MODIS H estimates.

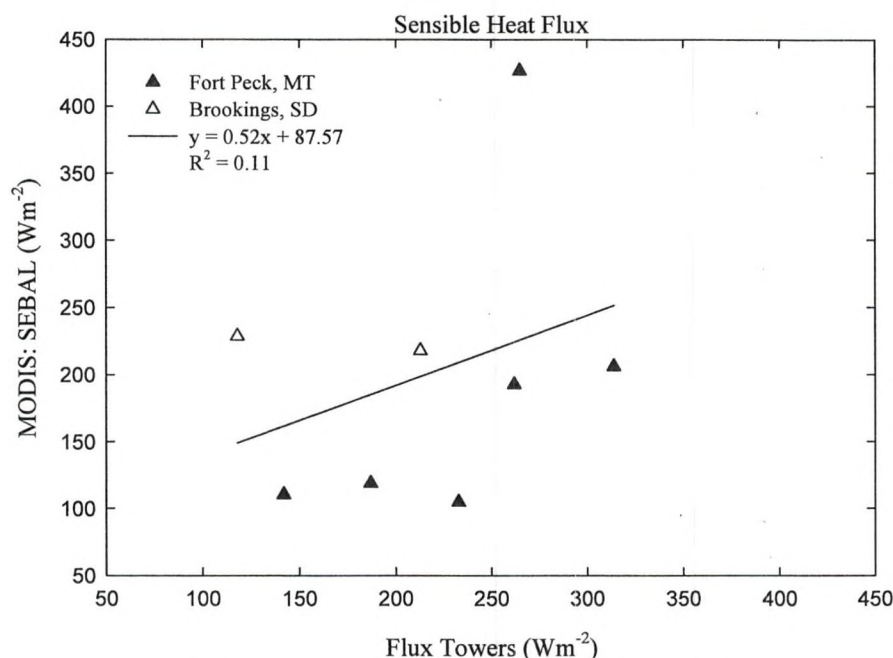


Figure 16. Comparison of H between the estimates by SEBAL using MODIS data and the measurements by two flux towers in Brookings and Fort Peck sites.

The SEBAL approach of sensible heat flux modeling in heterogeneous landscapes with different vegetations, soil, and moisture conditions would not always give accurate results. This is one of the possible reasons for poor performance of MODIS data in this study, as mixed signals of different vegetation cover and surface conditions were captured by a single pixel. This would have a pronounced effect on the modeling of H when an area with a mix of water, highly vegetated, and bare land within a single MODIS

pixel happens to represent the coldest pixels. This was particularly true for the Fort Peck site, where a single pixel covers part of the Missouri River tributary and the adjacent irrigated farms. In addition, conflict in MODIS pixel size and the flux contributing area approximated by the footprint analysis model was another possible reason for uncertainty involved in comparing MODIS modeled data with flux towers observed data.

Comparing an aerodynamic resistance–surface energy balance model and the Penman–Monteith equation, Cleugh *et al.* (2007) estimated regional ET over two strongly contrasting Australian ecosystems, a cool temperate, evergreen *Eucalyptus* forest and a wet/dry, tropical savanna. Eight-day MODIS products were used for the calculation of H . Although SEBAL was not used for modeling the heat fluxes, comparisons with flux towers-observed H revealed RMSD of 201.1, 268.3 and 235.7 for the forest, savanna and both sites combined, respectively. Moreover, the correlation coefficients between modeled and observed values were found to be 0.41, 0.22 and 0.41, respectively (Cleugh *et al.* 2007). This confirms discrepancies of heat flux modeling due to the use of coarse-resolution remote sensing data.

4.2.4 Latent Heat Flux

The R^2 between the modeled and observed values was 0.04. The highest modeling error in λE for MODIS was observed on the same date, where the biggest error was observed for H modeling. Excluding this outlier, the value improved to 0.37 (Fig. 17). Relative model performance was better for λE estimates than for H . Generally, λE was overestimated by MODIS as compared to flux tower data.

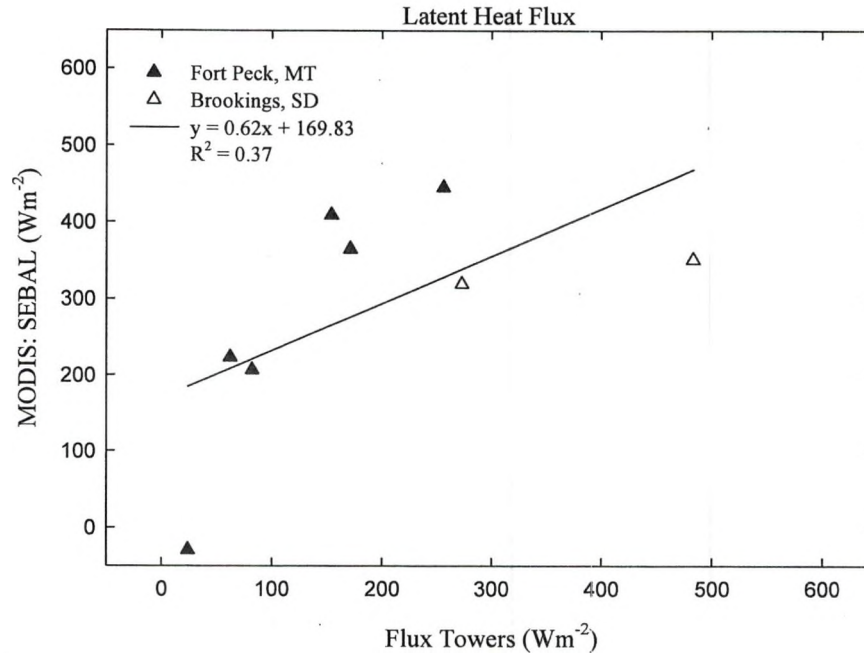


Figure 17. Comparison of λE between the estimates by SEBAL using MODIS data and the measurements by two flux towers in Brookings and Fort Peck sites.

4.3 Inter-sensor Comparison

Both Landsat and MODIS generally performed similarly when compared to the ground measurements of net radiation, *i.e.*, both sensors would over- or underestimate simultaneously, and the magnitudes of discrepancy tended to agree. For example, the same underestimated Landsat dates were also underestimated when MODIS data were used. Similar to Landsat modeling of R_n , all of the three MODIS dates sampled for the Brookings site yielded discrepancies of R_n modeling within 50 Wm^{-2} . For MODIS, the highest discrepancy in R_n modeling was found for Aug. 17, 2002, in which SEBAL overestimated the observed value by 122.5 Wm^{-2} . It is important to recall here that the highest discrepancy in R_n modeling was found for this same date when Landsat data were used. In addition, the lowest discrepancies of MODIS R_n modeling were observed for May 19, 2005 and June 23, 2005 images for which the lowest discrepancy was also

observed for the latter date when Landsat data were used. This is another indication of the consistency of R_n modeling by both Landsat and MODIS.

Although MODIS produces better estimates of surface temperature and thermal IR emissivity, the correlation with the observed radiation component is worse than for Landsat because of failure of the MODIS thermal band in capturing spatial heterogeneity of land surface elements. Net radiation was generally modeled within reasonable accuracy at both flux towers using data from Landsat and MODIS. Modeling of $R_{L\uparrow}$ and $R_{L\downarrow}$ were better for MODIS than for Landsat, although modeling of $R_{S\uparrow}$ showed the highest error, almost equal for both sensors. In addition, absence of G_0 modeling trend was observed between Landsat and MODIS (Figs. 11 and 15).

To further investigate and justify the scaling issue in comparing MODIS results with the flux towers, MODIS observations were simulated using Landsat data by aggregating Landsat pixels that are within the field of view of MODIS. Results show that net radiation modeling was found to be unaffected by spatial heterogeneity of a field of view of the sensors considered while no correlation coefficient was found for G_0 (Fig. 18 and 19). Generally, modeling of R_n was better for Landsat than MODIS, and conversely when Landsat pixels were aggregated to the same size as a MODIS pixel, modeled R_n was the only term that showed improvement against flux towers observed values. The R^2 value for R_n increased from 0.70 to 0.77. Even if distinction of land surface elements was not possible at a resolution as that of a MODIS pixel, the average R_n value taken from the aggregated Landsat pixels was still able to depict the heterogeneity of surface elements more accurately than a single MODIS pixel.

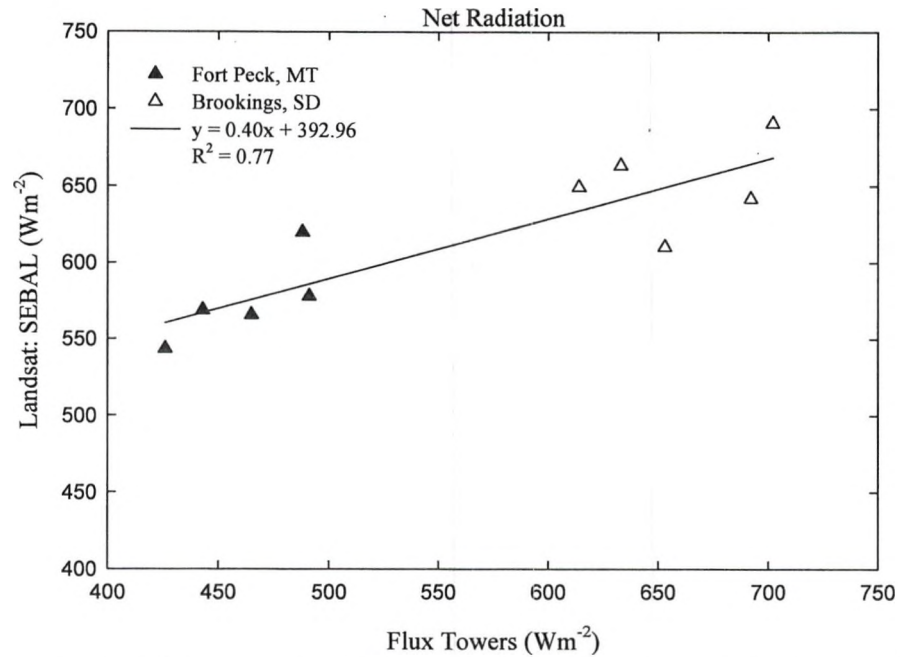


Figure 18. Comparison of R_n between the estimates by SEBAL using Landsat pixels simulated to a MODIS pixel and the measurements by two flux towers in Brookings and Fort Peck sites.

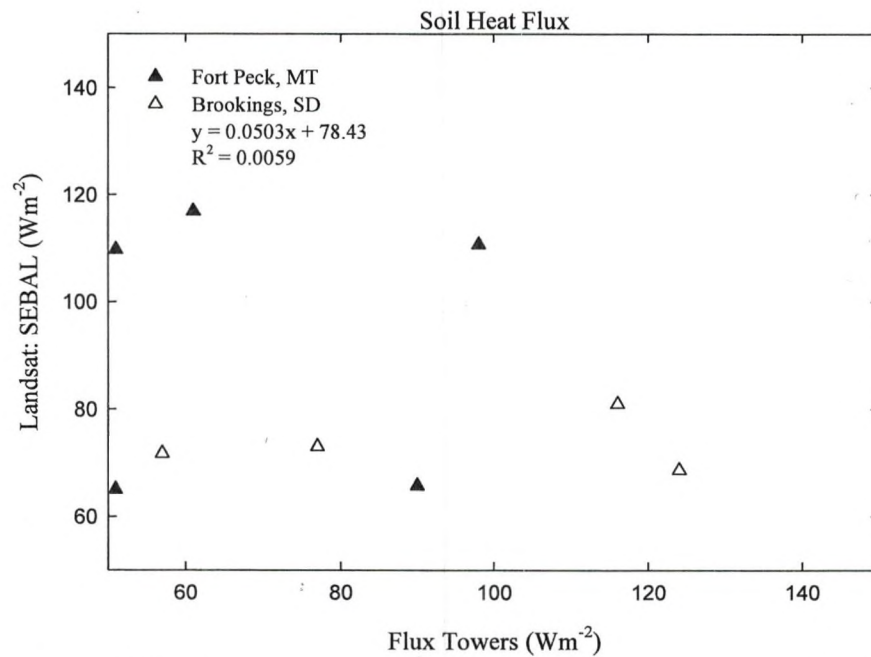


Figure 19. Comparison of G_0 between the estimates by SEBAL using Landsat pixels simulated to a MODIS pixel and the measurements by two flux towers in Brookings and Fort Peck sites.

Moreover, the R^2 value decreased from 0.62 to 0.25 for H modeling with an increase of RMSD from 50.5 to 68.3 Wm^{-2} due to Landsat pixel aggregation (Fig. 20).

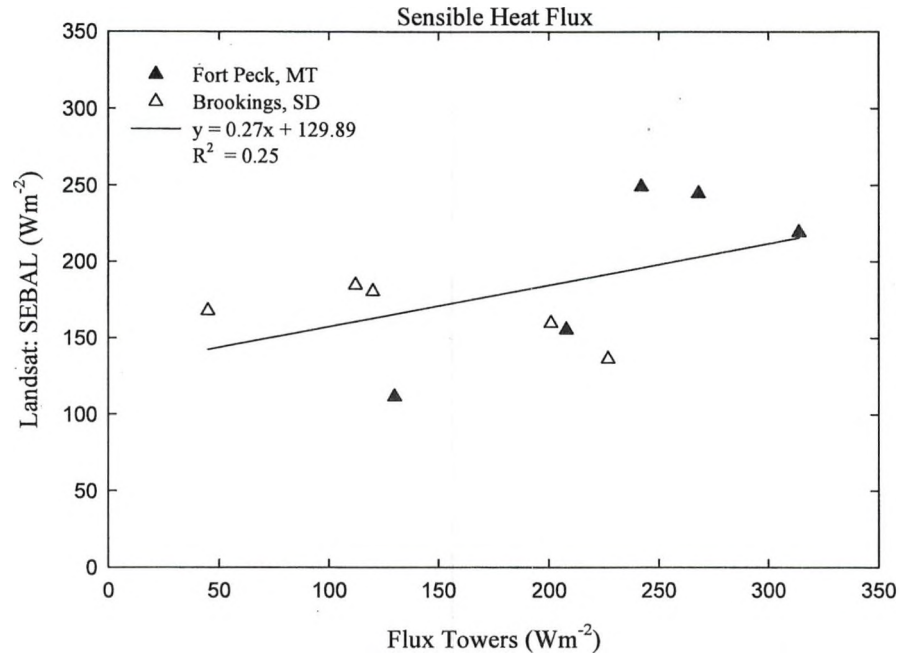


Figure 20. Comparison of H between the estimates by SEBAL using Landsat pixels simulated to a MODIS pixel and the measurements by two flux towers in Brookings and Fort Peck sites.

The above result indicates the effect of spatial heterogeneity in terms of surface conditions on H modeling. The advantage of using high spatial resolution remotely-sensed data such as Landsat is the ability to detect more land cover classes and surface conditions with the possibility of better estimation of the various input parameters that critically affect the accuracy of H modeling. As the accuracy in the modeling of H influences the level of modeling error that would ultimately be accumulated in λE calculations, the increase in the modeling error of H due to the use of low spatial resolution remotely-sensed data, such as data produced by MODIS, was significant. This was evidenced in this study where the R^2 between the modeled and observed λE values similarly decreased from 0.62 to 0.49 when Landsat pixels were aggregated to 1 km^2 (Fig. 21). Table 6 lists the statistics of comparison between flux tower measurements and aggregated Landsat pixels modeling.

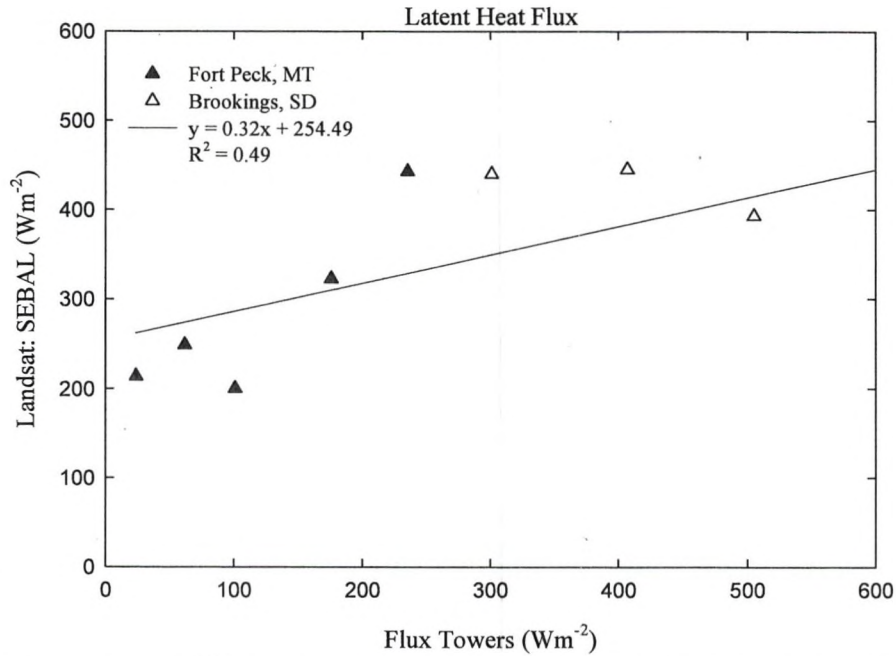


Figure 21. Comparison of λE between the estimates by SEBAL using Landsat pixels simulated to a MODIS pixel and the measurements by two flux towers in Brookings and Fort Peck sites.

Table 6. Model performance statistics for Landsat pixels simulated to a MODIS pixel: Both towers and all dates.

Flux	n	\bar{S} Wm ⁻²	\bar{T} Wm ⁻²	σ_s Wm ⁻²	σ_T Wm ⁻²	MAD Wm ⁻²	MAPD %	RMSD Wm ⁻²
R_n	10	613.2	560.7	48.5	108.1	73.2	13.1	84.4
G_0	10	83.9	74.9	21.4	31.7	30.5	40.7	35.9
H	10	186.4	190.6	46.6	79.5	54.2	28.4	65.2
λE	10	345.7	287.6	96.6	215.2	154.7	53.8	164.0

A similar study, known as the SMEX02/SMACEX study, was conducted by Kustas *et al.* (2004) in central Iowa using TM and ETM+ along with MODIS and AVHRR data and a two-source canopy model. Flux measurements from 14 flux towers and by a Twin Otter aircraft flown within half an hour of the overpass time of Landsat were used to validate the modeling results. Extensive field vegetation data, Normalized Difference Water Index (NDWI) derived from bands 4 and 5 of Landsat, land surface temperature, wind speed, air temperature and a land cover classification map were used as inputs to the model. The modeling results using Landsat data were validated by

averaging two to four pixels upwind of the flux towers, pixels along the aircraft track and pixels up to two km upwind the aircraft track. It was found that all the heat flux terms were modeled within discrepancies of 50 Wm^{-2} . Moreover, as the two-source model used in the study is sensitive to surface temperature and fractional vegetation cover (Kustas *et al.* 2004), the effect of spatial resolution difference in modeling the heat fluxes was tested at 60 m, 120 m, 240 m and one km levels. Surface temperature products from MODIS and AVHRR were thermally sharpened at the MODIS visible band to get the 240 m resolution surface temperature product. The study demonstrated that spatial distribution of heat fluxes, particularly of λE , was affected at one km level. The standard deviations and coefficient of variation for all the heat flux terms in general and for H and λE in particular decreased by more than 50 % when using the coarser resolution data as opposed to data from Landsat. Furthermore, information pertaining to corn and soybean fields was lost at this level when compared to Landsat estimates, and distinction between the two fields was not possible (Kustas *et al.* 2004). Their study compared the effect of spatial resolution difference on heat flux modeling by comparing the modeling output across the region.

In addition to the previously mentioned way of evaluating the scaling issues, direct comparisons were also made between heat flux modeling of a MODIS pixel and Landsat pixels aggregated to 1 km^2 (Figs. 22 to 25).

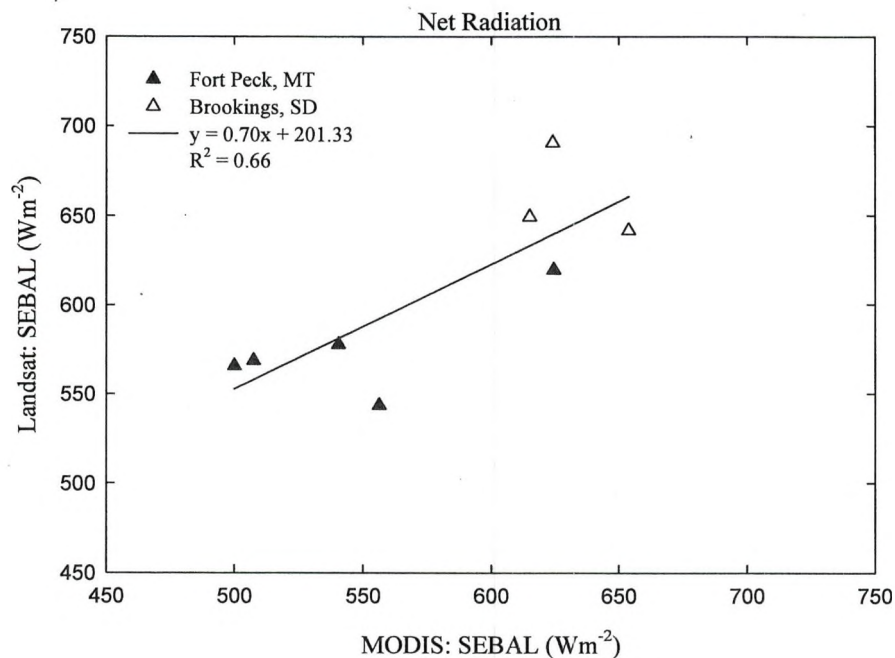


Figure 22. Comparison of R_n between the estimates by SEBAL using Landsat pixels simulated to a MODIS pixel and a MODIS pixel for Brookings and Fort Peck sites.

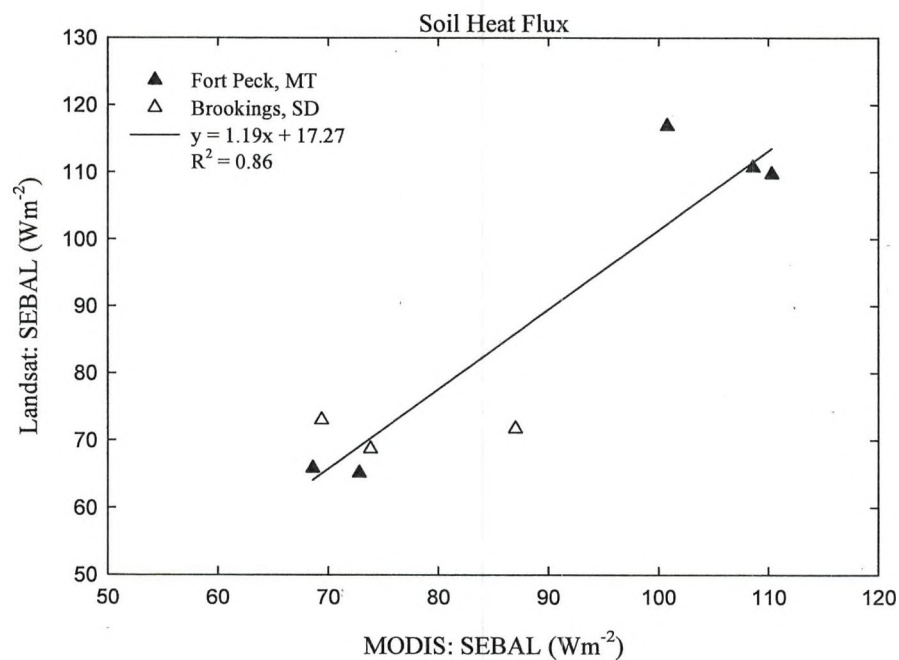


Figure 23. Comparison of G_0 between the estimates by SEBAL using Landsat pixels simulated to a MODIS pixel and a MODIS pixel for Brookings and Fort Peck sites.

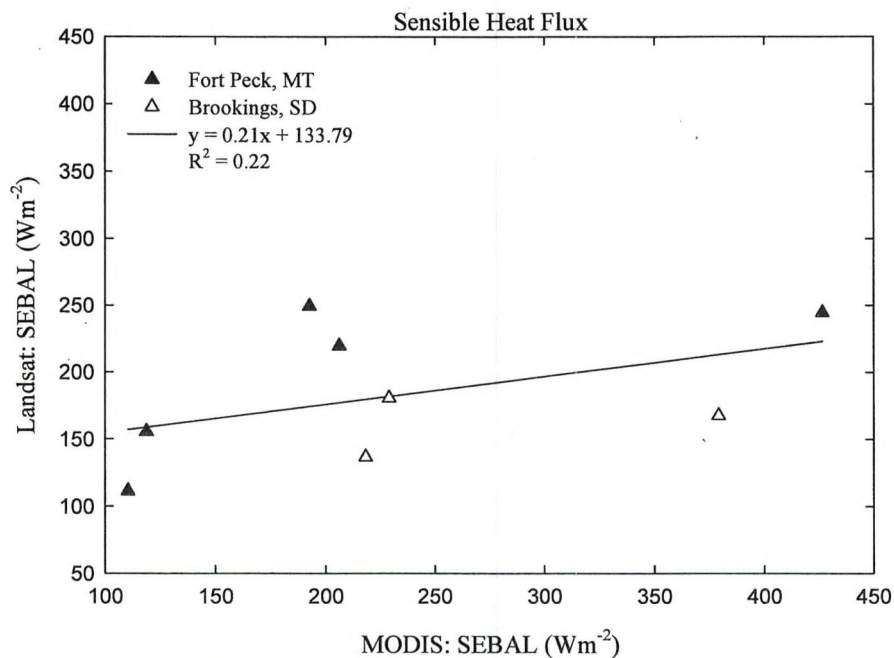


Figure 24. Comparison of H between the estimates by SEBAL using Landsat pixels simulated to a MODIS pixel and a MODIS pixel for Brookings and Fort Peck sites.

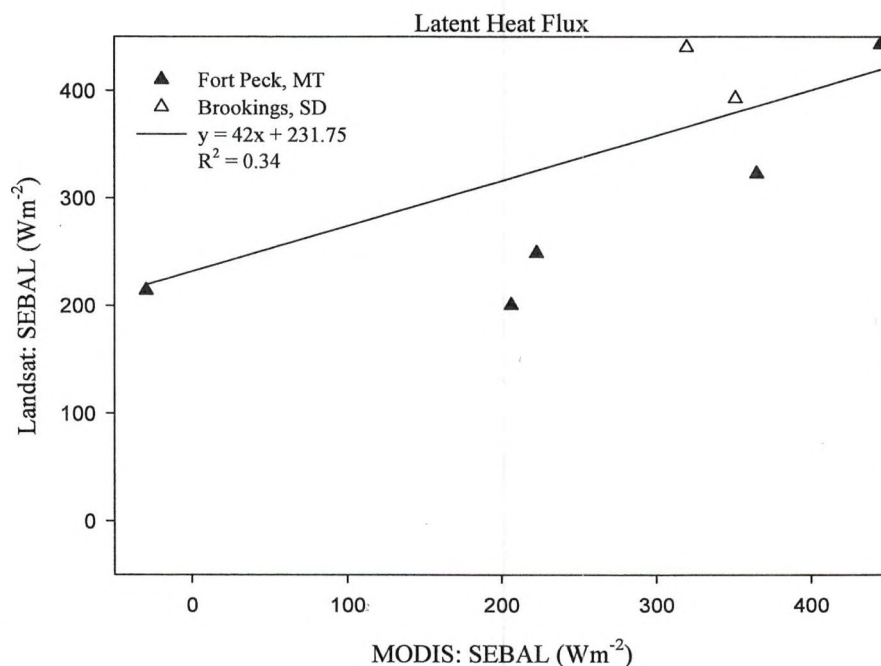


Figure 25. Comparison of λE between the estimates by SEBAL using Landsat pixels simulated to a MODIS pixel and a MODIS pixel for Brookings and Fort Peck sites.

For instance, in a similar study, McCabe and Wood (2006) compared modeled heat fluxes using the SEBS model, and ASTER, ETM+ and MODIS data over Walnut

Creek watershed in Iowa. Respectively, their results showed correlation of 0.65 and 0.59 between a MODIS pixel estimate of ET and that of ASTER and Landsat pixels aggregated to the same window size of a MODIS pixel around flux towers. When Landsat and MODIS estimates of ET were compared at all points across the watershed, the correlation was only 0.071. Pixel-level comparisons of ET between modeled and observed fluxes showed correlations of 0.71 and 0.74 for ASTER and Landsat, respectively. Unlike surface conditions of the flux tower sites in this study, the high correlation between Landsat and MODIS was explained in their paper by the high degree of surface homogeneity (similar agricultural crops) of the catchment where the validation towers were located (McCabe and Wood 2006). Caution should also be taken in interpreting the inter-sensor comparison results through pixel aggregation due to non-linearity of surface variables and parameters across space or what is called the adjacency effect (Liang *et al.* 2002; Brunsell and Gillies 2003).

4.4 Surface Energy Balance Closure

Finally, in literature it was mentioned that absence of energy closure is one of the main problems in comparing modeled and observed heat fluxes (Wever *et al.* 2002; Verstraeten *et al.* 2005). Similarly, in this study the absence of energy closure observed had certain influence on the accuracy of the comparison. Referring to Table 7, the discrepancies range from almost no absence of energy closure up to as high as 185 Wm^{-2} . The negative sign in the table indicates that the sum of the three heat fluxes was more than R_n , and the positive sign indicates the sum was less than R_n .

Table 7. Absence of energy closure observed at flux towers for all the dates and for both sensors.

Date	Site	Absence of Energy Closure (Wm^{-2})	
		Sensor	
		Landsat	MODIS
081702	Fort Peck	33	4
090202	Fort Peck	-9	28
071803	Fort Peck	-	-4
081203	Fort Peck	53	45
080406	Fort Peck	61	45
081106	Fort Peck	64	64
080404	Brookings	9	-
051905	Brookings	-57	-56
080705	Brookings	9	49
062306	Brookings	-9	-97
050907	Brookings	-185	-

It is difficult to know exactly where possible errors would be introduced in the flux tower estimation of heat fluxes, and hence a $\pm 50 \text{ Wm}^{-2}$ difference is usually considered as a typical error associated with such measurements (Nagler *et al.* 2005; Timmermans *et al.* 2007). However, when data points like June 23, 2006 and May 05, 2007 were considered, the discrepancies were higher than the prescribed value and could seriously affects the model-validation work.

4.5 Sensitivity Analysis

Again, the derivation of Z_{om} empirically from NDVI as in the original parameterization of SEBAL is not always applicable for areas with heterogeneous vegetation cover and different growth stages (Timmermans *et al.* 2007). Similarly, no definitive relationship was found between the vegetation height around the Brookings flux tower and NDVI. This approach was not followed as a result, and instead the 2001 USGS Land Cover map was used. Comparatively, the way land is used generally changes over longer periods of time than seasonal changes of land cover. It was therefore more

important to check if any significant change had happened in terms of land use instead of land cover. Multiple assumptions were made when the 2001 USGS National Land Cover map was used in H modeling including:

- 1) The 2001 land cover map was valid;
- 2) Dominant crop/vegetation types chosen were representative of the vegetation actually present; and
- 3) Constant values were assumed regardless of the growth stage of a dominant crop/vegetation type found under each class.

To assess the level of uncertainties involved in these assumptions, sensitivity analyses of H in response to changes in Z_{om} and δT were conducted. The MODIS image acquired on Aug. 17, 2002, covering Landsat path 35 and row 27 was chosen for analysis purposes. The main reason for choosing this particular image date was that a good level of agreement was obtained between the modeled and observed heat fluxes. A sensitivity analysis of the model was performed by perturbing the original Z_{om} values of four hot reference pixels. For each perturbation, an average value of the pixels was taken while iteratively deriving H . Also, the model's performance was tested to changes in δT . Changes were only made to δT values of the hot pixels from the fifth iteration, which was corrected for atmospheric stability conditions. Results in Table 8 show the percentage difference in the modeled H for the prescribed unit and percentage changes of δT and Z_{om} at the hot reference pixels, respectively. Increases in Z_{om} by significant percentages were accompanied by negligible increases in δT . It can be noted that δT at the hot pixels changes when any of the three input parameters of Eq. 6 changes. Perturbation of Z_{om} at the hot pixels resulted in a change of the original r_{ah} values at the

reference pixels and, hence δT . Consequently, when vegetation height at the hot pixels was artificially increased, δT decreased gradually but slightly. The corresponding change in H was more significant when δT was changed slightly than when Z_{om} was changed by significant amount, *i.e.* a 700% change in the original values of Z_{om} at the hot reference pixels was equivalent to a change of 1.4 °C in δT , causing discrepancies in the H estimate by about 23.6 % or 26 Wm⁻². Similarly, a change in δT by about 3 °C caused a discrepancy of 45.5% or 50 Wm⁻² in the H estimate.

Table 8. Results of sensitivity analysis of SEBAL sensible heat flux modeling to input parameters.

Input Parameters					
Surface-to-Air-Temperature Difference			Surface Roughness		
Change in δT °C	δT °C	% Difference in H estimate	% Change in Z_{om}	Z_{om} m	% Difference in H estimate
-3.0	3.624	-45.5	-75	0.016	16
-2.5	4.124	-37.9	-50	0.031	8.2
2.0	4.624	-30.5	-25	0.047	2.7
-1.5	5.124	-22.7	0	0.062	0.0
-1.0	5.624	-15.3	25	0.077	-2.7
-0.6	6.024	-9.1	50	0.092	-4.9
-0.2	6.424	-3.1	75	0.108	-7.3
0.0	6.624	0.0	100	0.123	-8.2
0.2	6.824	2.7	300	0.184	-12.7
0.6	7.224	9.1	400	0.246	-16.8
1.0	7.624	15.5	500	0.308	-19.1
1.5	8.124	22.7	600	0.369	-20.9
2.0	8.624	30.4	700	0.431	-23.6
2.5	9.124	37.7			
3.0	9.624	45.5			

The results of the sensitivity analyses were in good agreement with similar analysis performed by Timmermans *et al.* (2007), where they found deviations of H estimates by -6% and -45% from the original values when the original Z_{om} and δT values of the hot reference pixels were increased and decreased by 25% and 3 °C,

respectively. However, a notable difference in percentage of error for the H estimate was found between their study and this study when δT increased by the same amount. The results indicated that the model SEBAL is extremely insensitive to changes in vegetation characteristics, and hence the assumptions made in the derivation of Z_{om} did not introduce significant uncertainties in H modeling.

CHAPTER V

CONCLUSIONS AND FUTURE WORK

5.1 Conclusions

The model SEBAL was used to estimate heat fluxes using 10 Landsat and nine MODIS images. Flux towers located in Brookings, SD, and Fort Peck, MT, were used to validate modeled results. SEBAL performed better when Landsat data were used rather than MODIS data.

Generally, a coarser spatial resolution pixel like that of MODIS reflects more mixed land cover types and hence hydrological conditions as compared to a higher resolution pixel. Although MODIS has a high signal-to-noise ratio, its inability to distinguish sub-pixel land surface elements causes significant error in average latent heat estimates when sub-pixel variability of moisture and vegetation conditions was high. It has been indicated that spatial resolution of less than 250 m for the thermal band of MODIS and less than 500 m for most remote sensing input parameters to surface energy balance models would have provided better spatial details required for parameterization of heat fluxes (Kustas *et al.* 2004). This is particularly true for most land cover types under agricultural areas in the Midwest U.S., where typical plot size is on the order of one hectare (Kustas *et al.* 2004). Nevertheless, when an average ET value of a larger homogenous area is considered, flux estimation error would be minimal. This is because average values of remote sensing input parameters could be used in SEBAL modeling.

Modeling of heat fluxes at a significantly smaller fetch size made the comparison of the results with other similar studies that were conducted at a larger fetch more difficult. In addition, no study to date has used the relevant MODIS data as an input to SEBAL for heat flux modeling; hence it was difficult to make a direct one-to-one comparison with other work because of differences in modeling framework and settings. It was also noticed that most work involving surface energy balance models in literature did not have a consistent way of defining footprint area, and footprint area approximation by itself is currently an ongoing research topic. Absence of energy closure in eddy-covariance measurements was also another source of uncertainty. This phenomenon was observed for almost all of the dates considered in this study.

Moreover, the use of SEBAL has been limited to a relatively flat topography, as the effects of complex terrain on heat flux modeling are still a challenge (Allen *et al.* 2000). This could be of some concern when the intended application of SEBAL is for irrigated rough terrain where mountain populations continue to depend on natural resources and agriculture for their livelihood.

Most surface energy balance models including SEBAL suffer from contradictions of being simple in their implementation, with minimum required ground data, while they are needed at the same time to be accurate in the modeling of heat fluxes. Although many models have been acknowledged in literature as models producing reasonable estimates of heat and vapor fluxes, discrepancies still exist when considering the whole modeling domain of heat and vapor fluxes at regional scales. Generally, it can be concluded that the procedure in SEBAL modeling is not complicated; however it is highly subjective. The

same image processed by two different people using the same input parameters could yield different results, as the work involves personal judgment.

5.2 Future Work

For a similar research project, some important factors could be considered in the future to improve the accuracy of both the modeling and validation work. Large homogenous areas, at least equivalent in size to a number of aggregated MODIS pixels would be ideal sites for doing similar comparison work. This will avoid spatial heterogeneity that cannot be captured by a single MODIS pixel. The use of more validation sites located not only in the same type of land cover but across different ecosystems is important. The fact that 90% of the approximate footprint area is smaller than a single MODIS pixel and larger than a few Landsat pixels makes it difficult to apply footprint analysis models when remotely-sensed data with coarse spatial resolution are used. In this case, the use of data with higher spatial resolution than the spatial resolutions of both sensors considered will yield a better result. Footprint area discrepancies for the validation of MODIS modeling results can also be solved using scintillometer measurements of heat fluxes across a one-to-five kilometers profile. Real-time data collected from the field during the overpass time of the sensors would also provide more confidence in controlling the various input parameters used in SEBAL. In this regard, extensive field data collection during satellite overpass time for use in calibrating the various empirical equations of the model is important. This includes spectra measurement of soil and vegetation from representative areas and from vegetation of different growth stages. Also, ground validation of hot and cold reference pixels is needed to confirm that the SEBAL assumptions for the pixels are valid; and this would

improve the empirical and semi-empirical modeling approaches pursued by the model. In addition, estimates of one-way atmospheric transmittance and atmospheric emissivity could be improved by modeling the optical properties of the atmosphere during overpass time of the satellites.

Even though SEBAL is not sensitive to variation in Z_{om} , the use of a detailed and up-to-date land cover map for the derivation of surface roughness information and for validating the spatially varying conditions of land surface elements is important. This will decrease the number of uncertainties that would be involved in the modeling work. Extensive sensitivity analyses were already done in literature on inputs of SEBAL; however, it is always important to check on the model's sensitivity for various assumptions made on an individual research work basis. Combining high spatial, high temporal and multi-spectral resolution remote sensing data in order to amend the limitations of the ongoing operational satellites for continuous and reliable estimates of heat fluxes modeling should also be the focus of future research. For instance, ASTER, as the only sensor providing multi-spectral thermal IR data, can be utilized along with sensors having a single thermal IR band but high temporal resolution like AVHRR or MODIS. Landsat, mentioned earlier with its poor temporal resolution but high spatial resolution in both visible and thermal IR bands, can be considered in an effort to combine multi-sensor data for better parameterization of heat fluxes. Research focusing on combining the different available sources of remote sensing data over controlled surface and field conditions under different landscapes and ecosystems should also be encouraged in the future.

APPENDICES

APPENDIX A

LIST OF SYMBOLS

C_1 and C_2	local constants of vegetation type	-
Cp_{air}	specific heat capacity of air	$Jkg^{-1} \text{ } ^\circ K^{-1}$,
DN	(digital number) quantized calibrated pixel value	-
D and P	similarity constants of atmospheric stability	-
f	footprint	m^{-1}
g	acceleration due to gravity	ms^{-2}
G_0	soil heat flux	Wm^{-2}
$G_{0(cold)}$	soil heat flux at the cold pixel	Wm^{-2}
$G_{0(hot)}$	soil heat flux at the hot pixel	Wm^{-2}
G_{SC}	solar constant	Wm^{-2}
h	average vegetation height	m
H	sensible heat flux	Wm^{-2}
$H_{(cold)}$	sensible heat flux at the cold pixel	Wm^{-2}
$H_{(hot)}$	sensible heat flux at the hot pixel	Wm^{-2}
k_1 and k_2	Landsat calibration constants	$Wcm^{-2}sr^{-1}\mu m^{-1}$
L	spectral radiance	$Wm^{-2}sr\mu m$
L	Monin-Obukhov length	m
MAD	mean absolute difference	Wm^{-2}
MAPD	mean absolute percentage difference	%
n	total number of observations	-
NDVI	normalized difference vegetation index	-
r_{ah}	bulk aerodynamic resistance to heat transfer across a single surface-atmosphere layer determined according to the Monin-Obukhov stability function	sm^{-1}
$r_{ah(hot)}$	bulk aerodynamic resistance to heat transfer of hot pixel	sm^{-1}
$R_{(cold)}$	net radiation at the cold pixel	Wm^{-2}
$R_{(hot)}$	net radiation at the hot pixel	Wm^{-2}
$R_{L\downarrow}$	clear-sky incoming longwave radiation	Wm^{-2}
$R_{L\uparrow}$	outgoing longwave radiation	Wm^{-2}
RMSD	root mean square difference	Wm^{-2}
R_n	net radiation	Wm^{-2}
$R_{S\downarrow}$	clear-sky incoming direct and diffused shortwave radiation	Wm^{-2}
s	slope in radiance	-

\bar{S}	mean of SEBAL modeled heat flux	Wm ⁻²
S_i	SEBAL modeled heat flux of a particular date	Wm ⁻²
\bar{T}	mean of tower observed heat flux	Wm ⁻²
T_0	radiometric surface temperature	° K
T_a	reference air temperature	° K
$T_{air(Z)}$	potential skin level air temperature at reference height, Z , above canopy	° K
T_i	tower observed heat flux of a particular date	Wm ⁻²
$T_{0(cold)}$	radiometric surface temperature of cold pixel	° K
$T_{0(DEM)}$	DEM-adjusted radiometric surface temperature	° K
$T_{0(hot)}$	radiometric surface temperature of hot pixel	° K
T_S	land surface temperature	° K
T_{zoh}	aerodynamic surface temperature	° K
u_*	local friction velocity at wind speed measurement height	ms ⁻¹
u_*	first guess of spatially distributed friction velocity	ms ⁻¹
u_x	horizontal wind speed measurement at reference height x	ms ⁻¹
x	peak location of the footprint	m
Z_0	zero plane of displacement	m
Z_1 and Z_2	reference heights defining the boundary layer for heat transfer	m
Z_1 and Z_2	reference heights above the ground surface	m
Z_m	flux tower (observation) height	m
Z_{oh}	surface roughness length for heat transport	m
Z_{om}	surface roughness length for momentum transport	m
Z_x	height at which wind speed is measured	m
Z_u	combined length scale of Z_m and Z_0	m
δZ	elevation difference	m
α	planetary broadband surface albedo	-
$\alpha_{1,2,3,...}$	surface reflectance measured by the sensors in the respective bands (channels)	-
β	Bowen ratio	-
γ	surface azimuth angle	-
δ	declination of the earth	-
δT	surface-air temperature difference at reference height Z above the canopy	° K
δT_{cold}	surface-to-air temperature difference of cold reference pixels	° K
δT_{hot}	surface-to-air temperature difference of hot reference pixels	° K

$\frac{\delta T}{\delta Z}$	temperature difference between the soil surface and reference depth	$^{\circ} \text{Km}^{-1}$
ε_a	clear-sky emissivity of the atmosphere	-
ε_s	surface thermal IR emissivity	-
θ	solar incident angle	-
k	von Karman constant	-
λE	latent heat flux	Wm^{-2}
λ_s	thermal conductivity of the soil	Wm^{-2}
Λ	evaporative fraction	-
$\rho_{air(hot)}$	air density of hot pixel	kgm^{-3}
ρ_{air}	air density as a function of air temperature and atmospheric pressure	kgm^{-3}
σ	Stefan-Boltzman constant	$\text{Wm}^{-2} \text{ } ^{\circ} \text{K}^{-4}$
σ_s	standard deviation of SEBAL modeled heat flux	Wm^{-2}
σ_T	standard deviation of tower observed heat flux	Wm^{-2}
τ	momentum flux	Nm^{-2}
τ'	one-way atmospheric transmittance	-
ϕ	latitude of the site	-
ψ_h	stability correction for heat transport	-
ψ_m	stability correction for momentum transport	-
ω	hour angle	-

APPENDIX B

ATTRIBUTES OF LANDSAT TM AND ETM+

Table 9. Attributes of Landsat TM for Brookings, SD, flux tower site (USGS 2006).

Sensor	Acq. Date	Julian Date	Path	Raw	Cloud Cover	Sun Elevation	Sun Azimuth	Scene Time	
								Starting	Ending
TM	080404	217	29	29	20%	55.517768	135.274943	16:53:54	16:54:21
TM	051905	139	29	29	0%	59.710405	137.857919	16:58:28	16:58:55
TM	080705	219	29	29	0%	55.540973	137.984891	16:59:09	16:59:35
TM	062306	174	29	29	0%	62.654070	133.812250	17:03:52	17:04:19
TM	050907	129	29	29	0%	58.334862	143.137951	17:05:43	17:06:10

Table 10. Attributes of Landsat TM and ETM+ for Fort Peck, MT, flux tower site (USGS 2006).

Sensor	Acq. Date	Julian Date	Path	Raw	Cloud Cover	Sun Elevation	Sun Azimuth	Scene Time	
								Starting	Ending
ETM+	052902	149	35	27	1%	59.513584	140.709747	17:36:03	17:36:30
ETM+	081702	229	35	27	0%	51.243805	144.404526	17:35:36	17:36:03
ETM+	090202	245	35	27	0%	46.525845	149.044861	17:35:26	17:35:53
TM	070203	183	36	26	0%	57.756614	134.464812	17:29:25	17:29:52
TM	071803	199	36	26	0%	57.780477	135.607155	17:29:41	17:30:08
TM	081203	224	35	26	0%	50.567312	140.828055	17:23:57	17:24:23
TM	080406	216	35	26	0%	54.096329	144.853154	17:40:21	17:40:47
TM	081106	223	36	26	0%	52.361816	146.514384	17:46:36	17:47:03

APPENDIX C

C1. LANDSAT RADIOMETRIC, SATELLITE AND IMAGE CHARACTERISTICS DESCRIPTIONS

Table 11. Descriptions of Landsat 5 TM (USGS 2006).

TM Bands	1	2	3	4	5	6 (Thermal)	7
Bandwidth (nm)	450- 520	520- 600	630- 690	760- 900	1550- 1750	10400- 12500	2080- 2350
Spatial Resolution	30	30	30	30	30	120	30
Quantization	8-bit unsigned integer (256 levels)						
Swath Width	185 km						
Repeat coverage cycle	16 days (233 orbits)						
Altitude	705 km						
Inclination	Sun-synchronous, 98.2 degrees						
Equatorial crossing	Descending node: 10:10 am						
Launch date	March 1984						

Table 12. Descriptions of Landsat 7 ETM+ (USGS 2006).

ETM+ Bands	1	2	3	4	5	6 (Thermal)	7	Pan
Bandwidth (nm)	450- 515	525- 605	630- 690	750- 900	1550- 1750	10400- 12500	2090- 2350	520- 900
Spatial Resolution	30	30	30	30	30	60	30	15
Quantization	Best 8 of 9 bits							
Swath Width	185 km							
Repeat coverage cycle	16 days (233 orbits)							
Altitude	705 km							
Inclination	Sun-synchronous, 98.2 degrees							
Equatorial crossing	Descending node; 10:00 am							
Launch date	April 1999							

C 2. RADIOMETRIC AND IMAGE CHARACTERISTICS DESCRIPTIONS OF MODIS PRODUCTS

Table 13. Descriptions of MOD011A1 products (USGS 2006).

MODIS Channel	Bandwidth (nm)	Spatial Resolution	Quantization
31 emissivity	10.780 - 11.280	1 km	8-bit unsigned integer
32 emissivity	11.770 - 12.270	1 km	8-bit unsigned integer
Daily daytime LST	-	1 km	16-bit unsigned integer

Table 14. Descriptions of MOD09GHK products (USGS 2006).

MODIS Channel	Bandwidth (nm)	Spatial Resolution	Quantization
1	620-670	250 m	16-bit signed integer
2	841-876	250 m	16-bit signed integer
3	459-479	500 m	16-bit signed integer
4	545-565	500 m	16-bit signed integer
5	1230-1250	500 m	16-bit signed integer
7	2105-2155	500 m	16-bit signed integer

APPENDIX D

SEBAL PARAMETERS

Table 15. SEBAL parameters for the cold and hot reference pixels selected.

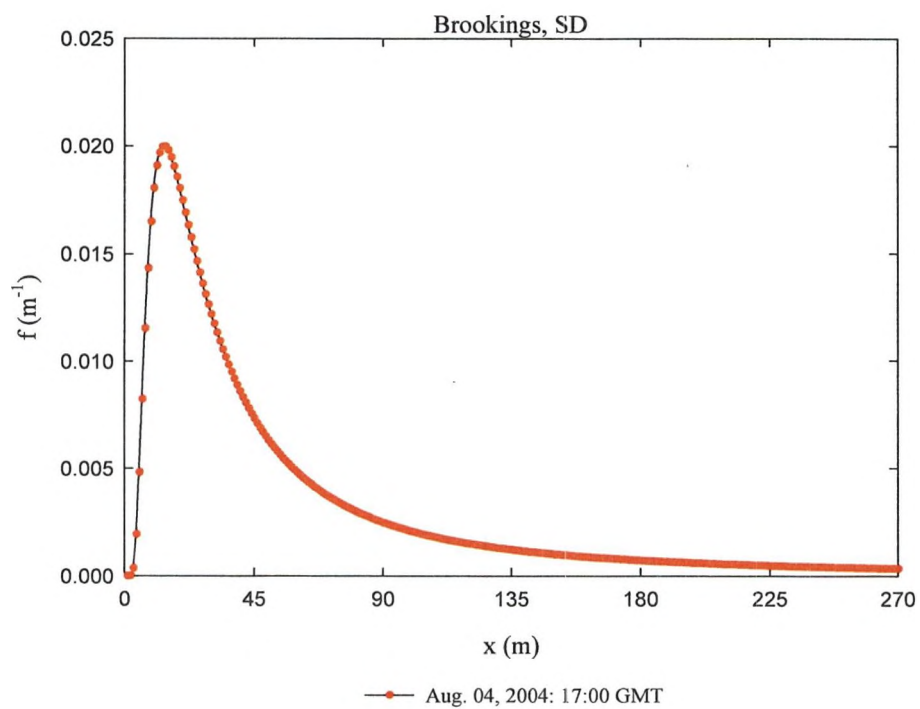
Scene ID_Date	Sensor	Pixel	R_n	G_0	T_0	δT	u_*	Z_{om}	r_{ah}	H	λE	NDVI	ε_s	τ'
3527_081702	ETM+	Cold	533.2	11.60	283.2	0.00	0.56	0.12		0.000	521.2	0.92	0.929	1.00
		Hot	453.7	113.2	316.8	6.10	0.70	0.10	18.5	340.5	0.000	0.09	0.901	0.76
	MODIS	Cold	659.1	39.60	289.6	0.00	0.37	0.00		0.000	619.1	0.52	0.988	0.76
		Hot	481.2	98.60	313.1	6.60	0.70	0.06	18.3	382.7	0.000	0.17	0.988	0.76
3527_090202	ETM+	Cold	573.2	31.20	284.7	0.00	0.00	0.00		0.000	542.0	0.73	0.994	0.76
		Hot	455.5	108.5	315.3	5.90	0.72	0.05	17.9	347.0	0.000	0.12	0.910	0.76
	MODIS	Cold	575.3	27.60	293.1	0.00	0.40	0.00		0.000	548.5	0.84	0.988	0.76
		Hot	413.2	89.20	313.3	5.10	0.80	0.12	16.4	324.0	0.000	0.17	0.981	0.76
3626_071803	MODIS	Cold	646.1	61.30	302.2	0.00	0.20	0.12		0.000	584.7	0.78	0.987	0.76
		Hot	506.8	134.9	324.7	13.2	0.31	0.12	36.3	371.9	0.000	0.38	0.987	0.76
3526_081203	TM	Cold	638.1	53.60	293.5	0.00	0.31	0.08		0.000	584.6	0.67	0.991	0.76
		Hot	501.0	125.8	322.2	10.0	0.43	0.06	27.6	375.1	0.000	0.18	0.930	0.76
	MODIS	Cold	613.3	77.50	301.3	0.00	0.27	0.08		0.000	535.6	0.57	0.975	0.76
		Hot	783.7	188.5	318.5	15.2	0.41	0.06	28.1	595.2	0.000	0.26	0.988	0.76
3526_080406	TM	Cold	670.9	45.10	292.4	0.00	0.15	0.00		0.000	619.3	0.73	0.994	0.76
		Hot	586.3	144.8	329.3	14.6	0.33	0.06	34.0	441.5	0.000	0.11	0.907	0.76
	MODIS	Cold	561.2	72.00	296.8	0.00	0.24	0.12		0.000	495.3	0.39	0.985	0.76
		Hot	463.4	114.3	320.0	11.3	0.34	0.06	33.8	349.1	0.000	0.25	0.985	0.76

Table 15 continued

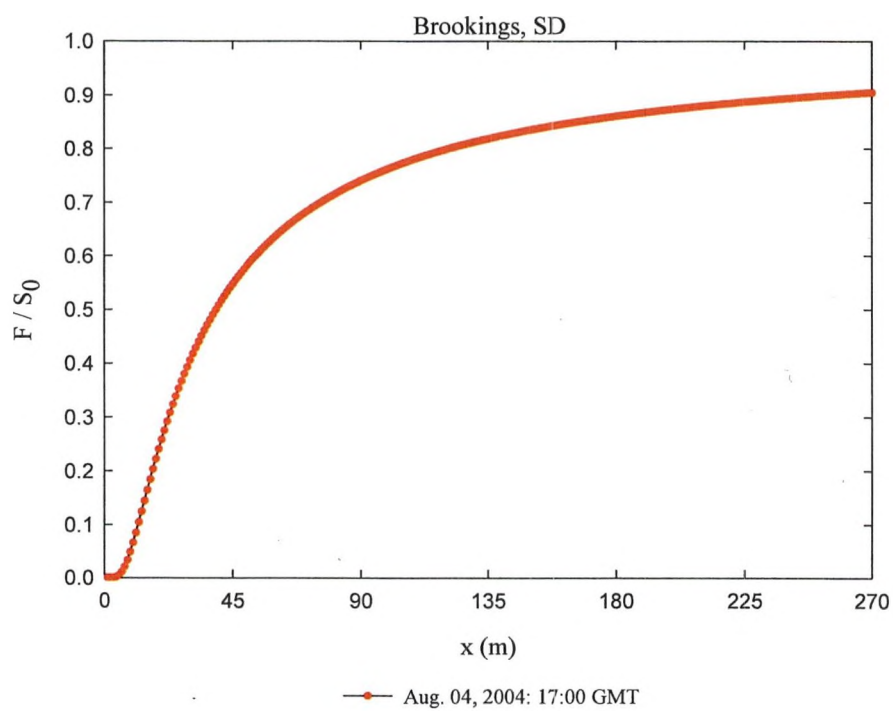
Scene ID_Date	Sensor	Pixel	R_n	G_0	T_0	δT	u_*	Z_{om}	r_{ah}	H	λE	NDVI	ε_s	τ'
3626_081106	TM	Cold	672.3	51.50	293.3	0.00	0.70	0.12		0.000	622.1	0.65	0.989	0.76
		Hot	491.1	122.3	326.9	6.40	0.74	0.04	17.5	368.8	0.000	0.12	0.910	0.76
	MODIS	Cold	580.4	97.80	304.6	0.00	0.74	0.12		0.000	482.5	0.32	0.988	0.76
		Hot	495.3	117.4	316.5	5.50	0.87	0.10	15.0	377.9	0.000	0.24	0.987	0.76
2929_080404	TM	Cold	534.7	47.80	288.6	0.00	0.39	0.12		0.000	486.9	0.25	0.987	0.75
		Hot	732.3	123.9	315.0	11.7	0.56	0.12	21.5	608.4	0.000	0.06	0.900	0.75
2929_051905	TM	Cold	687.8	34.70	290.1	0.00	0.40	0.27		0.000	653.6	0.80	0.997	0.75
		Hot	648.2	134.2	315.4	9.10	0.65	0.12	19.4	514.0	0.000	0.07	0.900	0.75
	MODIS	Cold	748.8	59.60	291.3	0.00	0.44	0.06		0.000	688.5	0.49	0.980	0.76
		Hot	606.4	96.80	304.6	8.30	0.71	0.12	18.0	509.6	0.000	0.34	0.988	0.76
2929_080705	TM	Cold	706.9	24.10	295.2	0.00	0.33	0.05		0.000	725.1	0.90	1.000	0.75
		Hot	621.3	144.5	323.4	9.30	0.59	0.12	20.7	476.8	0.000	0.13	0.913	0.76
	MODIS	Cold	619.1	43.10	298.4	0.00	0.38	0.12		0.000	568.3	0.86	0.980	0.76
		Hot	561.5	104.2	311.3	13.1	0.32	0.00	33.6	457.3	0.000	0.56	0.897	0.83
2929_062306	TM	Cold	727.0	30.80	292.8	0.00	0.15	0.12		0.000	697.1	0.86	1.000	0.76
		Hot	637.3	143.7	322.5	21.8	0.24	0.12	46.7	493.6	0.000	0.26	0.947	0.76
	MODIS	Cold	689.8	42.20	292.5	0.00	0.19	0.06		0.000	618.4	0.80	0.982	0.76
		Hot	627.2	102.8	308.3	14.8	0.31	0.12	31.8	524.4	0.000	0.53	0.987	0.76
2929_050907	TM	Cold	738.6	35.40	291.5	0.00	0.14	0.05		0.000	702.5	0.79	0.990	0.75
		Hot	590.6	129.6	321.0	18.6	0.24	0.05	43.2	461.0	0.000	0.35	0.960	0.76

APPENDIX E

RESULT OF FOOTPRINT ANALYSIS

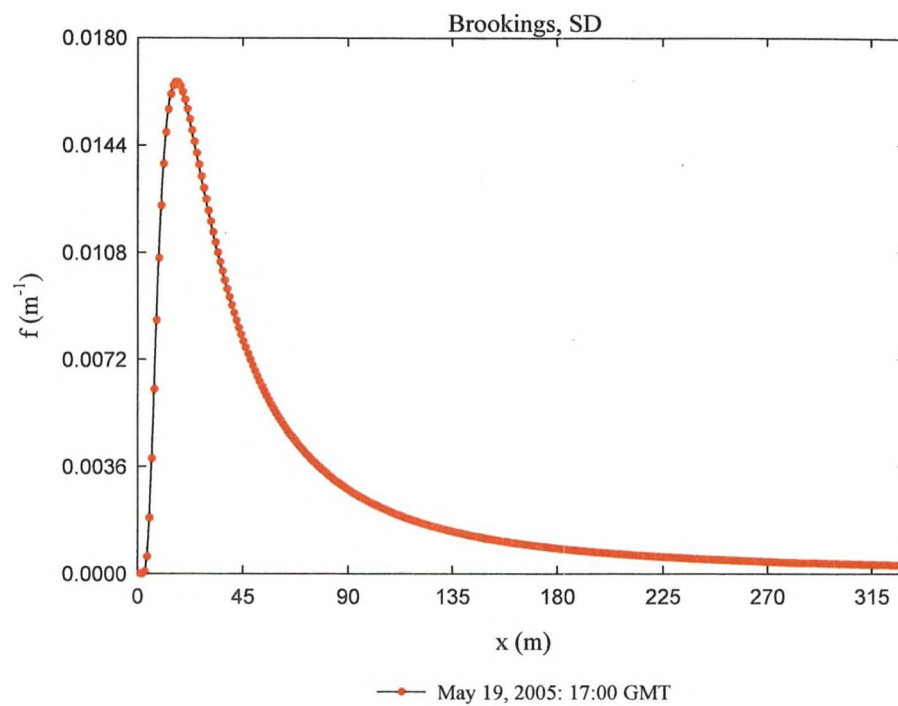


a)

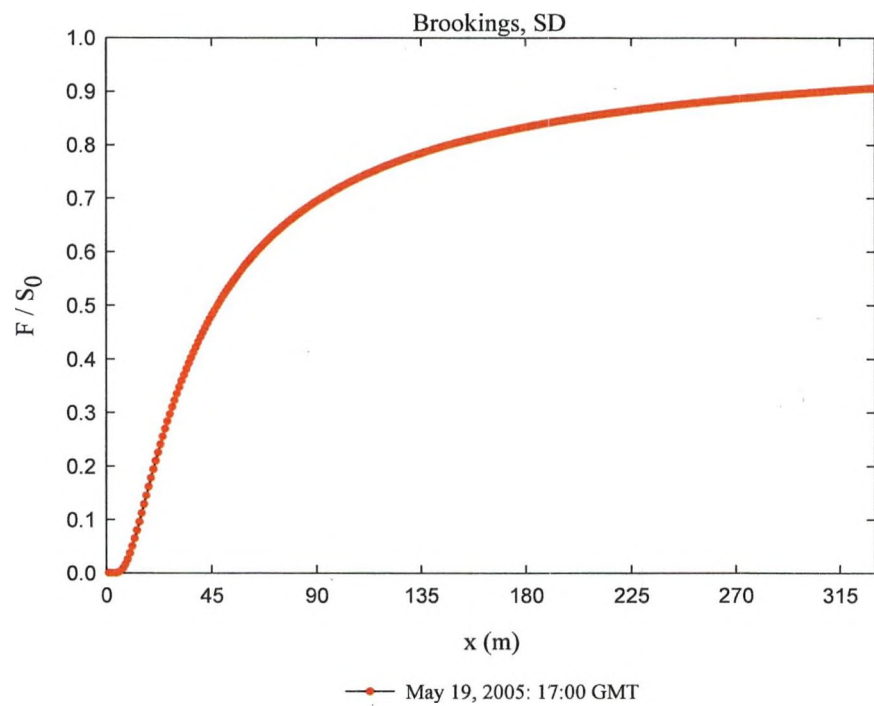


b)

Figure 26 a) footprint and b) cumulative flux as a function of fetch for Landsat TM 080404 overpass date.

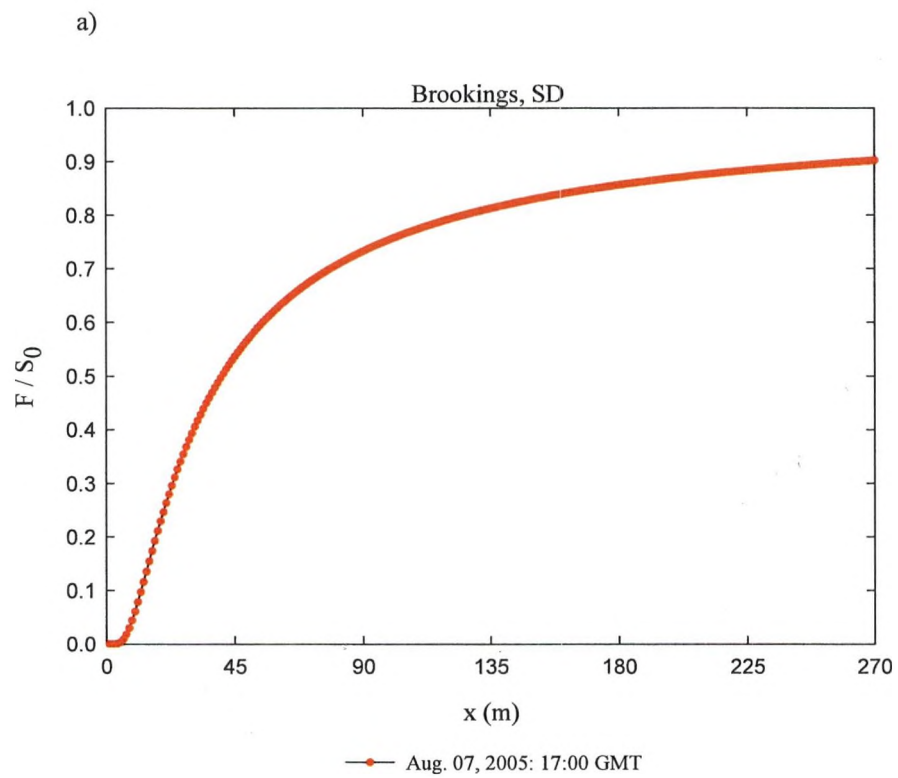
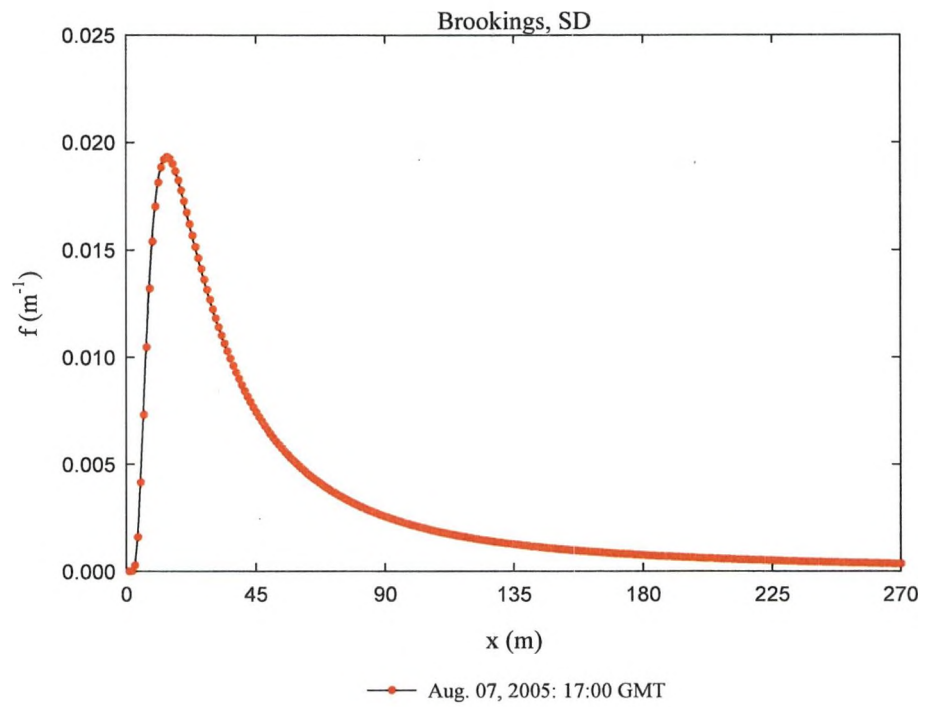


a)



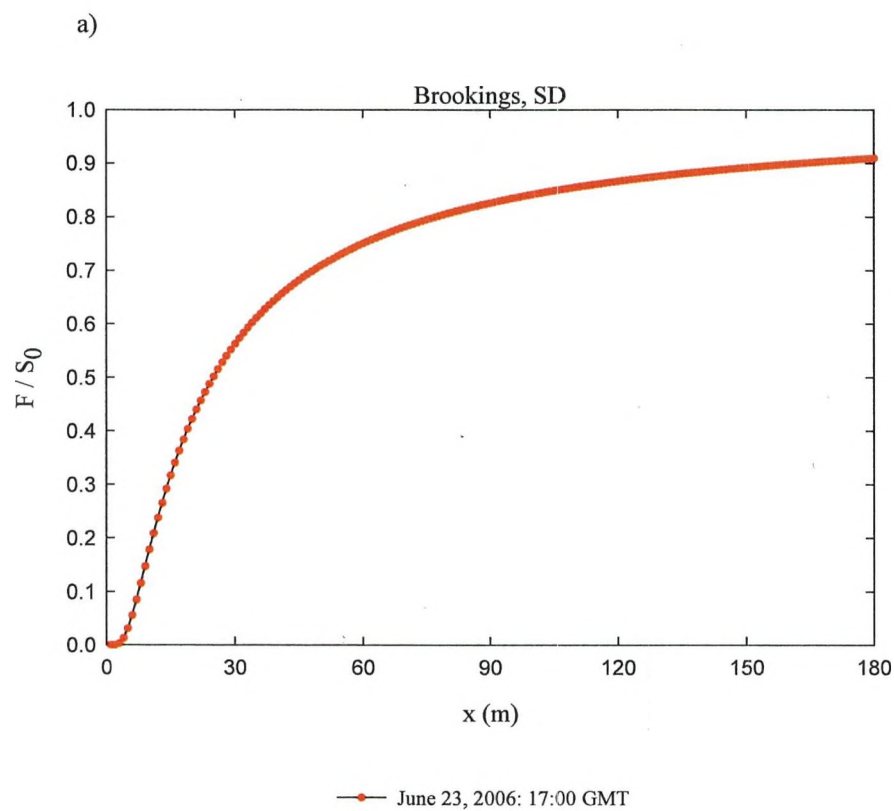
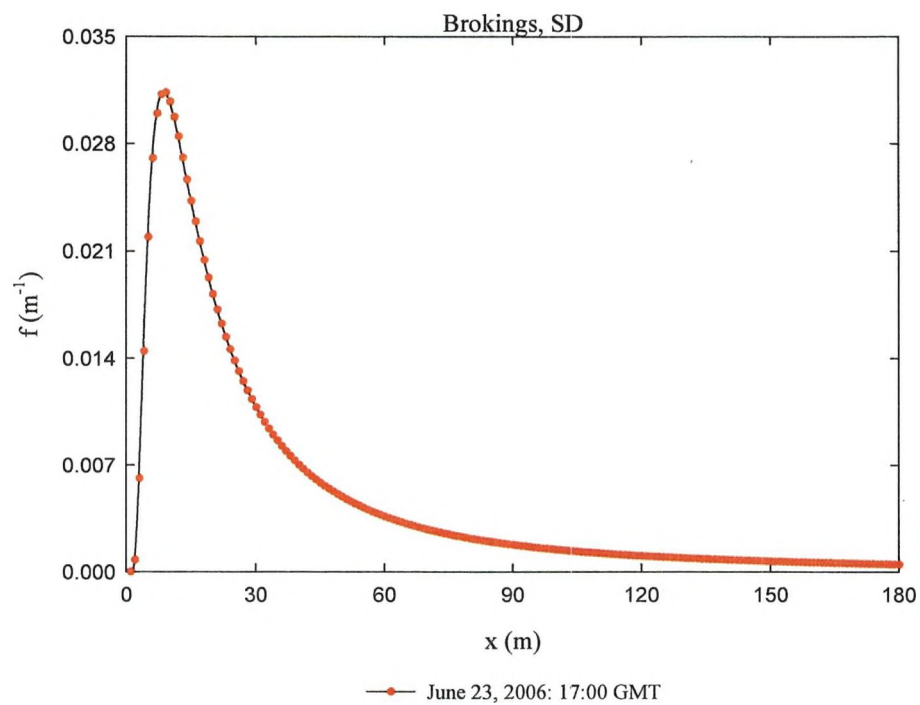
b)

Figure 27 a) footprint and b) cumulative flux as a function of fetch for Landsat TM 051905 overpass date.



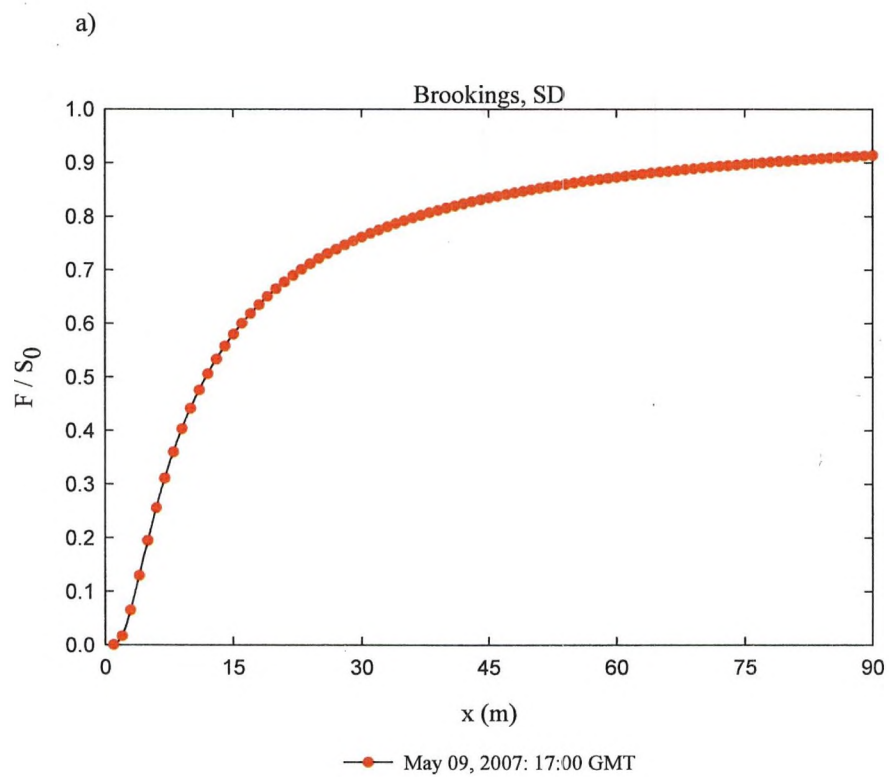
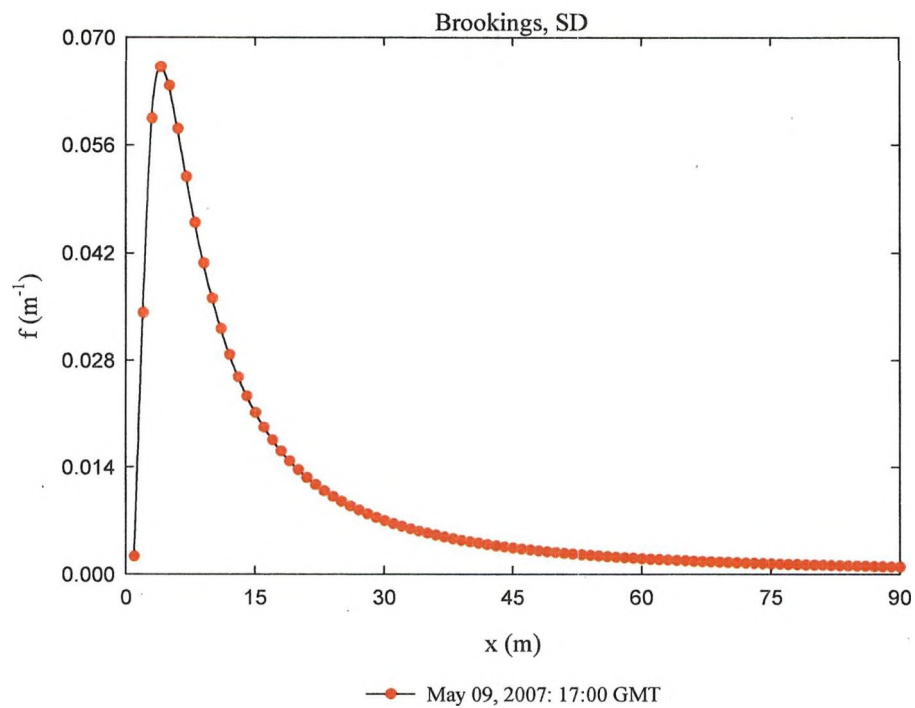
b)

Figure 28 a) footprint and b) cumulative flux as a function of fetch for Landsat TM 080705 overpass date.



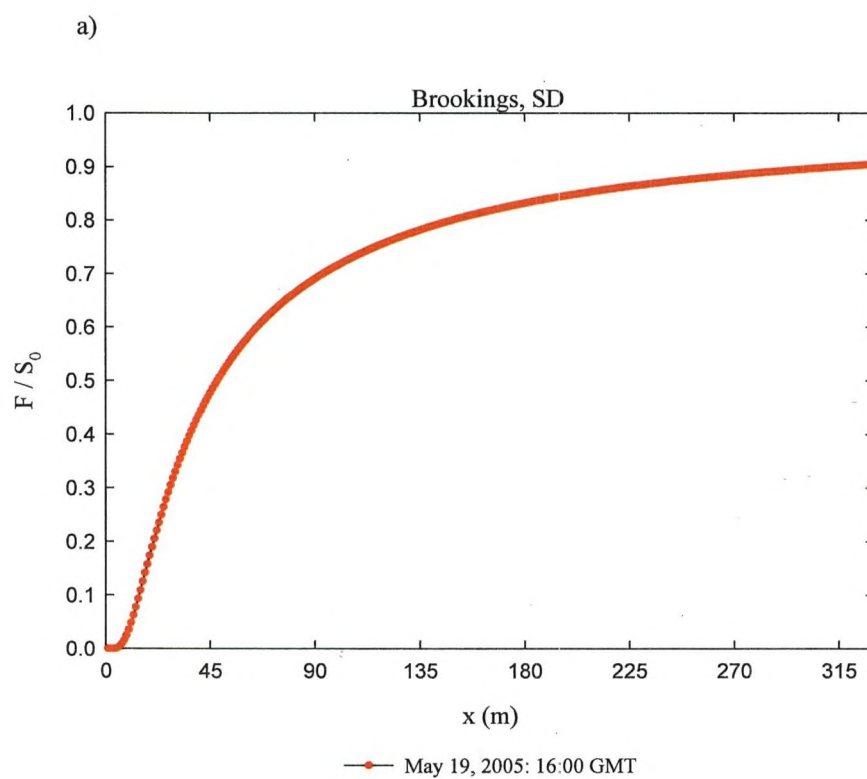
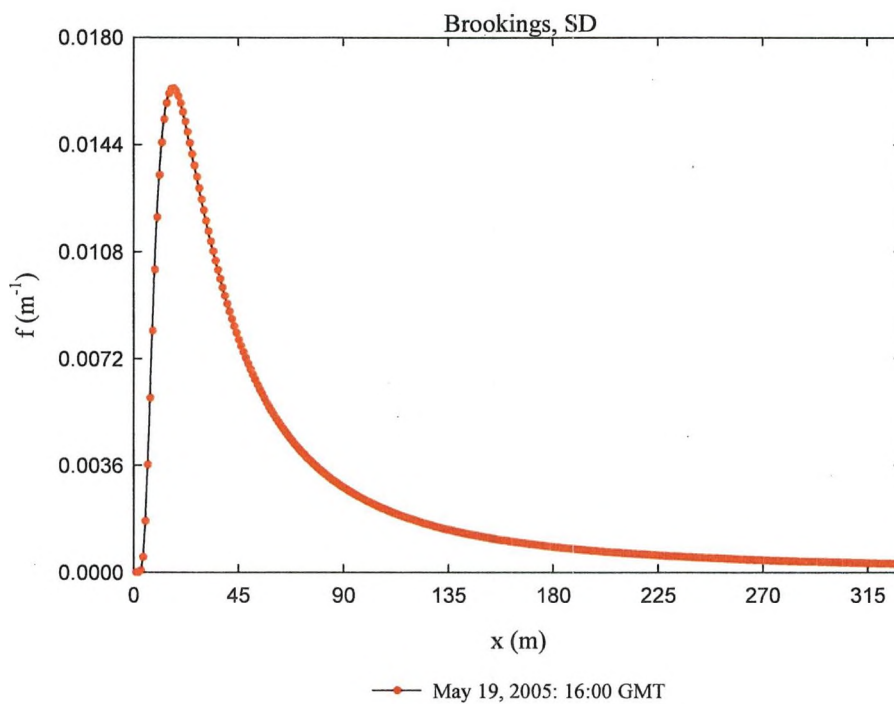
b)

Figure 29 a) footprint and b) cumulative flux as a function of fetch for Landsat TM 062306 overpass date.



b)

Figure 30 a) footprint and b) cumulative flux as a function of fetch for Landsat TM 050907 overpass date.



b)

Figure 31 a) footprint and b) cumulative flux as a function of fetch for MODIS 051905 overpass date.

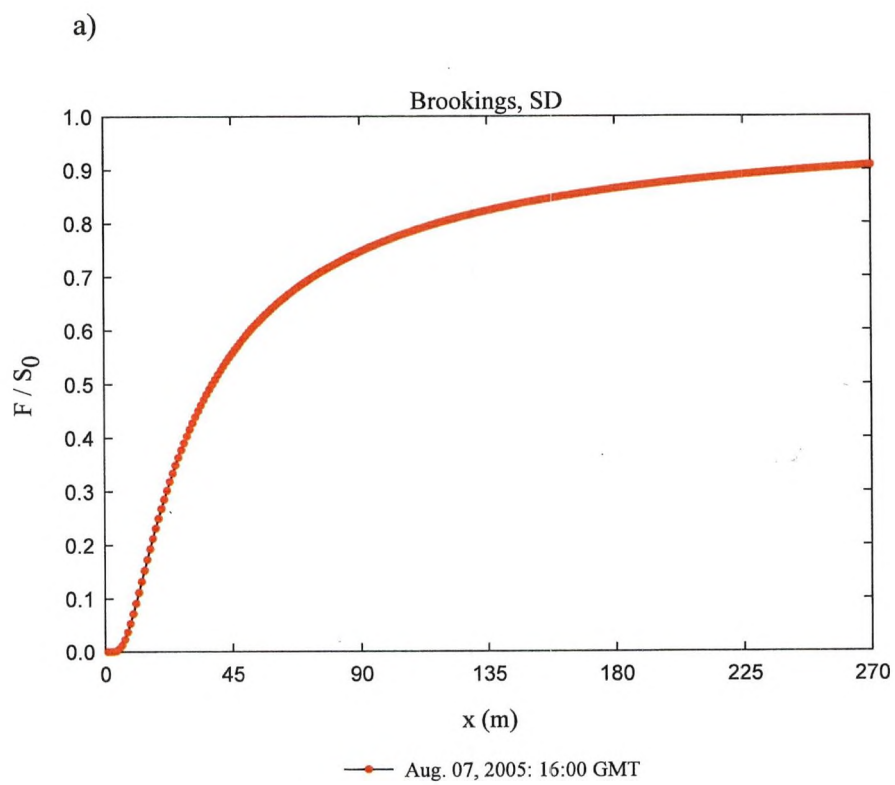
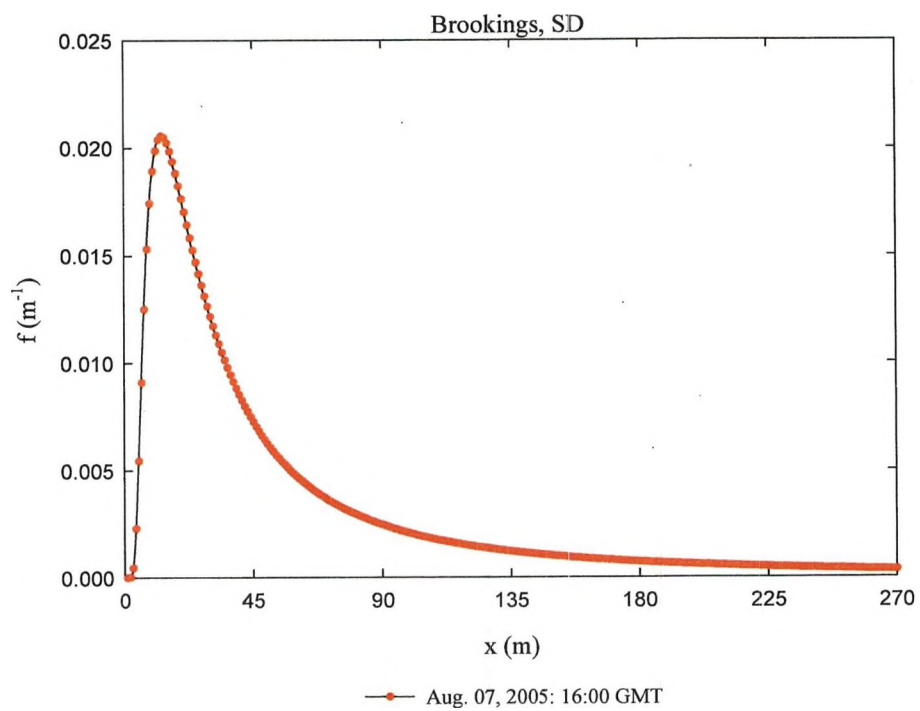
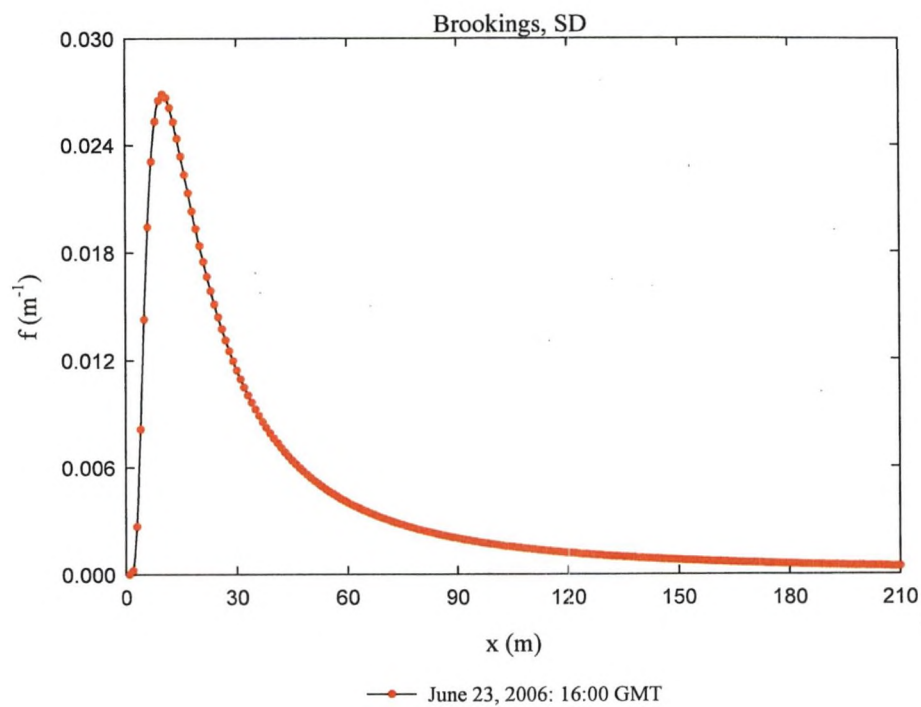
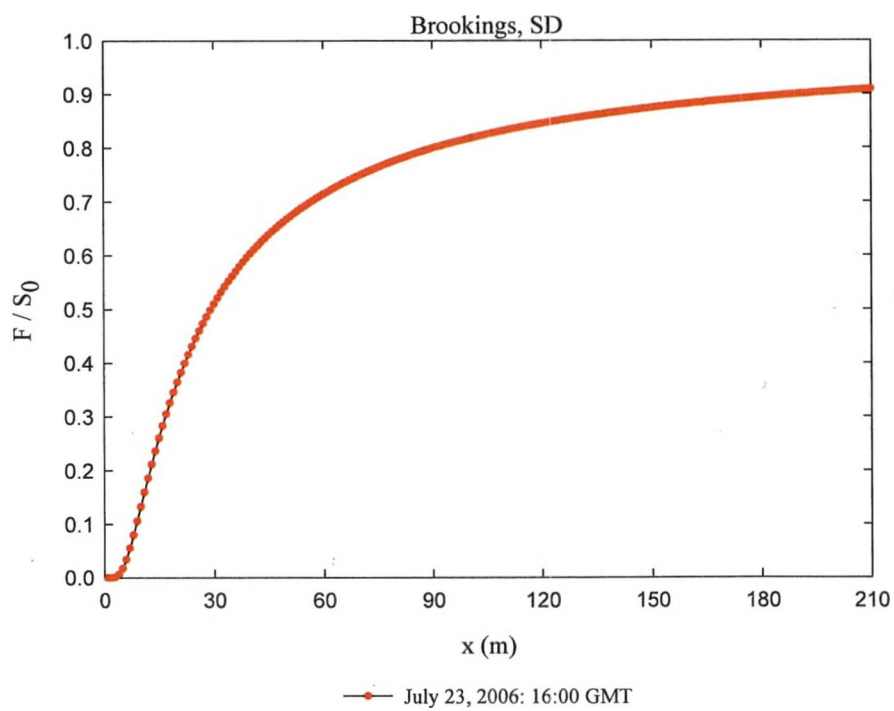


Figure 32 a) footprint and b) cumulative flux as a function of fetch for MODIS 080705 overpass date.



a)



b)

Figure 33 a) footprint and b) cumulative flux as a function of fetch for MODIS 072306 overpass date.

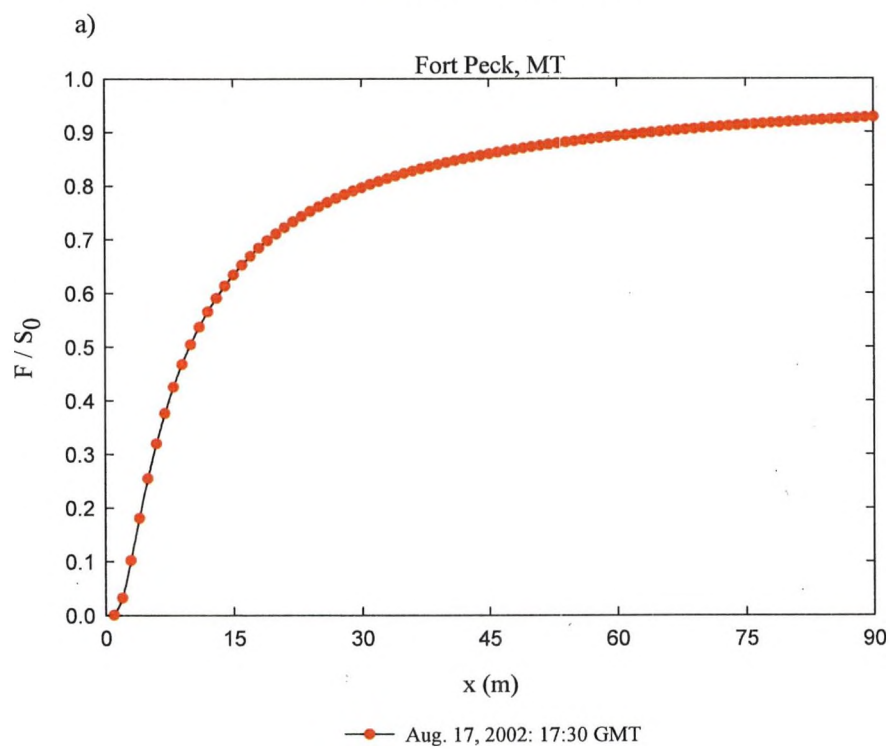
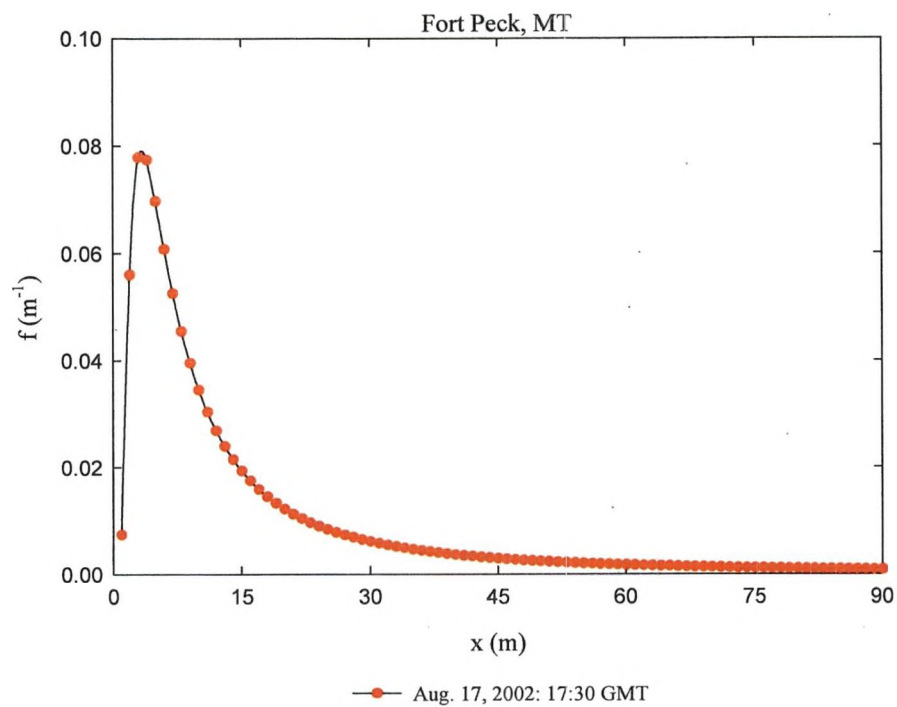


Figure 34 a) footprint and b) cumulative flux as a function of fetch for Landsat ETM+ 081702 overpass date.

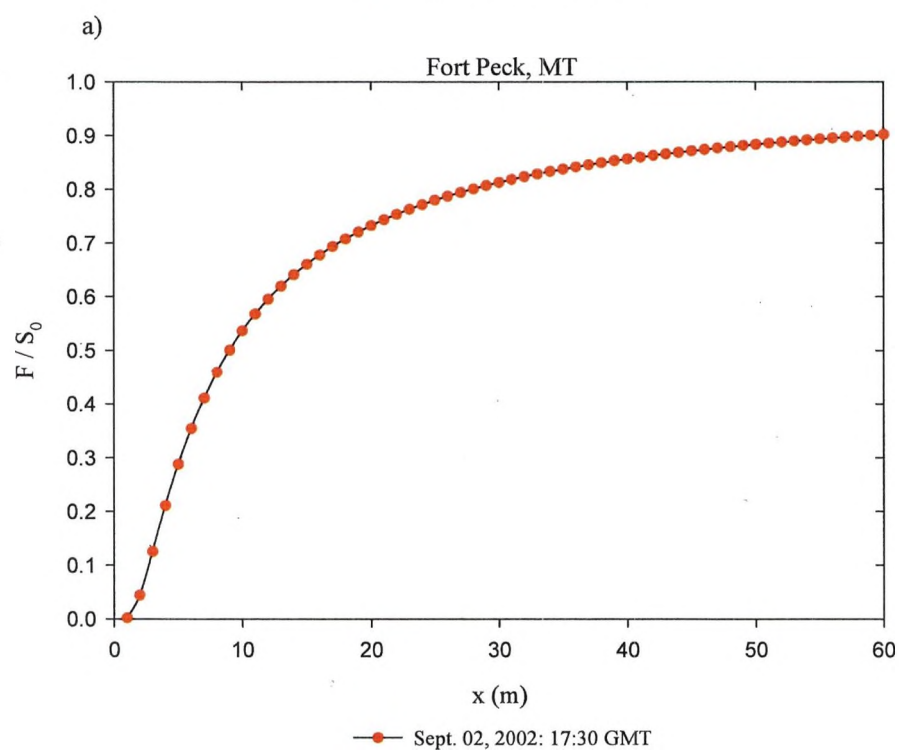
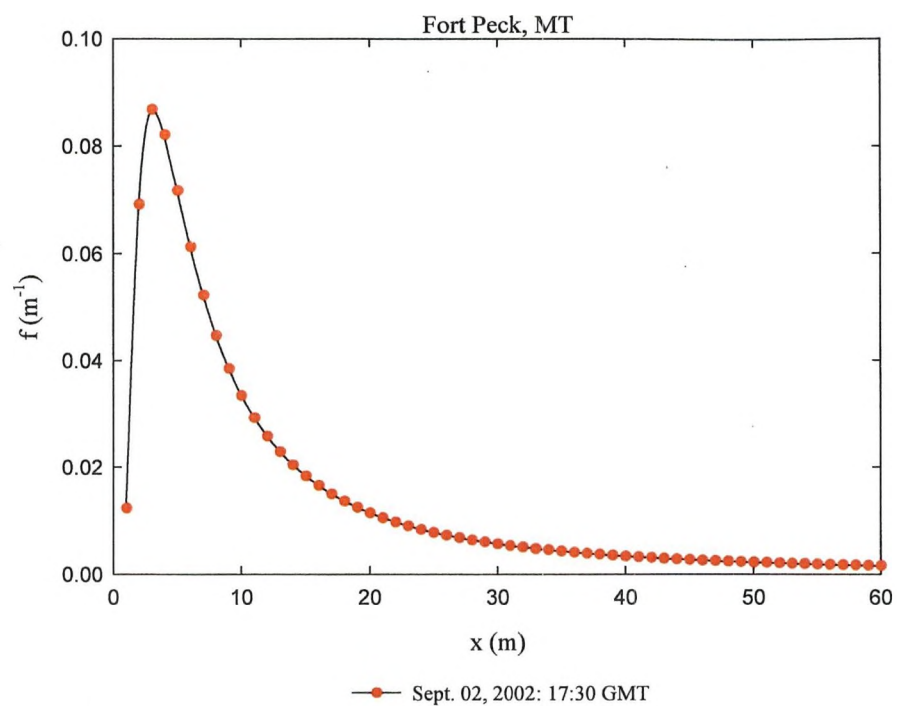


Figure 35 a) footprint and b) cumulative flux as a function of fetch for Landsat ETM+ 090202 overpass date.

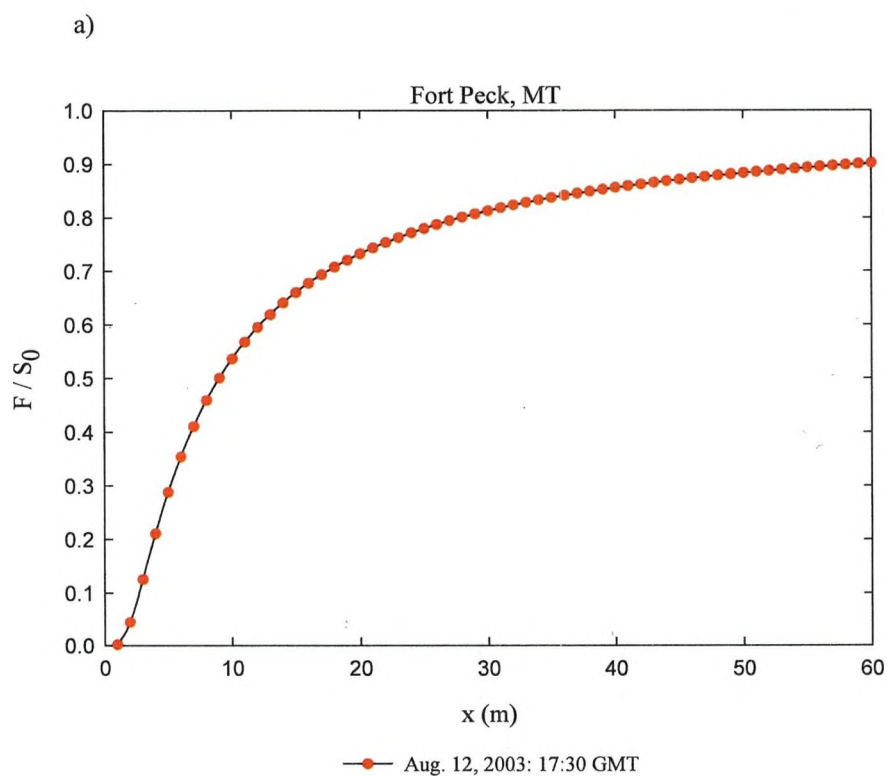
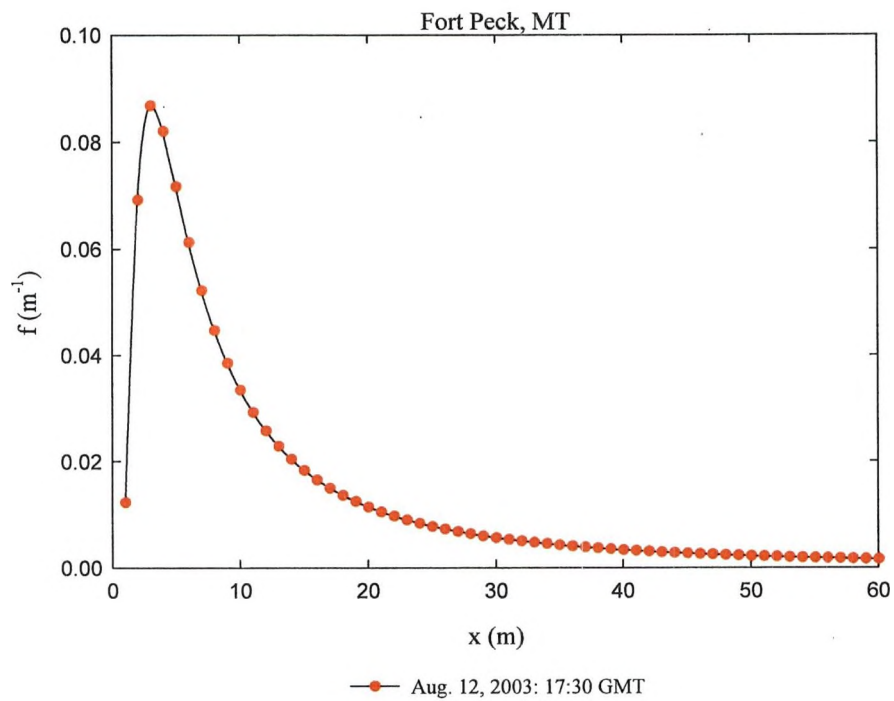
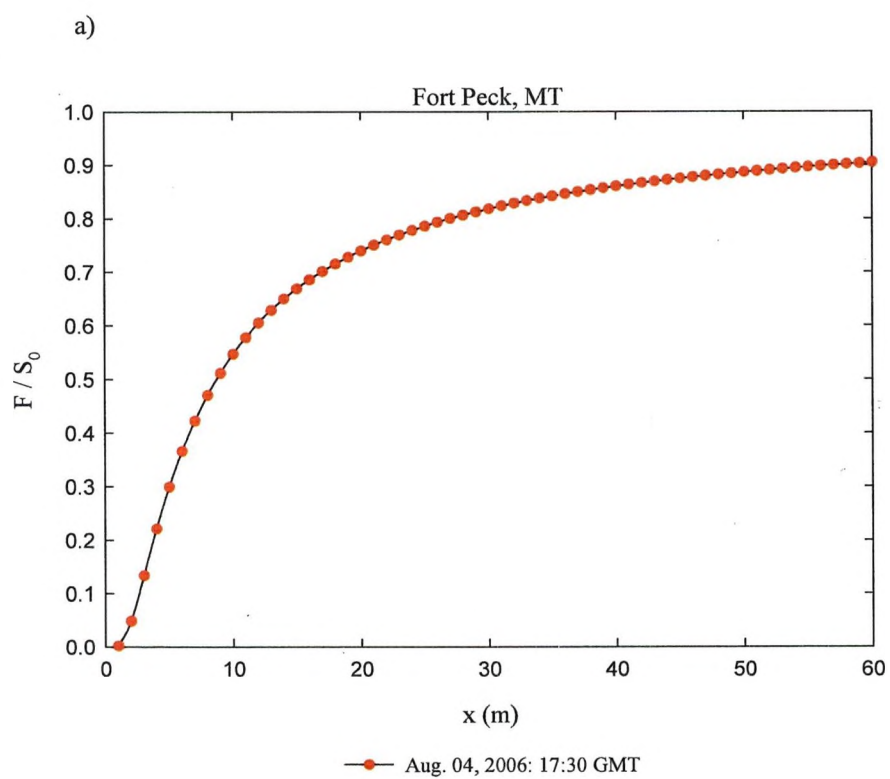
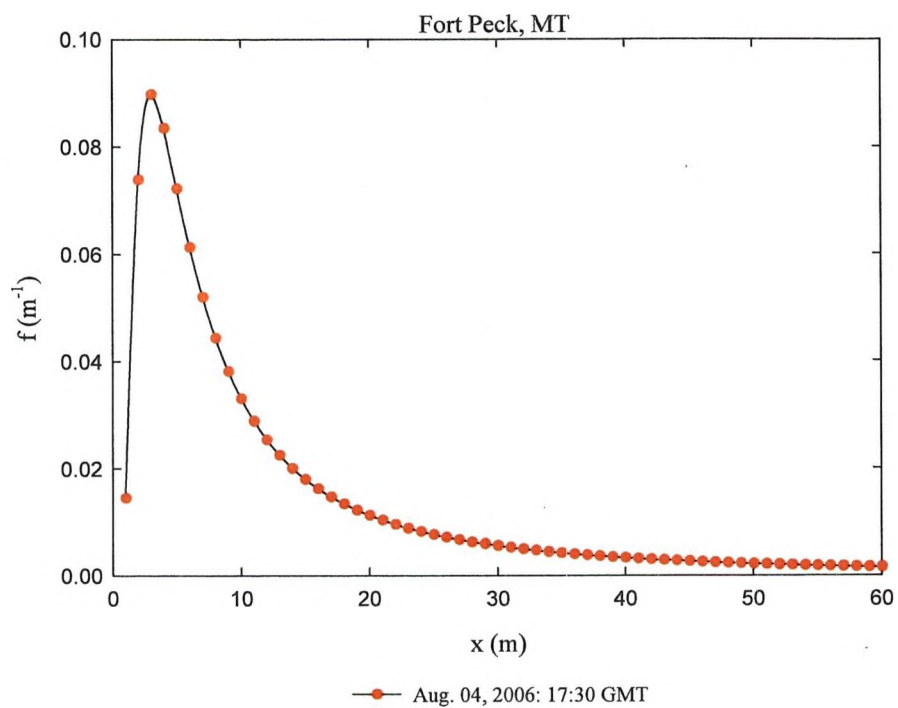
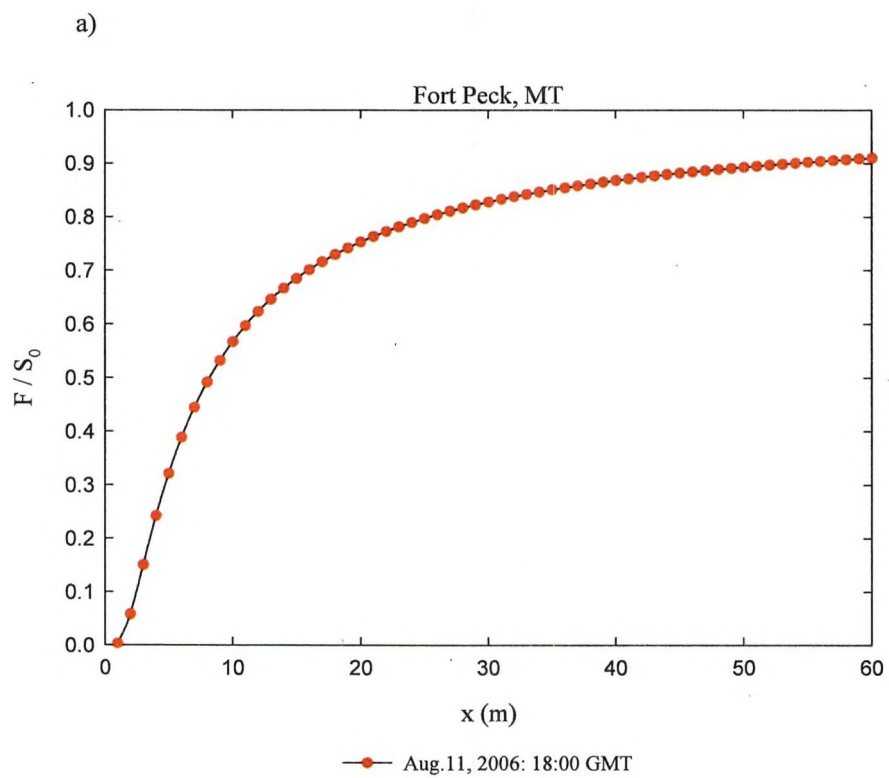
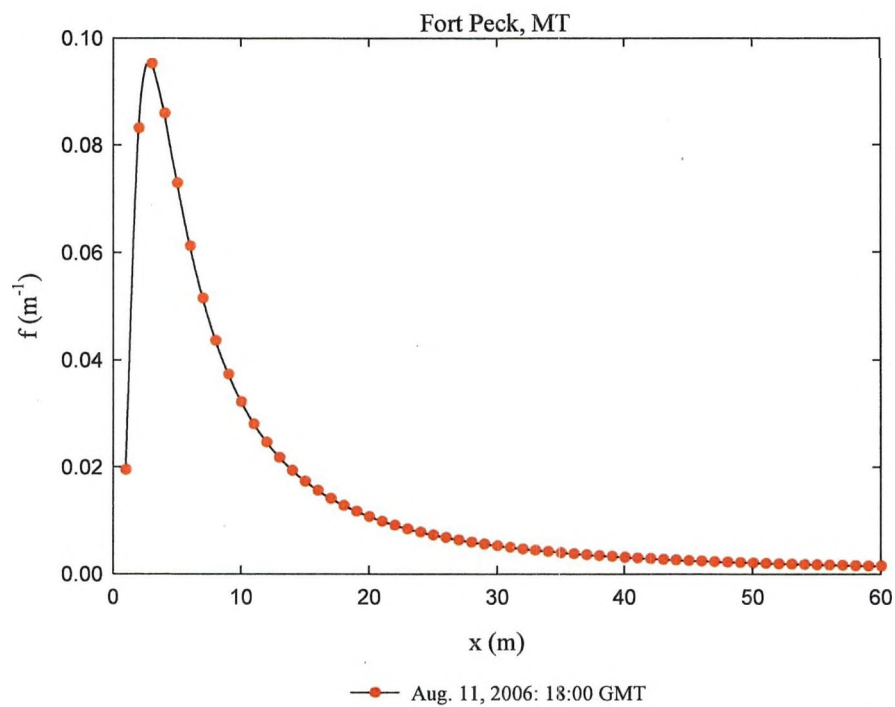


Figure 36 a) footprint and b) cumulative flux as a function of fetch for Landsat TM 081203 overpass date.



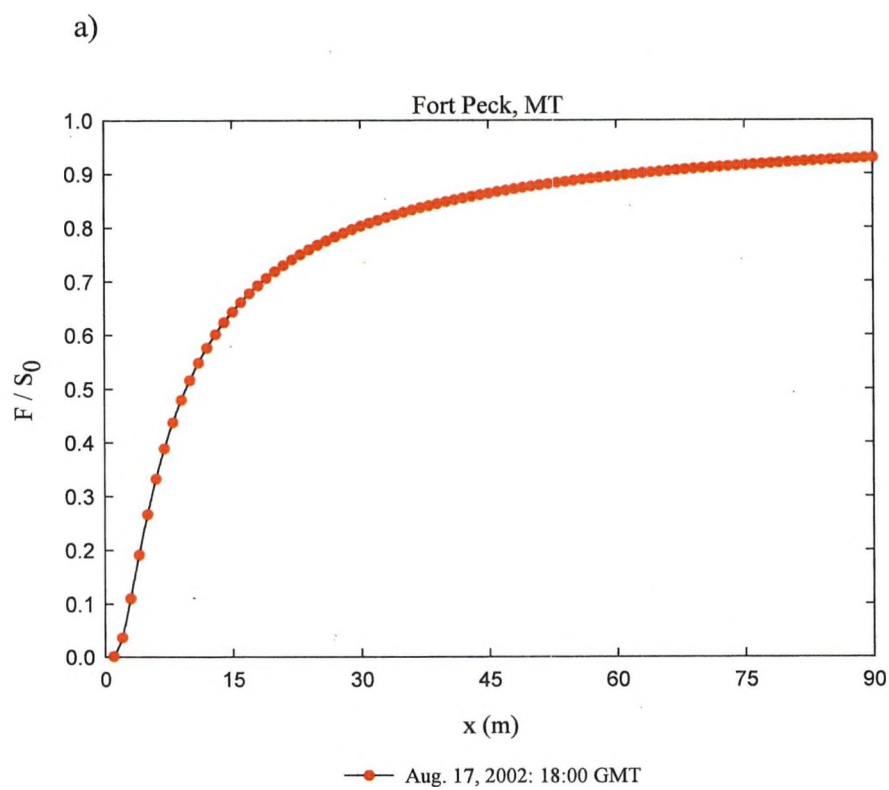
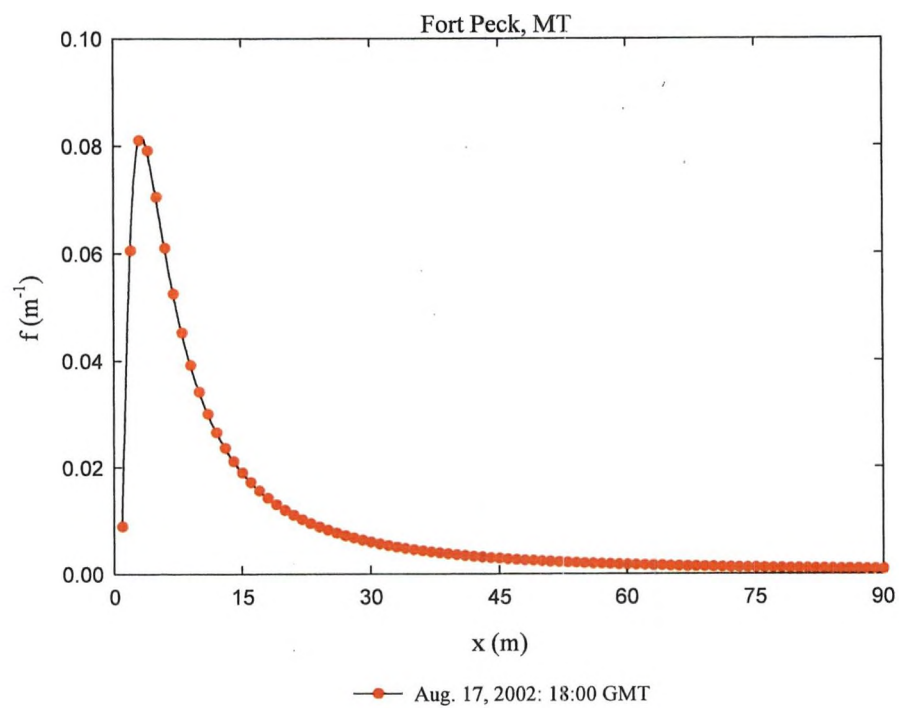
b)

Figure 37 a) footprint and b) cumulative flux as a function of fetch for Landsat TM 080406 overpass date.



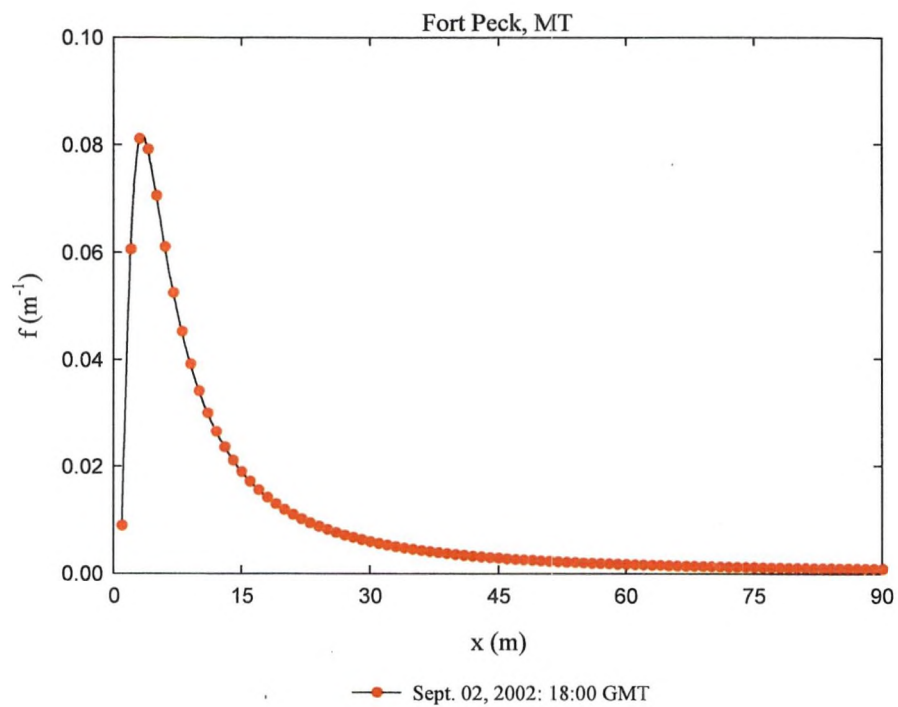
b)

Figure 38 a) footprint and b) cumulative flux as a function of fetch for Landsat TM 081106 overpass date.

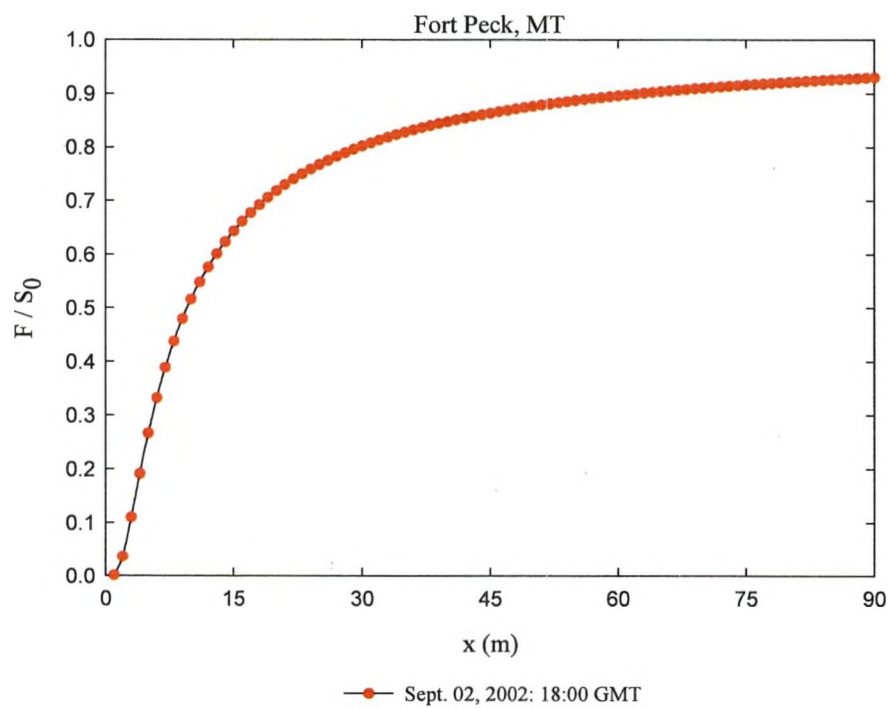


b)

Figure 39 a) footprint and b) cumulative flux as a function of fetch for MODIS 081702 overpass date.

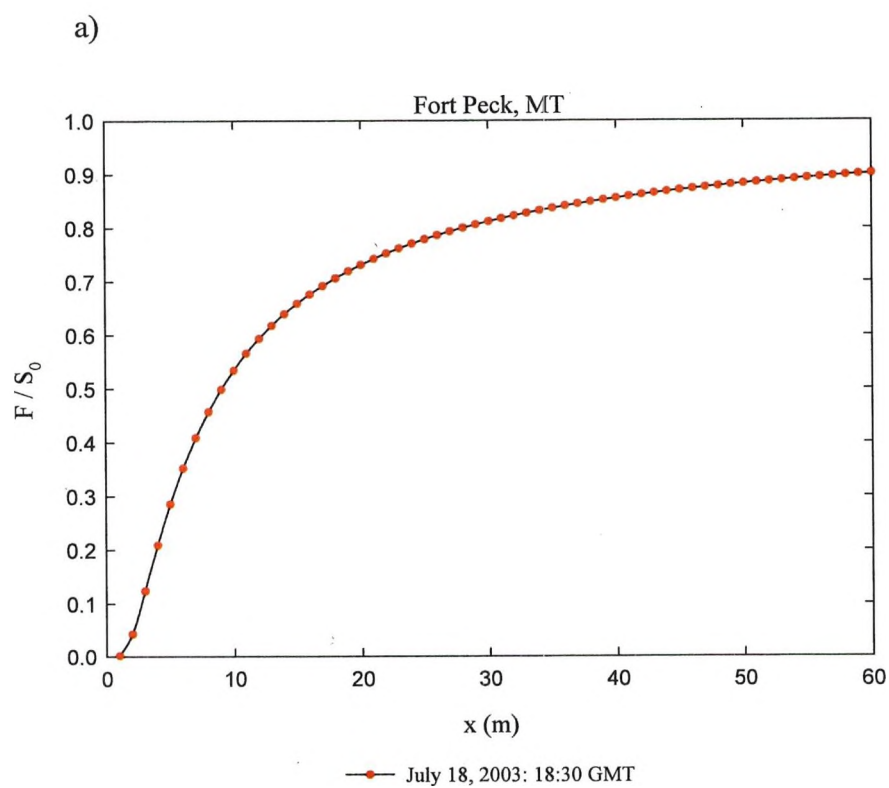
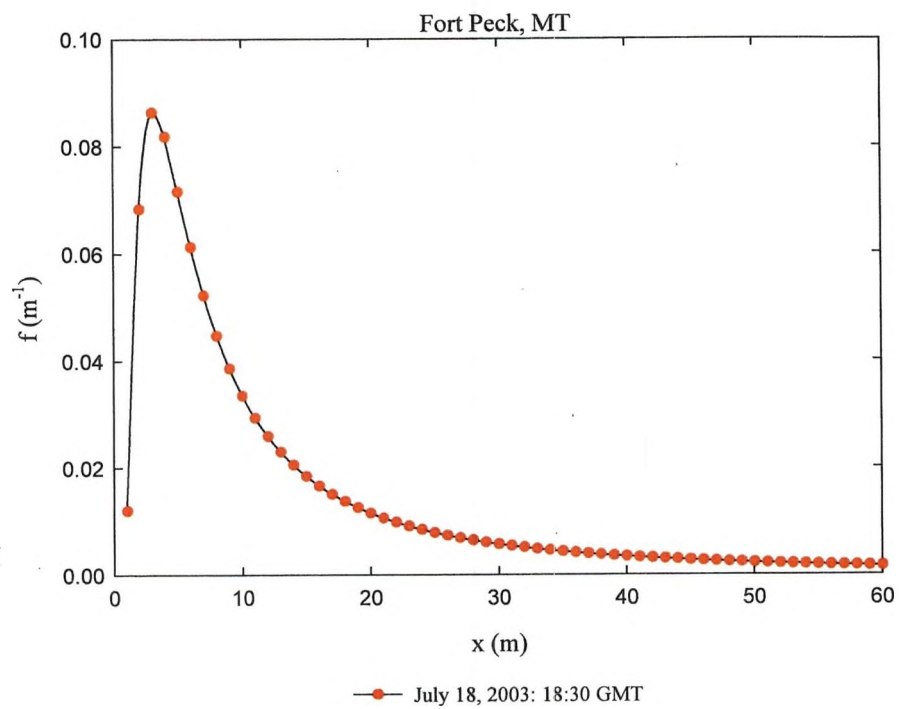


a)



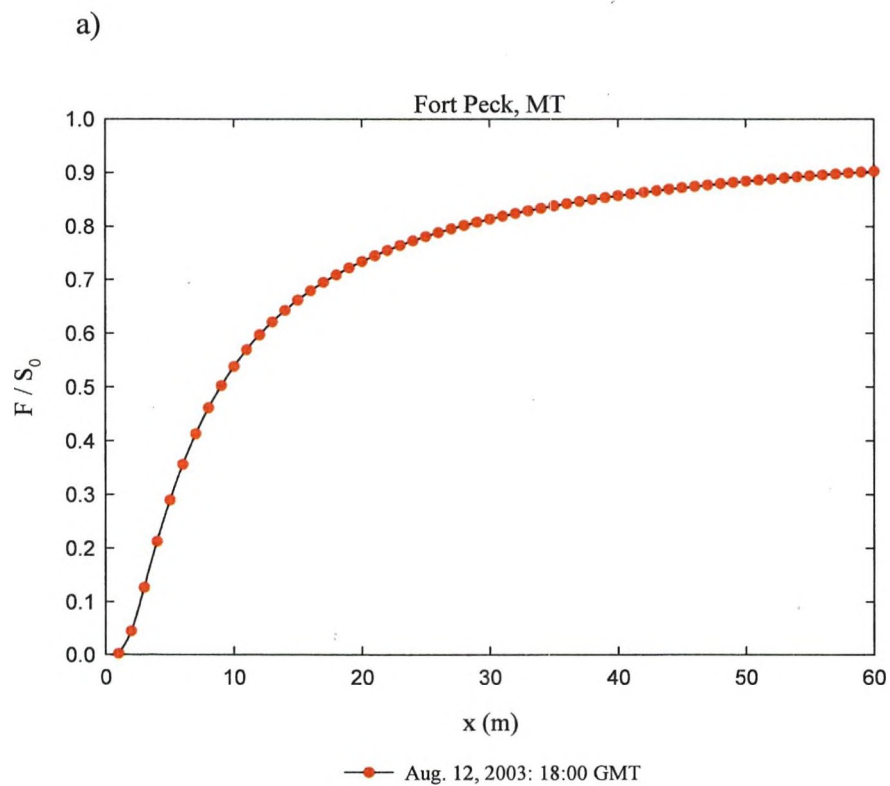
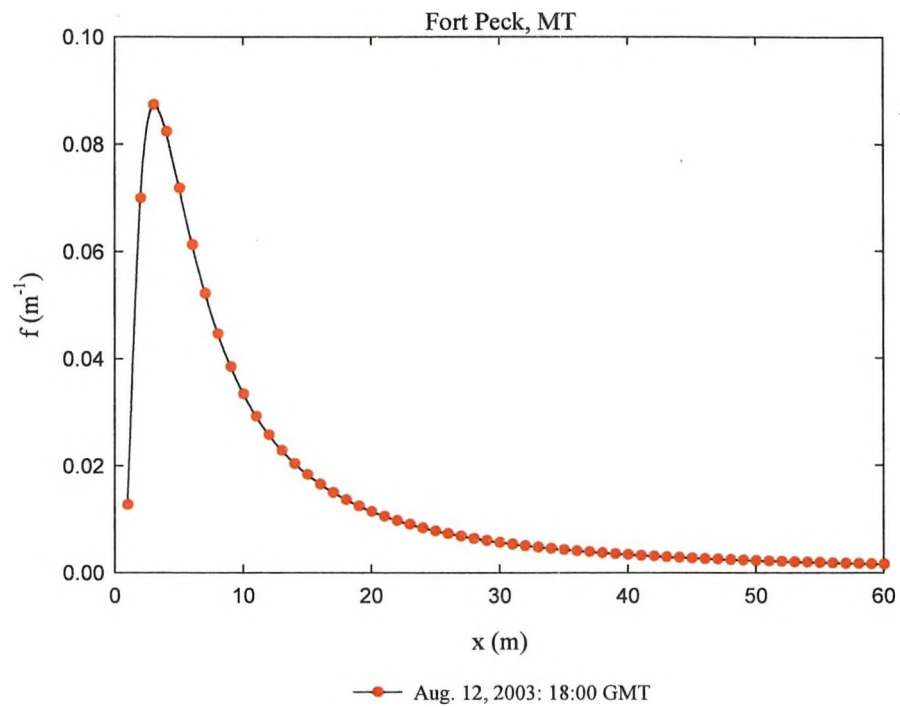
b)

Figure 40 a) footprint and b) cumulative flux as a function of fetch for MODIS 090202 overpass date.



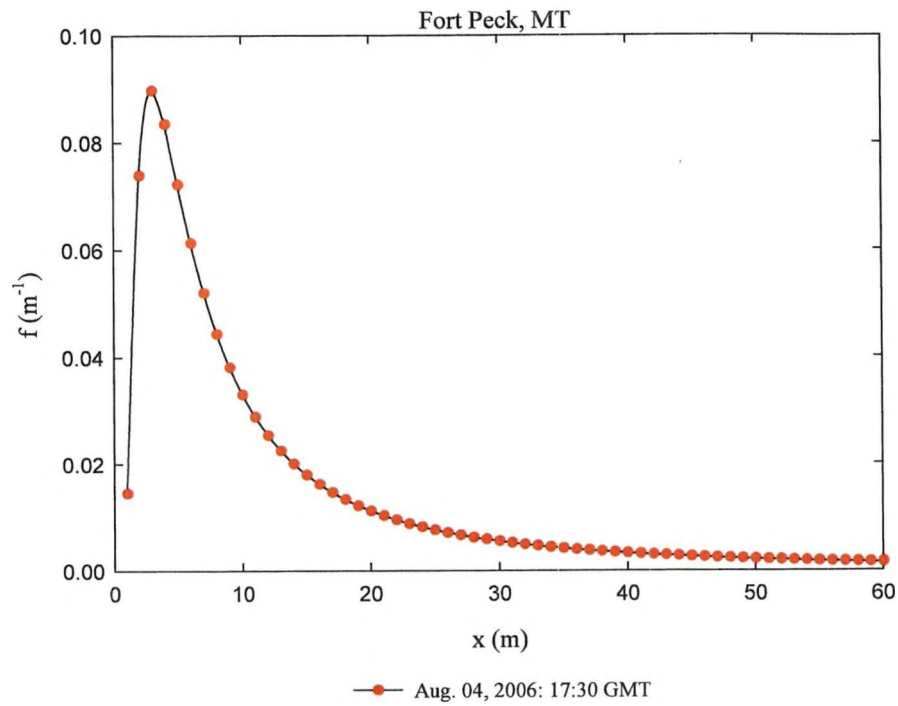
b)

Figure 41 a) footprint and b) cumulative flux as a function of fetch for MODIS 071803 overpass date.

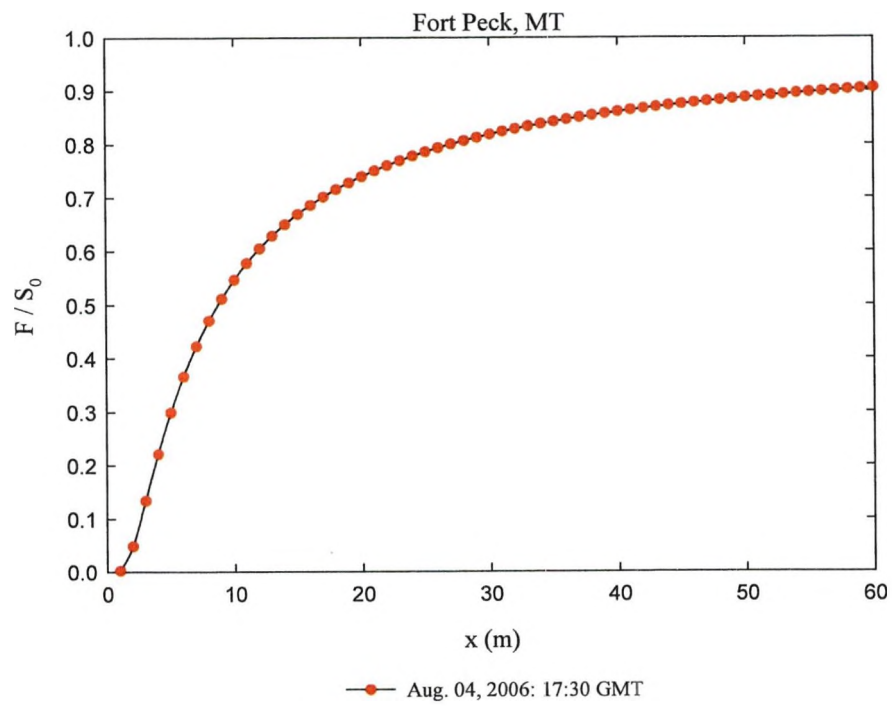


b)

Figure 42 a) footprint and b) cumulative flux as a function of fetch for MODIS 081203 overpass date.

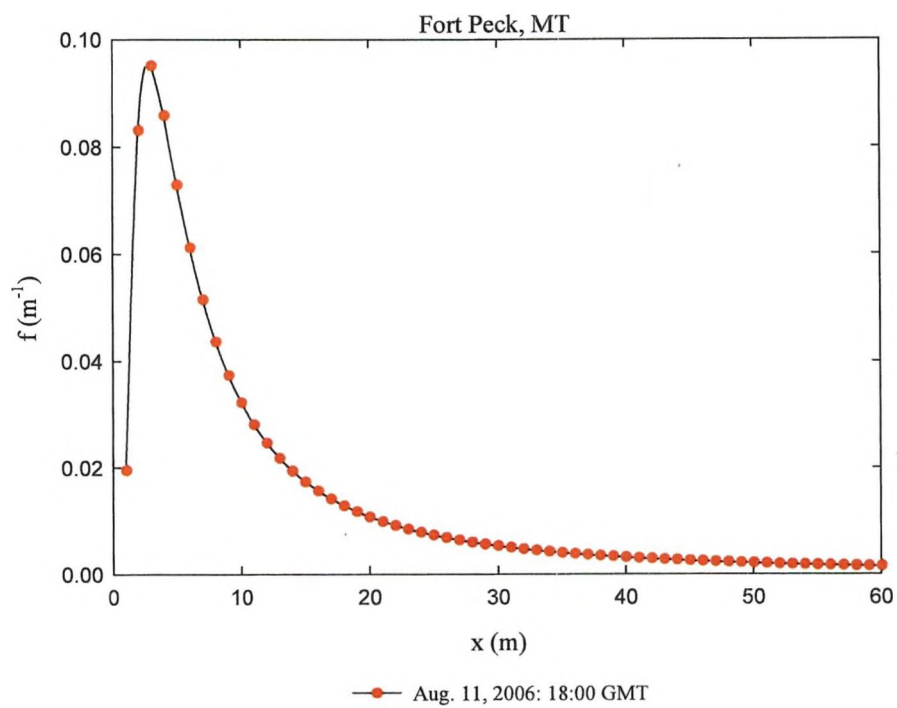


a)

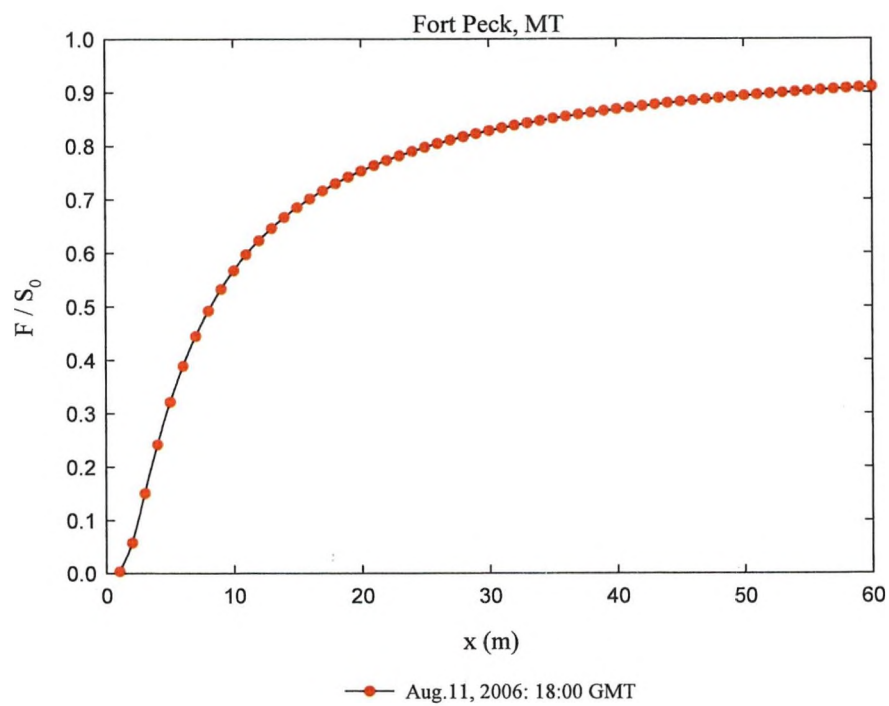


b)

Figure 43 a) footprint and b) cumulative flux as a function of fetch for MODIS 080406 overpass date.



a)



b)

Figure 44 a) footprint and b) cumulative flux as a function of fetch for MODIS 081106 overpass date.

REFERENCES

- Albertson, J., Parlange, M., Kiely, G., and Eichinger, W. 1997. The average dissipation rate of turbulent kinetic energy in the neutral and unstable atmospheric surface layer. *Journal of Geophysical Research*, 102(D12), 13423-13432.
- Allen, R., Morse, A., Tasumi, M. and Kramber, W. 2000. Final report: Application of the SEBAL methodology for estimating consumptive use of water and stream flow depletion in the Bear River Basin of Idaho through remote sensing. Idaho Department of Water Resources and University of Idaho, Department of Biological and Agricultural Engineering: Submitted to The Raytheon System Company: Earth Observation System Data and Information Project.
- Allen, R., Pereira, L., Raes, D. and Smith, M. 1998. "Crop Evapotranspiration." Food and Agricultural Organization of the United Nations, Rome, Italy.
- AmeriFlux Network, Oak Ridge National Laboratory. 2007. Flux tower data. <http://public.ornl.gov/ameriflux/>. Retrieved 12 January 2007. P.O. Box 2008, Oak Ridge, Tennessee 37831-6335, U.S.A.
- Bashir, M., Hata, T., Abdelhad, A., Tanakamaru, H. and Tada, A. 2006. Satellite-based evapotranspiration and crop coefficient for irrigated sorghum in the Gezira scheme, Sudan. *Journal of Hydrology and Earth System Science*, 3, 793-817.
- Bastiaanssen, W. 1995. Regionalization of surface flux densities and moisture indicators in composite terrain: a remote sensing approach under clear skies in Mediterranean climates. Agricultural Research Department, Wageningen, the Netherlands, Report 109.
- Bastiaanssen, W. 2000. SEBAL-based sensible and latent heat fluxes in the irrigated Gediz Basin, Turkey. *Journal of Hydrology*, 229, 87-100.
- Bastiaanssen, W., Menenti, M., Dolman, A., Feddes, R. and Pelgrum, H. 1996. Remote sensing parameterization of meso-scale land surface evaporation. NATO ASI Series, 145: Radiation and water in the climate system: *Remote Measurements*, 401-429.
- Bastiaanssen, W., Menenti, M., Feddes, R. and Holtslag, A. 1998. A remote sensing surface energy balance algorithm for land (SEBAL): 1 formulation. *Journal of Hydrology*, 212-213, 198-212.

- Batra, N., Islam, S., Venturini, V., Bisht, G. and Jiang, L. 2006. Estimation and comparison of evapotranspiration from MODIS and AVHRR sensors for clear sky days over the Southern Great Plains. *Remote Sensing of Environment*, 103, 1-15.
- Bauer, P., Thabeng, G., Stauffer, F., and Kinzelbach, W. 2004. Estimation of the evapotranspiration rate from diurnal groundwater level fluctuations in the Okavango Delta, Botswana. *Journal of Hydrology*, 288 (3-4), 344-355.
- Bisht, G., Venturini, V., Islam, S. and Jiang, L. 2005. Estimation of the net radiation using MODIS (Moderate Resolution Imaging Spectroradiometer) data for clear sky days. *Remote Sensing of Environment*, 97, 52-67.
- Brunsell, N. and Gillies, R. 2003. Scale issues in land-atmosphere interactions: implications for remote sensing of the surface energy balance. *Agricultural and Forest Meteorology*, 117(3-4), 203-221.
- Burba, G., Verma, S., and Kim, J. 1999. Surface energy fluxes of *Phragmites australis* in a prairie wetland. *Agricultural and Forest Meteorology*, 94, 31-51.
- Cain, J., Rosier, P., Meijninger, W., and De Bruin, H. 2001. Spatially averaged sensible heat fluxes measured over barley. *Agricultural and Forest Meteorology*, 107(4), 307-322.
- Chehbouni, A., Watts, C., Lagouarde, J., Kerr, Y., Rodriguez, J., Bonnefond, J., Santiago, F., Dedieu, G., Goodrich, D. and Unkrich, C. 2000. Estimation of heat and momentum fluxes over complex terrain using a large aperture scintillometer. *Agricultural and Forest Meteorology*, 105(1-3), 215-226.
- Chemin, Y. Evapotranspiration of crops by remote sensing using the energy balance based algorithms. Unpublished Manuscript. Asian Institute of Technology, PO Box 4, Klong Luang, Pathumithani 12120, Thailand.
- Cleugh, H., Leuning, R., Mu, Q., and Running, S. 2007. Regional evaporation estimates from flux tower and MODIS satellite data. *Remote Sensing of Environment*, 106(3), 285-304.
- Consoli, S., O'Connell, N. and Snyder, R. 2006. Estimation of evapotranspiration of different-sized navel-orange tree orchards using energy balance. *Journal of Irrigation and Drainage Engineering*, 132(1), 2-8.
- Dingman, S. 2002. *Physical Hydrology*, 2nd ed., 582-607. New Jersey: Prentice-Hall, Inc. Press.
- Driese, K. and Reiners, W. 1997. Aerodynamic roughness parameters for semi-arid natural shrub communities of Wyoming, USA. *Agricultural and Forest Meteorology*, 88, 1-14.

- Finnigan, J. 2006. The storage term in eddy flux calculations. *Agricultural and Forest Meteorology*, 136(3-4), 108-113.
- French, A., Jacob, F., Anderson, M., Kustas, W., Timmermans, W., Gieske, A., Su, Z., Su, H., McCabe, M., Li, F., Prueger, J. and Brunsell, N. 2005. Surface energy fluxes with the Advanced Spaceborne Thermal Emission and Reflection Radiometer (ASTER) at the Iowa 2002 SMACEX site (USA). *Remote Sensing of Environment*, 99, 55-65.
- Gilman, K. 1980. Estimating the soil heat flux in an upland drainage basin. *Hydrological Sciences Bulletin*, 25(4-12), 435-451.
- Granger, R. 2000. Satellite-derived estimates of evapotranspiration in the Gediz basin. *Journal of Hydrology*, 229, 70-76.
- Gutman, G. 1988. A simple method for estimating monthly mean albedo of land surfaces from AVHRR data. *Journal of Applied Meteorology*, 27, 973-988.
- Hafeez, M., Chemin, Y., Van De Giesen, N. and Bouman, B. 2002. Estimation of crop water deficit through remote sensing in Central Luzon, Philippines. IEEE International, Geosciences and Remote Sensing Symposium, 5, 2778-2780.
- Hemakumara, H., Chandrapala, L. and Moene, A. 2003. Evapotranspiration fluxes over mixed vegetation areas measured from large aperture scintillometer. *Agricultural Water Management*, 58, 109-122.
- Hsieh, C., Katul, G. and Chi, T. 2000. An approximate analytical model for footprint estimation of scalar fluxes in thermally stratified atmospheric flows. *Advances in Water Resources*, 23, 765-772.
- Ines, A., Honda, K., Gupta, A., Droogers, P. and Clemente, R. 2006. Combining remote sensing-simulation modeling and genetic algorithm optimization to explore water management options in irrigated agriculture. *Agricultural Water Management*, 83(3), 221-232.
- Jacob, F., Olioso, A., Fa Gu, X., Su, Z. and Seguin, B. 2002. Mapping surface fluxes using airborne visible, near infrared, thermal infrared remote sensing data and a spatialized surface energy balance model. *Agronomie*, 22, 669-680.
- Jasinski, M., Borak, J. and Crago, R. 2005. Bulk surface momentum parameters for satellite-derived vegetation fields. *Agricultural and Forest Meteorology*, 133, 55-68.
- Jia, L., Su, Z., Hurk, B., Menenti, M., Moene, A., De Bruin, H., Yrisarry, J., Ibanez M. and Cuesta, A. 2003. Estimation of sensible heat flux using the Surface Energy Balance System (SEBS) and ASTR measurements. *Physics and Chemistry of the Earth*, 28, 75-88.

- Kaleita, A. and Kumar, P. 2000. AVHRR estimates of surface temperature during the Southern Great Plains 1997 Experiment. *Journal of Geophysical Research*, 105(D16), 20,791-20,801.
- Kampf, S. and Tyler, S. 2006. Spatial characterization of land surface energy fluxes and uncertainty estimation at the Salar de Atacama, Northern Chile. *Advances in Water Resources*, 29(2), 336-354.
- Kim, J., Guo, Q., Baldocchi, D., Leclerc, M., Xu, L. and Schmid, H. 2006. Up-scaling fluxes from tower to landscape: overlaying flux footprints on high-resolution (IKONOS) images of vegetation cover. *Agricultural and Forest Meteorology*, 136, 132-146.
- Kimura, R., Bai, L., Fan, J., Takayama, N. and Hinokidani, O. 2007. Evapotranspiration estimation over the river basin of the Loess Plateau of China based on remote sensing. *Journal of Arid Environments*, 68(1), 53-65.
- Kite, G. and Droogers, P. 2000. Comparing evapotranspiration estimates from satellites, hydrological models and field data. *Journal of Hydrology*, 229(1-2), 3-18.
- Koloskov, G., Mukhamejaov, Kh. and Tanton, T. 2007. Monin-Obukhov length as a cornerstone of the SEBAL calculations of evapotranspiration. *Journal of Hydrology*, 335, 170-179.
- Kongo, V and Jewitt, G. 2006. Preliminary investigation of catchment hydrology in response to agricultural water use innovations: A case study of the Potshini catchment – South Africa. *Physics and Chemistry of the Earth*, 31(15-16), 976-987.
- Kustas, W., Li, F., Jackosn, T., Prueger, J., MacPherson, J. and Wolde, M. 2004. Effects of remote sensing pixel resolution on modeled energy flux variability of cropland in Iowa. *Remote Sensing of Environment*, 92, 535-547.
- Kustas, W., Norman, J., Anderson, M. and French, A. 2003. Estimating sub-pixel surface temperatures and energy fluxes from the vegetation index-radiometric temperature relationship. *Remote Sensing of Environment*, 85, 429-440.
- Lagouarde, J., Jacob, F., Fa Gu, X., Olioso, A., Bonnefond, J., Kerr, Y., McAneney, J. and Irvine, M. 2002. Spatialization of sensible heat flux over a heterogeneous landscape. *Agronomie*, 22, 627-633.
- Lhomme, J., Troufleau, D., Monteny, B., Chehbouni, A. and Bauduin, S. 1997. Sensible heat flux and radiometric surface temperature over sparse Sahelian vegetation II: a model for kB^{-1} parameter. *Journal of Hydrology*, (188-189), 839-854.

- Liang, S., Shuey, C., Russ, A., Fang, H., Chen, M., Walthall, C., Daughtry, C. and Hunt, R. 2002. Narrowband to broadband conversions of land surface albedo: II: validation. *Remote Sensing of Environment*, 84, 25-41.
- Mauser, W. and Schädlich, S. 1998. Modeling the spatial distribution of evapotranspiration on different scales using remote sensing data. *Journal of Hydrology*, 212-213, 250-267.
- McCabe, M., Kalma, J. and Franks, S. 2005. Spatial and temporal patterns of land surface fluxes from remotely sensed surface temperatures within an uncertainty modeling framework. *Hydrology and Earth Systems Sciences Discussion*, 2, 569-603.
- McCabe, M. and Wood, E. 2006. Scale influences on the remote estimation of evapotranspiration using multiple satellite sensors. *Remote Sensing of Environment*, 105(4), 271-285.
- Melesse, A. 2004. Spatiotemporal dynamics of land surface parameters in the Red River of the North Basin. *Physics and Chemistry of the Earth, Parts A/B/C*, 29(11-12), 795-810.
- Melesse, A. and Nangia, V. 2005. Estimation of spatially distributed surface energy fluxes using remotely-sensed data for agricultural fields. *Hydrological Processes*, 19, 2653-2670.
- Mohamed, Y., Bastiaanssen, W. and Savenije, H. 2004. Spatial variability of evaporation and moisture storage in the swamps of the upper Nile studied by remote sensing techniques. *Journal of Hydrology*, 289, 145-164.
- NASA. 2006. Landsat handbooks.
http://ltpwww.gsfc.nasa.gov/IAS/handbook/handbook_htmls/chapter11/chapter11.html#section11.3.3. NASA Headquarters, Suite 5K39, Washington, DC 20546-0001.
- Nagler, P., Cleverly, J., Glenn, E., Lampkin, D., Huete, A. and Wan, Z. 2005. Predicting riparian evapotranspiration from MODIS vegetation indices and meteorological data. *Remote Sensing of Environment*, 94, 17-30.
- Nagler, P., Scott, R., Westenburg, C., Cleverly, J., Glenn, E. and Huete, A. 2005. Evapotranspiration on western U.S. rivers estimated using the Enhanced Vegetation Index from MODIS and data from eddy covariance and Bowen ratio flux towers. *Remote Sensing of Environment*, 97, 337-351.
- Nagar, S., Seetaramayya, P., Tyagi, A. and Singh, S. 2002. Estimation of daytime surface fluxes of radiation and heat at Anand during 13-17 May 1997. *Current Science*, 83(1), 39-46.

- Oberg, J. and Melesse, A. 2006. Evapotranspiration dynamics at an ecohydrological restoration site: an energy balance and remote sensing approach. *Journal of the American Water Resources Association*, 565-582.
- Olioso, A., Chauki, H., Courault, D. and Wigneron, J. 1999. Estimation of evapotranspiration and photosynthesis by assimilation of remote sensing data into SVAT Models. *Remote Sensing of Environment*, 68(3), 341-356.
- Overgaard, J., Rosbjerg, D. and Butts, M. 2006. Land-surface modeling in hydrological perspective – a review. *Biogeosciences*, 3, 229-241.
- Pereira, A., Green, S., Augusto, N. and Nova, V. 2006. Penman-Monteith reference evapotranspiration adapted to estimate irrigated tree transpiration. *Agricultural Water Management*, 83(1-2), 153-161.
- Rivas, R. and Caselles, V. 2004. A simplified equation to estimate spatial reference evaporation from remote sensing-based surface temperature and local meteorological data. *Remote Sensing of Environment*, 93, 68-76.
- Schmugge, T., Kustas, W. and Humes, K. 1998. Monitoring land surface fluxes using ASTER observations. *IEEE Transactions on Geosciences and Remote Sensing*, 36(5), 1421-1430.
- Skeiker, K. 2006. Correlation of global solar radiation with common geographical and meteorological parameters for Damascus, Syria. *Energy Conservation and Management*, 47, 331-345.
- Steven, M., Malthus, T., Baret, F., Xu, H. and Chopping, M. 2003. Inter-calibration of vegetation indices from different sensor systems. *Remote Sensing of Environment*, 88, 412-422.
- Tang, B., Li, Z. and Zhang, R. 2006. A direct method for estimating net surface shortwave radiation from MODIS data. *Remote Sensing of Environment*, 103, 115-126.
- Timmermans, W., Kustas, W., Anderson, M. and French, A. 2007. An inter-comparison of the Surface Energy Balance Algorithm for Land (SEBAL) and the Two-Source Energy Balance (TSEB) modeling schemes. *Remote Sensing of Environment*, 108, 369-384.
- Timmermans, W. and Meijerink, A. 1999. Remotely sensed actual evapotranspiration: implications for groundwater management in Botswana. *Journal of Applied Geohydrology*, 1(3/4), 222-2333.

- USGS, NASA Distributed Active Archive Center. 2002-2006. MODIS data. <http://edcdaac.usgs.gov/main.asp>. Retrieved December 5, 2006, from Earth Observing System -Land Processes Distributed Active Archive Center, EOS-LP DAAC: Center for Earth Resources Observation and Science (EROS), 47914 252nd Street, Sioux Falls, SD, 57198-0001.
- USGS, U.S. Department of the Interior, National Land Cover map. 2001. Land cover map. <http://www.mrlc.gov/>. Retrieved January 10, 2007, from MRLC Consortium- U.S. Geological Survey (USGS): Center for Earth Resources Observation and Science (EROS), MRLC Project 47914 252nd Street, Sioux Falls, SD, 57198-0001
- Venturini, V., Bisht, G., Islam, S. and Jiang, L. 2004. Comparison of evaporative fractions estimated from AVHRR and MODIS sensors over South Florida. *Remote Sensing of Environment*, 93, 77-86.
- Verstraeten, W., Veroustraete, F. and Feyen, J. 2005. Estimating evapotranspiration of European forests from NOAA-imagery at satellite overpass time: towards an operational processing chain for integrated optical and thermal sensor data products. *Remote Sensing of Environment*, 96, 256-276.
- Waheed, T., Bonnell, R., Prasher, S and Paulet, E. 2006. Measuring performance in precision agriculture: CART—a decision tree approach. *Agricultural Water Management*, 84(1-2), 173-185.
- Wang, K., Li, Z. and Cribb, M. 2006. Estimation of evaporative fraction from a combination of day and night land surface temperatures and NDVI: a new method to determine the Priestley-Taylor parameter. *Remote Sensing of Environment*, 102, 293-305.
- Wang, J., Miller, D., Sammis, T., Gutschick, V., Simmons, L. and Andales, A. 2007. Energy balance measurements and a simple model for estimating pecan water use efficiency. *Agricultural Water Management*, 19(1-3), 92-101.
- Wever, L., Flanagan, L. and Carlson, P. 2002. Seasonal and inter-annual variation in evapotranspiration, energy balance and surface conductance in a northern temperate grassland. *Agricultural and Forest Meteorology*, 112, 31-49.
- Wu, W., Hall, C., Scatena, F. and Quackenbush, L. 2006. Spatial modeling of evapotranspiration in the Liquillo experimental forest of Puerto Rico using remotely-sensed data. *Journal of Hydrology*, 328, 733-752.
- Yang, C., Chandler, R., Isham, V., Annoni, C. and Wheeler, H. 2005. Simulation and downscaling models for potential evaporation. *Journal of Hydrology*, 302(1-4), 239-254.

- Zhan, X., Kustas, W. and Humes, K. 1996. An inter-comparison study on models of sensible heat flux over partial canopy surfaces with remotely sensed surface temperature. *Remote Sensing of Environment*, 58(3), 242-256.
- Zwart, S. and Bastiaanssen, W. 2007. SEBAL for detecting spatial variation of water productivity and scope for improvement in eight irrigated wheat systems. *Agricultural Water Management*, 89(3), 287-296.